# Optically detected cyclotron resonance in a single GaAs/AlGaAs heterojunction

Dissertation

presented to the Faculty of Physics of the
Technische Universität Dortmund, Germany,
in partial fulfillment of the requirements
for the degree of

Doktor rer. nat.


presented by

Gregor Bartsch

Dortmund, August 2011

Accepted by the Faculty of Physics of the
Technische Universität Dortmund, Germany.

Day of the oral exam: 23rd September 2011

Examination board:

Prof. Dr. Dmitri Yakovlev
Prof. Dr. Manfred Bayer
Prof. Dr. Götz Uhrig
Dr. Ilya Akimov

# Contents

# 1 Introduction

Modern semiconductor industry relies on the concept of heterostructures. Semiconductor heterostructures are artificial crystals that contain layers of different materials. Prominent examples are the *p*-*n* junction of a diode, the quantum well in a semiconductor laser or the single heterojunction (HJ) in a high-electron-mobility transistor (HEMT).

The single HJ, used in a HEMT, stands out due to its high electron mobility. The electrons are located in a potential notch in the vicinity of the HJ. Along the interface plane they can move freely, while the motion perpendicular to the interface is confined. The system of electrons is therefore called a *two-dimensional-electron gas* (2DEG). High electron mobility is achieved by choosing a material system, which provides good interface quality and a low amount of impurities. Today, heterojunctions of GaAs and AlGaAs are widely used for that purpose. Furthermore, the doping technique is crucial for a high mobility 2DEG: *Modulation doping* spatially separates dopants and carriers and therefore avoids additional electron scattering at ionized donors.

High electron mobilities are of crucial importance for the technical application of HEMTs. High operation frequencies and a low noise level are only possible due to high mobility 2DEGs. In fact, high carrier mobilities have a positive effect on the efficiency of modern semiconductor devices, whenever carrier dynamics plays an essential role in the functional principle. For example, this is the case for the electron-hole separation process in a solar cell or for the carrier transport to the *p*-*n* junction in a light emitting diode.

Similarly, basic research benefits from high electron mobilities: Low carrier scattering means direct access to intrinsic electronic properties. Consequently, high mobility 2DEGs in GaAs/AlGaAs HJs represent an interesting system to investigate the electronic band structure.

In this work, a GaAs/AlGaAs HJ is studied by optically detected far-infrared cyclotron resonance (FIR-ODCR). FIR-ODCR is a powerful tool to investigate electronic properties in semiconductors - it combines the FIR-

excitation of electron-intraband transitions with optical detection by photoluminescence (PL) [1, 2, 3]. The technique allows a detailed and especially sensitive access to electron-cyclotron resonance (CR) by analyzing the change of rich PL spectra under FIR irradiation. In order to discuss the PL modulation under FIR influence, a deep understanding of the plain PL itself is required.

The PL of GaAs/AlGaAs HJs attracted much attention in the past. A highly important contribution was the spectroscopic evidence for the integer and the fractional quantum hall effect in 1990 [4, 5]. Abrupt changes in the PL were used as an indicator for fractionally or totally filled Landau levels. While there is no doubt about the definitive observation of the quantum Hall effect, different explanations of the mechanism behind the PL discontinuities can be found in literature. The latest explanation was introduced in the year 2000 [6] and confirmed in later studies [7]. It describes a coexistence of 2DEG to three-dimensional (3D) hole transitions and free 3D-exciton recombinations. The abrupt PL intensity redistributions are attributed to an exciton-dissociation mechanism at the GaAs/AlGaAs interface. The model differs considerably from previously presented PL interpretations.

In parallel to the extended work on pure PL, a few FIR-ODCR studies on GaAs/AlGaAs HJs were published [8, 9, 10, 11]. However, all of them were written before the year 2000 and none of them considers the mechanism of exciton dissociation. Therefore, the current state of FIR-ODCR studies on GaAs/AlGaAs HJ's is not satisfying and it is necessary to resume experiments, considering the latest insights into the HJs photoluminescence.

This work aims to provide a reinterpretation of FIR-ODCR in GaAs/-AlGaAs HJs in the frame of the exciton-dissociation mechanism. Furthermore the systematic use of low power-laser excitation allows insight into intrinsic system parameters, like conduction-band nonparabolicity or electron mobility, which has not been demonstrated by FIR-ODCR before.

This thesis is structured as follows: Chapter 2 gives a basic theoretical overview of electron-cyclotron resonance, followed by chapter 3, where basic properties of interband transitions are discussed, in order to provide a model of optical recombinations in GaAs. After that, a compact revision of the experimental technique and the typical treatment of ODCR data is presented in chapter 4. Chapter 5 introduces the sample and highlights the specific methods to supply high electron mobilities. An extended review of the PL of GaAs/AlGaAs HJs is presented in chapter 6. This includes the discussion of the interesting history of PL interpretation and the application of the exciton dissociation model on the polarization-resolved magneto-PL experiments. In chapter 7 the FIR influence on the PL is investigated. It is possible to explain the ODR mechanism by an exciton drag. It is mediated by ballistically

propagating phonons, which are emitted by the resonantly heated 2DEG. Very narrow ODCRs are presented, and by using a Drude model for FIR absorption, realistic mobility values can be calculated. The exceptionally narrow ODCRs allow to measure conduction-band nonparabolicity effects and resolve satellite resonances, close to the main CR line. Conclusions are drawn in chapter 8.

# 2

# Cyclotron resonance - basic principles

This chapter is dedicated to CR-transitions in the FIR spectral range. In the following a quantum mechanical picture of crystal electrons in magnetic fields is presented and selection rules for CR-transitions are developed (Sec. 2.1). After that a classical Drude model for CR is discussed (Sec. 2.2).

## 2.1 Quantum mechanics

### 2.1.1 The effective mass approximation

A suitable starting point to describe the electron-cyclotron resonance in semiconductors is to introduce the solid surrounding the electrons. The influence of a crystal potential can be described by the effective mass approximation. For the basic understanding it is sufficient to consider a single electron in an isotropic crystal first. In an anisotropic crystal the effective mass is a tensor of third order, see e.g. [12] or [13].

The periodic potential is given as $U(\boldsymbol{r}) = U(\boldsymbol{r} + \boldsymbol{R})$, where $\boldsymbol{r}$ is the electrons spacial coordinate and $\boldsymbol{R}$ is a lattice point position vector. The Hamiltonian of the single electron in the potential $U(\boldsymbol{r})$ with the mass $m_0$ and the momentum $p$ reads

$$H = \frac{p^2}{2m_0} + U(\boldsymbol{r}). \tag{2.1}$$

The corresponding Schrödinger equation is solved by Bloch-functions [14]

$$\psi_{n\boldsymbol{k}}(\boldsymbol{r}) = e^{i\boldsymbol{k}\boldsymbol{r}} u_{n\boldsymbol{k}}(\boldsymbol{r}). \tag{2.2}$$

They factorize into two parts, one showing characteristics of free electrons $e^{i\boldsymbol{k}\boldsymbol{r}}$ and the other showing lattice periodic contributions of each atomic nucleus

$u_{n\boldsymbol{k}}(\boldsymbol{r})$, where $n$ is the band index.
Operating $H$ on $\psi_{n\boldsymbol{k}}(\boldsymbol{r})$, one obtains a differential equation for $u_{n\boldsymbol{k}}(\boldsymbol{r})$

$$\left(\frac{p^2}{2m_0} + \frac{\hbar\,\boldsymbol{k}\,\boldsymbol{p}}{m_0} + \frac{\hbar^2\,\boldsymbol{k}^2}{2m_0} + U(\boldsymbol{r})\right) u_{n\boldsymbol{k}}(\boldsymbol{r}) = E_{n\boldsymbol{k}}\, u_{n\boldsymbol{k}}(\boldsymbol{r}), \tag{2.3}$$

with the eigenvalues $E_{n\boldsymbol{k}}$ and the reduced Planck constant $\hbar$. For small $\boldsymbol{k}$, that means close to the band edge, $\frac{\hbar\,\boldsymbol{k}\,\boldsymbol{p}}{m_0}$ can be treated as a perturbation. This method is commonly called $\boldsymbol{k}\,\boldsymbol{p}$ *perturbation theory*. In the second order of nondegenerate perturbation theory, the eigenvalues of equation 2.3 are

$$E_{n\boldsymbol{k}} = E_{n\boldsymbol{0}} + \frac{\hbar^2\,\boldsymbol{k}^2}{2m_0} + \frac{\hbar^2}{m_0^2}\sum_{n'\neq n}\frac{\left|\langle u_{n\boldsymbol{0}}|\boldsymbol{k}\,\boldsymbol{p}|u_{n'\boldsymbol{0}}\rangle\right|^2}{E_{n\boldsymbol{0}} - E_{n'\boldsymbol{0}}}. \tag{2.4}$$

The first order $\boldsymbol{k}\,\boldsymbol{p}$ perturbation term vanishes

$$\left|\langle u_{n\boldsymbol{0}}|\boldsymbol{k}\,\boldsymbol{p}|u_{n\boldsymbol{0}}\rangle\right| = 0, \tag{2.5}$$

as the wavefunction $u_{n\boldsymbol{0}}$ has the same inversion symmetry, as the lattice $U(\boldsymbol{r}) = U(-\boldsymbol{r})$.

A central expression, for treating carrier masses in solid states, comes along with the following notation of equation 2.4:

$$E_{n\boldsymbol{k}} = E_{n\boldsymbol{0}} + \frac{\hbar^2\,\boldsymbol{k}^2}{2m^*}, \tag{2.6}$$

where

$$\frac{1}{m^*} = \frac{1}{\hbar^2}\frac{\partial^2}{\partial\boldsymbol{k}^2}\,E_{n\boldsymbol{k}}(\boldsymbol{k}) = \frac{1}{m_0} + \frac{2}{m_0^2\boldsymbol{k}^2}\sum_{n'\neq n}\frac{\left|\langle u_{n\boldsymbol{0}}|\boldsymbol{k}\,\boldsymbol{p}|u_{n'\boldsymbol{0}}\rangle\right|^2}{E_{n\boldsymbol{0}} - E_{n'\boldsymbol{0}}}. \tag{2.7}$$

Equations 2.6 and 2.7 demonstrate that for sufficiently small $\boldsymbol{k}$, crystal electrons act like free electrons, having an effective mass $m^*$. The quadratic dispersion differs only in the electron mass from the vacuum-electron dispersion. In other words, the crystal potential is condensed in the effective mass only and the band electrons can be approximated as freely moving particles with a modified but to a large extend constant effective mass.

$$H = \frac{p^2}{2m_0} + U(\boldsymbol{r}) \rightarrow H^* = \frac{p^2}{2m^*} \tag{2.8}$$

The effective mass is commonly expressed in units of the vacuum mass $m_0$. Dramatic differences from $m_0$ are very usual, e.g. in GaAs the effective electron mass is $m^* = 0.067\,m_0$. At the edges of the Brillouin zone, where

the band is not parabolic any more, even negative values for the effective mass are possible.

Beyond the description of single electrons the effective mass approximation is widely applicable in solid state physics (see e.g. [15]). Coulomb interactions, like in excitons, external magnetic fields or confinement potentials are commonly expressed in the frame of the effective mass approximation: the real Schrödinger equation of the full problem, including the crystal potential, is replaced by the so called *effective Schrödinger equation*, which does not contain the crystal potential and the vacuum carrier masses are substituted by the effective masses. The effective Schrödinger equation coincides with the corresponding problem in the free space. Its eigenfuctions are envelope functions which do not contain lattice periodic contributions.

### 2.1.2 External magnetic fields

The perturbation of an external magnetic field is introduced by starting from the crystal-electrons Hamiltonian in effective mass approximation and performing the standard substitution $\boldsymbol{p} \rightarrow \boldsymbol{p} - e\boldsymbol{A}$, see e.g. [16]:

$$H = \frac{(\boldsymbol{p} - e\boldsymbol{A})^2}{2m^*}. \tag{2.9}$$

Here $\boldsymbol{A}$ is the vector potential obeying $\boldsymbol{B} = \mathrm{rot}\boldsymbol{A}$. In case of a homogeneous magnetic field $\boldsymbol{B}$ along the $z$-direction, it is convenient to write

$$H = H_{xy} + H_z, \tag{2.10}$$

as $H_z$ is not influenced by the magnetic field. Without loss of generality the $z$-direction will be omitted in the following and the two-dimensional problem of $H_{xy}$ will be treated independently.

Several different approaches to solve $H_{xy}\Psi = E\Psi$ can be found in quantum mechanics textbooks. Naturally all of them lead to the same Landau level eigenvalues, but one of them provides especially direct insight into the intraband selection rules. At first the so called kinetic momentum $\boldsymbol{\pi}$ is introduced:

$$\boldsymbol{\pi} = \boldsymbol{p} - e\boldsymbol{A}. \tag{2.11}$$

Hence the Hamiltonian reads

$$H_{xy} = \frac{\boldsymbol{\pi}^2}{2m^*} = \frac{\pi_x^2 + \pi_y^2}{2m^*}. \tag{2.12}$$

Independent of the chosen gauge, $\boldsymbol{\pi}$ obeys several commutation relations

$$[x, \pi_x] = [y, \pi_y] = i\hbar \tag{2.13}$$
$$[x, \pi_y] = [y, \pi_x] = 0 \tag{2.14}$$
$$[x, y] = 0 \tag{2.15}$$
$$[\pi_x, \pi_y] = -i\hbar^2/l^2. \tag{2.16}$$

The magnetic length

$$l = \sqrt{\hbar/m^*\omega_c} = \sqrt{\hbar/eB} \tag{2.17}$$

defines the radius of the cyclotron orbit (see Eq. 2.30) and

$$\omega_c = eB/m^* \tag{2.18}$$

is the cyclotron frequency.

Defining raising and lowering operators

$$a_\pm = \frac{l}{\sqrt{2}\hbar}\left(\pi_x \pm i\pi_y\right), \tag{2.19}$$

allows to write the Hamiltonian in the form of a harmonic oscillator

$$H_{xy} = \hbar\omega_c\left(a_+a_- + \frac{1}{2}\right). \tag{2.20}$$

Using the commutiation relations 2.16 one finds

$$[a_-, a_+] = 1 \tag{2.21}$$
$$[H_{xy}, a_\pm] = \pm\,\hbar\omega_c a_\pm. \tag{2.22}$$

In analogy to the harmonic oscillator a number operator $N$ and the respective eigenfunctions $|N\rangle$ are introduced

$$N = a_+a_-, \tag{2.23}$$
$$N\,|N\rangle = N\,|N\rangle\,. \tag{2.24}$$

The functions $|N\rangle$ are also eigenfunctions of $H_{xy}$

$$H_{xy}\,|N\rangle = E_{_N}\,|N\rangle = \hbar\omega_c\left(N + \frac{1}{2}\right)|N\rangle\,. \tag{2.25}$$

The eigenvalues

$$E_{_N} = \hbar\omega_c\left(N + \frac{1}{2}\right) \tag{2.26}$$

are known as *Landau levels* [17]. For a finite magnetic field, $\hbar\omega_c \neq 0$, the motion in the $xy$-plane is quantized and the energy eigenvalues $E_N$ are equally distanced by the cyclotron energy $\hbar\omega_c$, while $\omega_c$ itself increases linearly with $B$. In Fig. 2.1 (a) $E_N(B)$ are shown for several values of $N$.

Landau levels are highly degenerate with respect to the center coordinate of the cyclotron orbit [18]. Considering the electron spin, a semiconductor of the dimensions $L_x$ and $L_y$ each Landau level is $\eta$-times degenerate:

$$\eta = \frac{eBL_xL_y}{h}. \tag{2.27}$$

For an electron density $n_e$ a filling factor $\nu$ can be introduced as the ratio of the total number of electrons and the Landau level degeneracy $\eta$

$$\nu = \frac{n_eL_xL_y}{\eta} = \frac{n_e}{eB/h}. \tag{2.28}$$

Here, $\nu$ reflects the number of completely filled Landau levels. If $\nu = \beta$, with $\beta$ being an integer, exactly $\beta$ Landau levels are completely occupied.

The analog to the classical orbital motion of electrons is reflected by the wavefunctions $|N\rangle$. In terms of the radial coordinates $\rho$ and $\phi$ one finds the wavefunctions

$$\psi_N = \alpha_N \frac{1}{\sqrt{N!}} \frac{1}{l^N} e^{iN\phi} \rho^N \exp\left(-\frac{\rho^2}{4l^2}\right) \tag{2.29}$$

according to [19], where $\alpha_N$ is a scaling factor. $\psi_N$ are rotational symmetric, their radial probability density is given by

$$\rho|\psi_N|^2 = \alpha_N^2 \frac{1}{N!} \frac{1}{l^{2N}} \rho^{2N+1} \exp\left(-\frac{\rho^2}{4l^2}\right). \tag{2.30}$$

$\rho|\psi_N|^2$ is plotted at a fixed magnetic field in Fig. 2.2 (b). For each $N$ there is only one maximum at

$$\tilde{\rho} = l\sqrt{2N+1}. \tag{2.31}$$

Therefore the physical meaning of $l$ becomes obvious. It is a natural length scale for the expansion of the electron wavefunction in an external magnetic field. It defines the radius $\tilde{\rho}$ of each Landau level orbit by Eq. 2.31. Landau orbits for several radii $\tilde{\rho}$ are plotted in Fig. 2.2 (a). Note that $l$ does not depend on any specific material properties. For common direct current magnetic fields ($B \leq 30\,T$), $l$ is in the range of several nanometers (see Fig. 2.1 (b)).

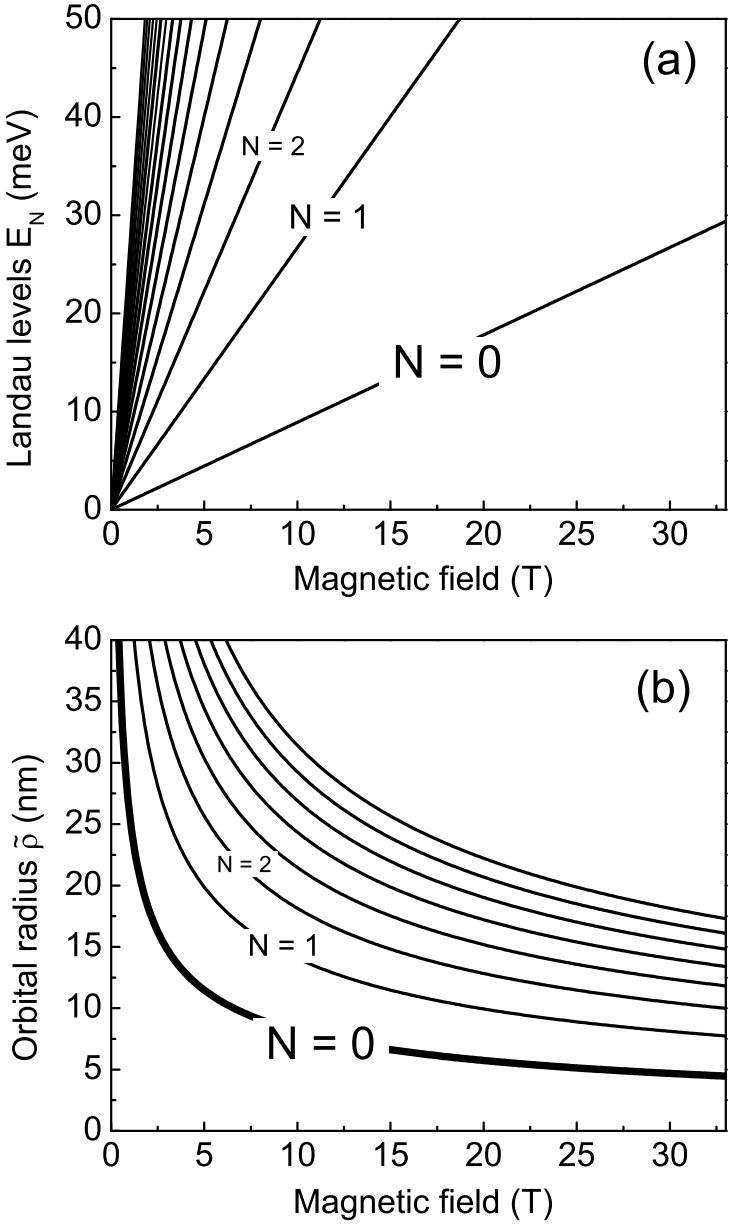


Figure 2.1: (a) Landau level energies $E_N$ for $N = 0, 1, 2...$ in bulk GaAs ($m^* = 0.065\, m$). (b) Magnetic field dependence of the orbital radius $\tilde{\rho}$, for magnetic fields up to $33\, T$. $\tilde{\rho}|_{N=0} = l$

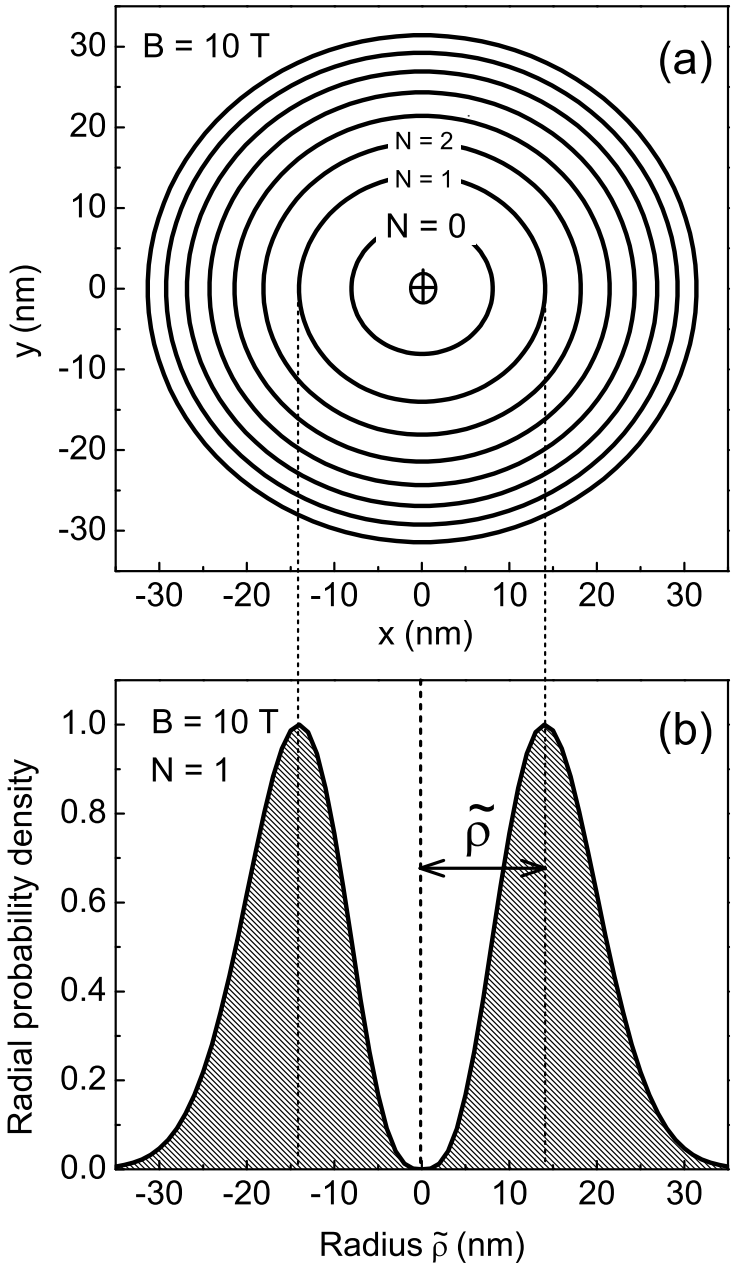


Figure 2.2: (a) Landau level orbits for different quantum numbers $N = 0, 1, 2...$ , plotted in the $xy$-plane. The field of $10\,T$ is aligned in $z$-direction. (b) Density of probability for the electron's wavefunction at $B = 10\,T$ and $N = 1$.

### 2.1.3 Far-infrared radiation

The elementary understanding of cyclotron resonance is the resonant promotion of electrons to higher Landau levels, i.e. from an energy $E_N$ to $E_{N'}$. This transition is excited by a weak FIR field $\boldsymbol{A}_{\mathrm{FIR}}$, conveniently expressed as a superposition of two oppositely circular polarized fields $\boldsymbol{A}^{+}_{\mathrm{FIR}}$ and $\boldsymbol{A}^{-}_{\mathrm{FIR}}$. In dipole approximation, $exp(i\boldsymbol{kr}) \approx 1$, they are given by

$$\boldsymbol{A}^{\pm}_{\mathrm{FIR}} = A_0(\boldsymbol{e}_x \pm i\boldsymbol{e}_y)e^{i\omega t}, \tag{2.32}$$

where $A_0$ is the field amplitude and $\boldsymbol{e}_x$ and $\boldsymbol{e}_y$ are unit vectors in the $x$- and $y$-direction, respectively. $\boldsymbol{A}^{\pm}_{\mathrm{FIR}}$ is included by the same standard substitution, used for Eq. 2.9. Hence, the full Hamiltonian $H$ reads

$$H = \frac{(\boldsymbol{p} - e\boldsymbol{A} - e\boldsymbol{A}^{\pm}_{\mathrm{FIR}})^2}{2m^*} \approx \frac{\boldsymbol{\pi}^2}{2m^*} - \frac{e\,\boldsymbol{\pi}\,\boldsymbol{A}^{\pm}_{\mathrm{FIR}}}{m^*} = H_0 - H_{\mathrm{FIR}}. \tag{2.33}$$

Reusing the ladder operators of Eq. 2.19, $H_{\mathrm{FIR}}$ can be written in an illustrative form:

$$\begin{aligned} H_{\mathrm{FIR}} =& \frac{e}{m^*}(\pi_x A^{\pm}_{\mathrm{FIR},x} + \pi_y A^{\pm}_{\mathrm{FIR},y}) && (2.34)\\ =& \frac{eA_0}{m^*}(\pi_x \pm i\pi_y)e^{i\omega t} && (2.35)\\ =& \frac{eA_0\sqrt{2}\hbar}{m^* l}\, a_{\pm}\, e^{i\omega t} && (2.36)\\ =& \tilde{H}_{\mathrm{FIR}}\, e^{i\omega t}. && (2.37) \end{aligned}$$

The operator of the FIR field is basically the raising $a_+$ or the lowering operator $a_-$ of the Landau level eigenfunctions $|N\rangle$, depending on the particular polarization of incident FIR-radiation.

Fermi's golden rule provides for a periodic perturbation like $H_{\mathrm{FIR}}$ the transition rate

$$\Gamma_{N',N} = \frac{2\pi}{\hbar}\delta(E_N - E_{N'} - \hbar\omega)\left|\langle N|\,\tilde{H}_{\mathrm{FIR}}\,|N'\rangle\right|^2. \tag{2.38}$$

According to $\langle N|\,\tilde{H}_{\mathrm{FIR}}\,|N'\rangle$, the FIR-radiation connects states $|N\rangle$ and $|N \pm 1\rangle$ exclusively, while $\delta(E_N - E_{N'} - \hbar\omega)$ only permits FIR-quantum energies $E_{\mathrm{FIR}} = \hbar\omega$ matching the Landau level energy splitting.

In short, the FIR selection rules are:

$$\begin{aligned} \Delta N &= \pm 1 && (2.39)\\ \Delta E &= \hbar\omega_c = \hbar eB/m^* = E_{\mathrm{FIR}}. && (2.40) \end{aligned}$$

Fixing the FIR wavelength and tuning the magnetic field, a sharp cyclotron resonance at

$$B_{\mathrm{res}} = \frac{m^* \omega_{\mathrm{FIR}}}{e} \tag{2.41}$$

is expected.

$B_{\mathrm{res}}$ and $\omega_{\mathrm{FIR}}$ are experimentally well accessible parameters, especially for FIR lasers, where the FIR lines are spectrally very narrow. By measuring $B_{\mathrm{res}}$ and $\omega_{\mathrm{FIR}}$ the effective electron mass can be estimated to:

$$m^* = \frac{eB}{\omega_{\mathrm{FIR}}}. \tag{2.42}$$

### 2.1.4 Kohn's theorem

In the previous considerations only single electrons were discussed. For a number of $N$ electrons in a homogeneous magnetic field, electron-electron interaction $u_{ee}$ becomes important and Eq. 2.12 has to be extended to describe the interacting system of electrons:

$$H = \frac{1}{2m^*} \sum_i^N \boldsymbol{\pi}_i^2 + \sum_{i,j}^N u_{ee}(\boldsymbol{r}_i - \boldsymbol{r}_j). \tag{2.43}$$

In principle, it requires sophisticated approximations to solve Eq. 2.43. However, if only CR transitions are considered, a simple analytical approach is sufficient.

The basic idea is to decouple the center of mass motion from the internal degrees of freedom $(\boldsymbol{r}_i - \boldsymbol{r}_j)$. The collective momentum of the electron system is given by

$$\boldsymbol{\pi} = \sum_i \boldsymbol{\pi}_i. \tag{2.44}$$

In analogy to the single particle momentum (see Eq. 2.19), raising and lowering operators

$$A_\pm = \frac{l}{\sqrt{2}\hbar} (\pi_x \pm i\pi_y) \tag{2.45}$$

can be defined. Independent of the exact form of $u_{ee}(\boldsymbol{r_i} - \boldsymbol{r_j})$ one obtains

$$\frac{d\pi}{dt} = \frac{i}{\hbar}[H, \boldsymbol{\pi}] = -\frac{e}{m^*} \boldsymbol{\pi} \times \boldsymbol{B} \tag{2.46}$$

and therewith

$$[H, A_\pm] = \pm \hbar \omega_c A_\pm. \tag{2.47}$$

Although neither the ground state $|N=0\rangle$ nor its energy $E_0$ are known, Eq. 2.47 serves an excited eigenstate

$$|N=1\rangle = A_+ \,|N=0\rangle\,, \tag{2.48}$$

with an eigenenergy

$$E_1 = E_0 + \hbar\omega_c. \tag{2.49}$$

The same energy difference is obtained for any higher energy state $E_{_N}$ and its closest excited state $E_{_{N+1}}$

$$\Delta E = E_{_{N+1}} - E_{_N} = \hbar\omega_c. \tag{2.50}$$

The perturbation by the FIR-radiation $H_{\text{FIR}}$ is introduced in analogy to Eq. 2.37, and results in

$$H_{\text{FIR}} = \frac{e\hbar\epsilon_0}{i\omega l m^*}\, A_\pm\, e^{i\omega t}. \tag{2.51}$$

Thus, $H_{\text{FIR}}$ provides the same selection rules in a system of interacting electrons as for a single electron (see Sec. 2.1.3):

$$\Delta N = \pm 1, \tag{2.52}$$

$$\Delta E = \hbar\omega_c = \hbar eB/m^* = E_{\text{FIR}}. \tag{2.53}$$

This means that the cyclotron frequency, and hence the effective mass obey Kohn's theorem [20], i.e. they do not depend on the electron-electron interaction potential $u_{ee}$

$$\omega_c|_{u_{ee}\neq 0} = \omega_c|_{u_{ee}=0}, \tag{2.54}$$

$$m^*|_{u_{ee}\neq 0} = m^*|_{u_{ee}=0}. \tag{2.55}$$

However Kohn's theorem is valid for systems with one single cyclotron frequency $\omega_c$ only. For more than one cyclotron frequency, like it is the case for spin-split CR or nonparabolic conduction bands, electron-electron interaction affect the effective mass and consequently CR is able to reveal many-body effects.

## 2.2 The classical Drude model

Besides the quantum mechanical picture, a short comment on the classical treatment of cyclotron resonance is illustrative. It provides an comparatively intuitive approach to the electron dynamics. Within this classical description two widely used parameters, the electron mobility $\mu$ and the electron scattering time $\tau$ were originally defined.

Under the influence of an electric field $\boldsymbol{E}$ and a magnetic field $\boldsymbol{B}$, the Drude model [21] describes the electron at a velocity $\boldsymbol{v}$ by the following equation of motion

$$m^* \frac{d\boldsymbol{v}}{dt} + \frac{m^* \boldsymbol{v}}{\tau} = -e\boldsymbol{E} - e(\boldsymbol{v} \times \boldsymbol{B}), \tag{2.56}$$

where $\tau$ is the time between two scattering events. The scattering is often expressed by the means of the electron mobility

$$\mu = e\tau/m^*. \tag{2.57}$$

The itinerant electrons of density $n_e$ produce a current

$$\boldsymbol{J} = n_e e \boldsymbol{v}, \tag{2.58}$$

which, in turn, defines a conductivity $\sigma$

$$\boldsymbol{J} = \sigma \boldsymbol{E}. \tag{2.59}$$

Assuming an orientation of the magnetic field in $z$-direction

$$\boldsymbol{B} = \begin{pmatrix} 0 \\ 0 \\ B \end{pmatrix}, \tag{2.60}$$

and the oscillatory components of the electric field

$$\boldsymbol{E} = \boldsymbol{E}_{\mathrm{FIR}\pm} = \begin{pmatrix} 0 \\ \cos(\omega t) \\ \pm\sin(\omega t) \end{pmatrix} \tag{2.61}$$

one finds the frequency dependent conductivity for circular polarized FIR-radiation by solving Eq. 2.56

$$\sigma_\pm(\omega) = \sigma_0 \left[ \frac{1}{1 + (\omega \mp \omega_c)^2 \tau^2} - i \frac{(\omega \mp \omega_c)\tau}{1 + (\omega \mp \omega_c)^2 \tau^2} \right] = \sigma_\pm^{'} + i\sigma_\pm^{''}, \tag{2.62}$$

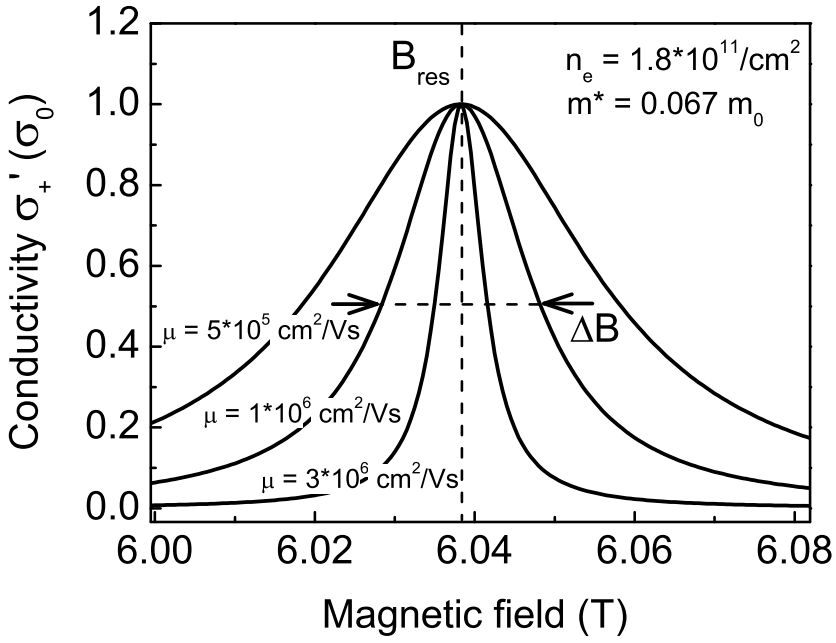


Figure 2.3: Classical cyclotron resonances of the conductivity $\sigma_+^{'}$ in units of $\sigma_0$, for three different electron mobilities $\mu$.

where the steady state conductivity is given by $\sigma_0 = \frac{n_e e^2 \tau}{m^*}$.

According to classical electrodynamics the power absorption is proportional to the real part of the conductivity

$$P_{abs\pm} \propto \sigma_{\pm}^{'} \boldsymbol{E}_{\mathrm{FIR}\pm}^2. \tag{2.63}$$

For a fixed FIR energy $E_{\mathrm{FIR}}$ and a variable magnetic field $B$ the real part $\sigma_{\pm}^{'}$ of Eq 2.62 is expressed by

$$\sigma_{\pm}^{'}(B) = \sigma_0 \left[ \frac{1}{1 + (B \mp \frac{E_{\mathrm{FIR}} m^*}{\hbar e})^2 \mu^2} \right]. \tag{2.64}$$

Assuming $B > 0$, $\sigma_+^{'}(B)$ is of Lorentzian shape (see Fig. 2.3), with a single cyclotron resonance at

$$B_{\mathrm{res}} = \frac{m^* E_{\mathrm{FIR}}}{e\hbar}. \tag{2.65}$$

The second component of the conductivity, $\sigma_-^{'}(B)$, causes a continuous background only, which is negligibly small for narrow resonances. Therefore, $\boldsymbol{E}_{\mathrm{FIR}+}$ is called the *cyclotron active* component of the FIR-radiation. For $B < 0$ all signs are inverted and therefore $\boldsymbol{E}_{\mathrm{FIR}-}$ is cyclotron active.

One obtains the same formula for the effective mass as derived in Sec. 2.1.3,

$$m^* = \frac{eB}{\omega_{\text{FIR}}}. \tag{2.66}$$

Furthermore, the width of the cyclotron-resonance line contains valuable information. The half-width of the half maximum $\Delta B/2$ of the cyclotron active component of $\sigma_{\pm}^{'}(B)$ is directly related to the electron mobility and thus to the electron scattering time.

$$\frac{\Delta B}{2} = \frac{1}{\mu} = \frac{m^*}{e\tau}. \tag{2.67}$$

# 3

# Optical transitions

In this chapter optical transitions in the visible or near-infrared spectral region ($1 - 3\ eV$) are discussed in order to provide basics for the optical detection techniques, used in ODCR.

Photon energies, exceeding the band-gap energy, enable interband transitions, i.e., transitions between the valence- and the conduction-band. The generation of electron-hole pairs is the fundamental difference to intraband transitions. However, the involvement of holes complicates the situation as the GaAs valence band is of $p$-like character, which makes it a system of six bands.

In the following the most relevant GaAs conduction and valence bands will be discussed briefly. In that context, optical dipole selection rules will be developed.

## 3.1 GaAs band structure

GaAs is a zinc-blende structure semiconductor. Its electronic bands, schematically shown in Fig. 3.1, obey the typical structure specific symmetries, noted according to the common terminology ($\Gamma_6$, $\Gamma_7$, $\Gamma_8$). In contrast to the $s$-like conduction band, the valence band could not be described by one parabolic band only. The $p$-like valence-band (i.e. orbital angular momentum $l = 1$) requires to include spin-orbit interaction so that the spin $\boldsymbol{s}$ is not a good quantum number any more, instead the total angular momentum $\boldsymbol{j} = \boldsymbol{l} + \boldsymbol{s}$ has to be used. For $l = 1$ the total angular momentum can take two possible values $j = 3/2$ and $j = 1/2$ and its $z$-component the values

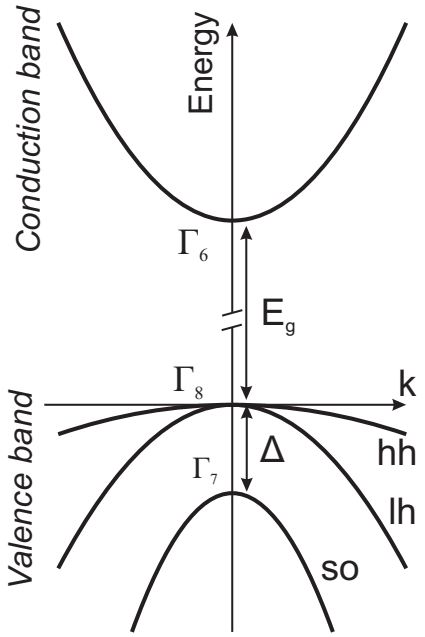


Figure 3.1: Schematic depiction of the most relevant, two-fold spin-degenerate zinc-blende structure bands in $k$-space: The $\Gamma_6$ conduction band the heavy-hole band (hh, $\Gamma_8$), the light-hole band (lh, $\Gamma_8$) and the split-off band (so, $\Gamma_7$).

$j_z = j, j-1, ..., -j+1, -j$. Thus one finds six valence band functions $|j, j_z>$:

$$\begin{aligned}
|\mathrm{hh}, +\rangle &= |3/2, 3/2\rangle & \Gamma_8 \\
|\mathrm{hh}, -\rangle &= |3/2, -3/2\rangle & \Gamma_8 \\
|\mathrm{lh}, +\rangle &= |3/2, 1/2\rangle & \Gamma_8 \\
|\mathrm{lh}, -\rangle &= |3/2, -1/2\rangle & \Gamma_8 \\
|\mathrm{so}, +\rangle &= |1/2, 1/2\rangle & \Gamma_7 \\
|\mathrm{so}, -\rangle &= |1/2, -1/2\rangle & \Gamma_7
\end{aligned} \tag{3.1}$$

The $\Gamma_7$ band is shifted to lower energies by $\Delta = 0.33eV$ in respect to the $\Gamma_8$ bands. Hence, it is called the *split-off* band. The $\Gamma_8$ *heavy-* and *light*-hole bands are named according to their different effective masses.

The standard treatment of the total angular momenta of the holes slightly obscures the $p$-like valence band-character. The $z$-component of the total hole angular momentum $j_z$ is widely called the hole spin $s_{hh}$ and $s_{lh}$. Hence, according to Eq. 3.1, one finds $s_{hh} = \pm 3/2$ for heavy holes and $s_{lh} = \pm 1/2$ for light holes.

## 3.2 Transition-matrix elements

The photoluminescence intensity is defined by both, the population of the initial states and the transition rates [22].

The transitions rates are given by Fermi's golden rule, very similar to the previously discussed FIR absorption (see Eq. 2.38). In dipole approximation the radiation is described by a periodic vector potential $\boldsymbol{A} = A_0\,\boldsymbol{e}\,e^{i\omega t}$. Thus, the transition rate between the initial state $|\psi_i\rangle$ with the energy $E_i$ and the final state $|\psi_f\rangle$ with the energy $E_f$ reads

$$\Gamma_{i,f} = \frac{2\pi A_0^2 e^2}{m^{*2}\hbar}\delta(E_f - E_i - \hbar\omega)\,|\langle\psi_f|\,\boldsymbol{e}\,\boldsymbol{p}\,|\psi_i\rangle|^2\,, \tag{3.2}$$

with the total wavefunctions

$$|\psi_n\rangle = |F_n\rangle\,|u_n\rangle\,, \tag{3.3}$$

where $|F_n\rangle$ is the envelope function and $|u_n\rangle$ is the cell periodic part of the Bloch-function [17].

The transition rate in Eq. 3.2 is dominated by two factors. Firstly, the $\delta$-function which provides the energy conservation, and secondly, the dipole transition-matrix element whose role is analyzed in the following. Inserting Eq. 3.3 into the dipole matrix element, it expands in

$$\langle\psi_f|\,\boldsymbol{e}\,\boldsymbol{p}\,|\psi_i\rangle = \langle u_i|u_f\rangle\,\langle F_i|\boldsymbol{e}\,\boldsymbol{p}|F_f\rangle + \langle u_i|\boldsymbol{e}\,\boldsymbol{p}|u_f\rangle\,\langle F_i|F_f\rangle\,. \tag{3.4}$$

The two summands describe essentially different transitions.

The first summand requires initial and final states within the same band $|u_i\rangle = |u_f\rangle$, otherwise it vanishes. Therefore, it describes intraband transitions and the matrix element $\langle F_i|\boldsymbol{e}\,\boldsymbol{p}|F_f\rangle$ determines the corresponding intraband selection rules. In section 2.1.3 such rules are derived for transitions between Landau levels.

The second summand is related to interband transitions. The Bloch function matrix element $\langle u_i|\boldsymbol{e}\,\boldsymbol{p}|u_f\rangle$ is responsible for the polarization of the emitted light [23]. It designates circularly polarized emission for heavy-hole transitions

$$|1/2,+1/2\rangle \xrightarrow{\sigma_-} |3/2,+3/2\rangle \tag{3.5}$$

$$|1/2,-1/2\rangle \xrightarrow{\sigma_+} |3/2,-3/2\rangle\ , \tag{3.6}$$

where $\sigma_\pm$ denote left- and right-hand circularly polarized photons.

The envelope function matrix element $\langle F_i|F_f\rangle$ stands for momentum conservation in the bulk crystal, e.g. the free carrier wavevector $\boldsymbol{k}_\alpha$ fulfills

$$\boldsymbol{k}_i = \boldsymbol{k}_f. \tag{3.7}$$

In the case of quantum confinement, the envelope-matrix element provides a selection rule for the subband wavefunctions of the respective confinement potential. In the limit of very strong confinement, the subbands of the initial and the final state have to be identical to allow dipole transitions [23].

## 3.3 Excitons

Before recombination electrons and holes can form excitons, Hydrogen-atom like complexes bound by Coulomb interaction. The PL emission of such recombinations is lowered in energy by the exciton binding energy. As all the experiments are carried out in magnetic fields, it is convenient to introduce a vector potential $\boldsymbol{A}(\boldsymbol{r}) = B/2(-y, x, 0)$ immediately. The Hamiltonian for an electron (denoted by the index "$e$") and a hole (denoted by "$h$"), including Coulomb interaction, thus reads

$$H = \frac{(\boldsymbol{p}_e - e\boldsymbol{A}(\boldsymbol{r}_e))^2}{2m_e^*} + \frac{(\boldsymbol{p}_h + e\boldsymbol{A}(\boldsymbol{r}_h))^2}{2m_h^*} + \frac{e^2}{4\pi\epsilon|\boldsymbol{r}_e - \boldsymbol{r}_h|}. \tag{3.8}$$

It is common to treat the exciton problem in the center of mass coordinate $\boldsymbol{\rho}$ and the relative coordinate $\boldsymbol{r}$

$$\boldsymbol{r} = \boldsymbol{r}_e - \boldsymbol{r}_h, \tag{3.9}$$

$$\boldsymbol{\rho} = \frac{m_e^*\boldsymbol{r}_e + m_h^*\boldsymbol{r}_h}{m_e^* + m_h^*}, \tag{3.10}$$

with the center of mass wavevector

$$\boldsymbol{K} = \boldsymbol{k}_e - \boldsymbol{k}_h. \tag{3.11}$$

This enables one to write down a factorized wavefunction

$$\psi(\boldsymbol{r}, \boldsymbol{\rho}) = \exp\left(i\left[\boldsymbol{K} - \frac{e}{\hbar}\boldsymbol{A}(\boldsymbol{r})\right]\boldsymbol{\rho}\right) F(\boldsymbol{r}). \tag{3.12}$$

Applying Eq. 3.8 to Eq. 3.12 one obtains [1]

$$\left[-\frac{\hbar^2}{2\mu^*}\nabla^2 - \frac{e^2}{4\pi\epsilon r} + ie\hbar\left(\frac{1}{m_e^*} - \frac{1}{m_h^*}\right)\boldsymbol{A}(\boldsymbol{r})\nabla\right. \tag{3.13}$$

$$\left. + \frac{e^2}{2\mu^*}A(\boldsymbol{r})^2 - \frac{2e\hbar}{m_e^* + m_h^*}\boldsymbol{A}(\boldsymbol{r})\boldsymbol{K} + \frac{\hbar^2 K^2}{2(m_e^* + m_h^*)}\right] F(\boldsymbol{r}) \tag{3.14}$$

$$= EF(\boldsymbol{r}), \tag{3.15}$$

with the reduced exciton mass

$$\frac{1}{\mu^*} = \frac{1}{m_e^*} + \frac{1}{m_h^*}. \tag{3.16}$$

The transformation into relative coordinates reveals the problem of a hydrogen atom in the first two terms

$$\left[-\frac{\hbar^2}{2\mu^*}\nabla^2 - \frac{e^2}{4\pi\epsilon r}\right] F_{\tilde{n},\tilde{l},\tilde{m}}(\boldsymbol{r}) = E_{\tilde{n}} F_{\tilde{n},\tilde{l},\tilde{m}}(\boldsymbol{r}), \tag{3.17}$$

with the typical set of quantum numbers: the angular momentum quantum number $\tilde{l}$, its projection on the $z$-axis $\tilde{m}$ and the principal quantum number $\tilde{n}$. For $B = 0$ all other terms vanish and only the hydrogen problem remains, with the exact eigenvalues

$$E_{\tilde{n}} = -\frac{Ry^*}{\tilde{n}^2} \qquad (\tilde{n} = 1, 2, ...), \tag{3.18}$$

$$Ry^* = \frac{\mu^* e^4}{32\pi^2\hbar^2\epsilon^2} = \frac{\hbar^2}{2\mu^* a_B^{*2}}. \tag{3.19}$$

For the full Hamiltonian of Eq. 3.15 there is no analytical solution. Approximations can be found for low magnetic fields $\hbar\omega_c \gg Ry^*$ or high magnetic fields $\hbar\omega_c \ll Ry^*$, respectively.

Generally $\boldsymbol{K}$ is expected to be small because the photoexcited exciton only carries the small momentum of the photon. Thus, the fifth and sixth term in Eq. 3.15 can be neglected. The third term vanishes for s-states [12], so that only the hydrogen-like Hamiltonian and the fourth term $\frac{e^2}{2\mu^*}A^2$ remain. For small fields the hydrogen Hamilton is dominant and the magnetic field is treated as a perturbation. So, the exciton energy in the ground state $|n = 1\rangle$ is

$$E = Ry^* + \frac{e^2}{4\mu^*}B^2 \left\langle \tilde{n} = 1|\boldsymbol{r}|\tilde{n} = 1\right\rangle^2 = Ry^* + \frac{e^2}{4\mu^*}B^2 a_B^{*2} = Ry^* + \kappa\, B^2, \tag{3.20}$$

[1] Compare [12, 24].

where $\kappa = \frac{e^{*2}a_B^2}{4\mu^*}$. As a result, the exciton energy exhibits a *diamagnetic shift* which is proportional to $B^2$ and the excitons effective Bohr radius for sufficiently small magnetic fields.

At high magnetic fields, the Coulomb interaction is small compared to $\hbar\omega_c$. Therefore the exciton binding energy is treated as a perturbation and electrons and holes experience approximately a linear field dependence consequently.

# 4
# Experimental setup

The sample is located in a single coil magnet cryostat in Faraday configuration (see Fig. 4.1). It could be exposed either to a bath of liquid helium or to helium gas at $T = 2.2\ K$. The single coil construction allows high magnetic fields of up to $17\,T$ but lacks direct optical access by glass windows.

## 4.1 FIR transmission

The FIR-radiation is generated by a $CO_2$-laser pumped FIR-laser, which can be filled with different gases. In this study only methanol is used for that purpose, as it provides highest intensities and best stability. The FIR-laser generates a spectrum of discrete, narrow lines, not wider than $0.001\,meV$. The strongest and most stable line is $E_{\mathrm{FIR}} = 10.433\,meV$. The laser is stabilized by a separate stabilization unit. It corrects the tuning of the laser cavity according to the current laser power. A measure of the current laser power is provided by the signal of a pyroelectric detector. It is illuminated by a small fraction of FIR radiation, split off by a beamsplitter B1 from the main FIR beamline (see Fig. 4.1). As pyroelectric detectors can detect differences in FIR intensity only, the reference beam has to be chopped by the mechanical chopper C1. For FIR transmission experiments the main FIR beamline is interrupted by another chopper (C2), sandwiched by two teflon lenses (L1 and L2). The chopper is placed in the focus of L1 and L2, so that the FIR beam can pass the narrow chopper blades, which allow high frequency operation up to $4\ kHz$. After L2, the parallel FIR beam is coupled to a copper wavequide W1, then reflected by a gold mirror M2 and guided to the cryostat through a teflon window. In there a second waveguide W2, made from stainless steel, transmits the FIR radiation to the back side of the sample.

On the front side of the sample there is a polished carbon resistor to detect the transmitted FIR radiation (case (a) in Fig. 4.1). A lock-in amplifier

measures the change of the voltage drop at the carbon resistor at the chopping frequency $f_{\mathrm{ref}}$.

## 4.2 FIR-ODCR

For ODCR, the FIR excitation is basically the same as in FIR transmission experiments (see Fig. 4.1). However, for continuous wave (CW) FIR-ODCR the main FIR beamline is not chopped. That means lenses L1 and L2 and the chopper C2 can be omitted. Instead a mechanical shutter is used to block the FIR beamline.

The carbon resistor at the front side of the sample is exchanged by an optical detection system: Step index fibers of 200 $\mu m$ core diameter are guided to the sample chamber, one fiber for the excitation (blue) and one for PL detection (orange). The excitation fiber illuminates the sample unfocused to provide homogeneous excitation conditions. It is feeded with two laser lines of 633 $nm$ and 785 $nm$, generated by a HeNe-laser and a diode-laser respectively. The PL is collected from a spot of the sample of less than 500 $\mu m$ by a lense L3 with 6 $mm$ diameter and 1 $cm$ focal length. With the sample in the focal plane, the parallel PL beam passes a $\lambda/4$-plate and a linear polarizer at a fixed relative angle of 45°, enabling circular polarization resolved measurements. In order to change the orientation of polarization, the electromagnets sign of current is inverted. A second lense L4 focuses the PL into the second fiber for PL detection (orange). This fiber is guided to a system of two achromats (L5 and L6). It focuses the PL on a 550 $cm$ grating spectrometer, equipped with different detectors. A liquid nitrogen Si-CCD (1) is used for CW-PL measurements.

ODR measurements using discrete FIR light sources are based on scanning the magnetic field and comparing PL spectra, with and without FIR-radiation at each field. In a typical measurement process, the magnet is ramped to the desired field $B$, stopped and stabilized. Then one pure PL spectrum is measured $I_{\mathrm{PL}}(E,B)$, where $E$ is the photon energy. Subsequently a mechanical shutter in the FIR beamline is opened and another spectrum $I_{\mathrm{PL}}^{\mathrm{FIR}}(E,B)$ is recorded under additional FIR illumination. The modifications of the PL, due to FIR-radiation, sometimes called the *modulation*, can be visualized by the difference of the PL intensities of the two PL spectra

$$\mathrm{Modulation}(E,B) = I_{\mathrm{PL}}(E,B) - I_{\mathrm{PL}}^{\mathrm{FIR}}(E,B). \tag{4.1}$$

For the sake of clarity, it is convenient to condense the complex ODR data

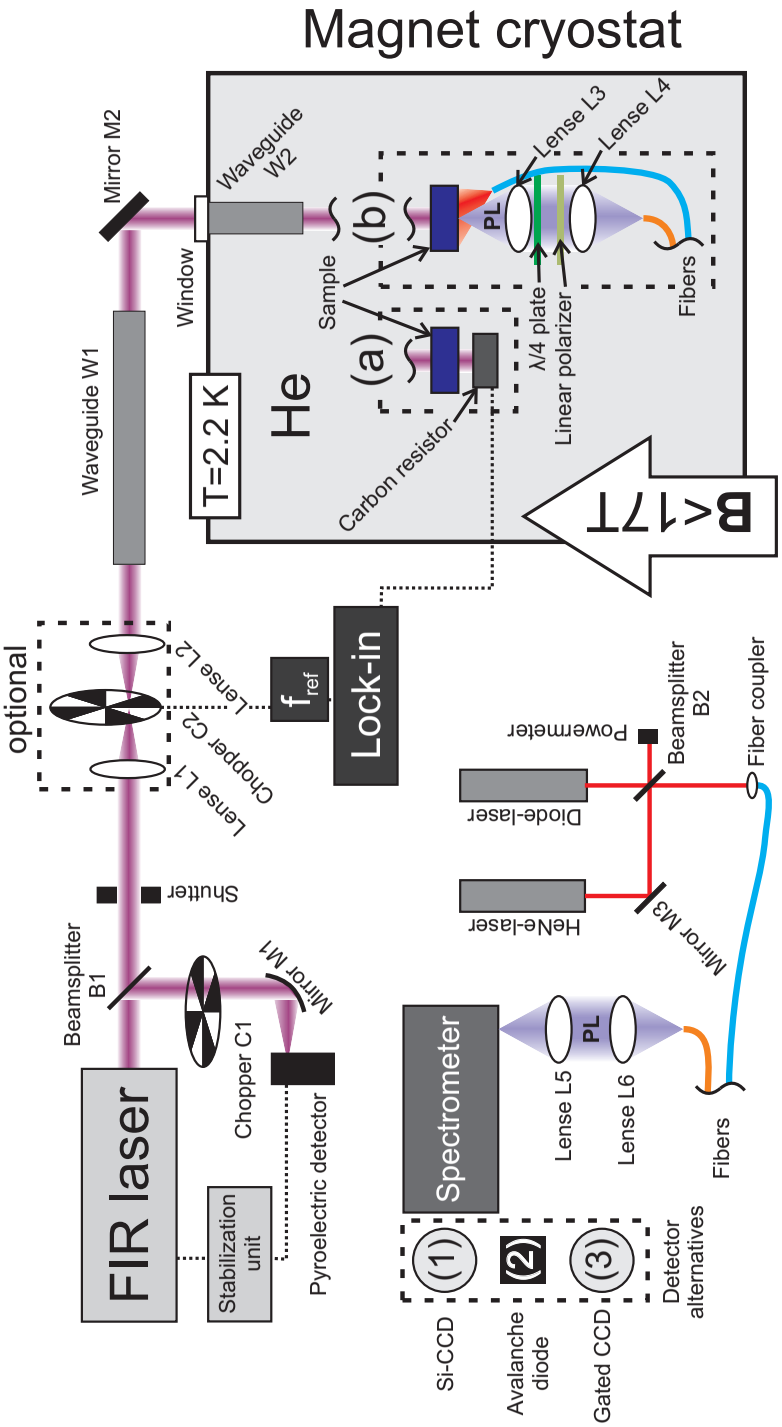


Figure 4.1: Schematic depiction of the experimental setup for FIR transmission (a) and ODCR (b).

to a simple one dimensional function ODR $(B)$, according to

$$\mathrm{ODR}\,(B) = \frac{\int_{E_1}^{E_2} \left| I_{\mathrm{PL}}(E,B) - I_{\mathrm{PL}}^{\mathrm{FIR}}(E,B) \right| \mathrm{d}E}{\int_{E_1}^{E_2} I_{\mathrm{PL}}(E,B)\,\mathrm{d}E}. \tag{4.2}$$

$E_1$ and $E_2$ can be chosen to cover the whole PL range, or only single lines in the spectrum, depending on the respective analytical needs. ODR $(B)$ is very useful, to track resonances and allows a straight forward data comparison with less complex detection techniques, like FIR transmission data.

Time dependent FIR-ODCR requires fast FIR modulation. The mechanical shutter is opened permanently and the modulation is done by the system of chopper C2 and lenses L1 and L2 (see Fig. 4.1). The chopping frequency of 4 $kHz$ enables FIR modulation times, shorter than 250 $\mu s$. For the PL detection either an avalanche photodiode (2) or a gated CCD (3) are used. Both are triggered by the chopper frequency $f_{\mathrm{ref}}$.

# 5 The sample

For any experiment, perturbations caused by technical imperfections are most likely counterproductive and should be reduced to a minimum. According to the sample, technical imperfections are found in two steps of the production process. The first is related to the design of the sample itself. Naturally there are structural designs fitting differently well to the experimental challenges. The second aspect is about how precise the structural design can be put into practice, i.e. imperfections in the growth process unavoidably generate impurities. It is about a good sample design and a well working production process, to reduce impurity effects to a minimum. A low number of impurities is reflected by large electron mobilities $\mu$, which is directly related to long electron scattering times $\tau$, see Eq. 2.57.

In this work a GaAs/AlGaAs heterojunction is investigated. Within this chapter its structure is discussed and a motivation is developed, why this sample is a good choice to study optically detected electron-cyclotron resonance.

## 5.1 The high-mobility single heterojunction

The sample is grown by molecular beam epitaxy (MBE). On a (001) oriented GaAs substrate layers of different $Al_xGa_{1-x}As$-alloys are deposited epitaxially. This is a good starting point for two-dimensional band-gap engineering: On the one hand, the growth process in layers favors intentional alloy variations along the growth direction ($z$-direction), while maximal homogeneity along the remaining directions is assured. On the other hand the choice of $Al_xGa_{1-x}As$ is very convenient. GaAs is very popular in both, technical applications and basic research so that its production is well developed. A driving force behind that attention is the virtually identical lattice constants of AlAs and GaAs, while the band-gaps are considerably different. Thus varying the Al content $x$ of the $Al_xGa_{1-x}As$ alloy allows to control the

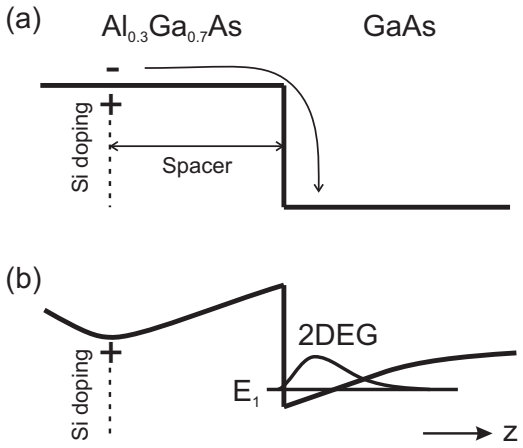


Figure 5.1: Conduction band of a modulation doped GaAs/$Al_{0.3}Ga_{0.7}As$ heterojunction, with the electrons at the donors (a), and after dropping to the GaAs layer (b).

band-gap without suffering from too strong strain effects. Thereby artificial potential wells along the $z$-direction can be created, confining electrons to narrow regions of a few $nm$, without restricting the movement in the $x$-$y$ plane. Quasi two-dimensional carriers are the result.

The electron confinement can affect the mobility strikingly. Doping is essentially needed to introduce a certain density of resident electrons. However, the inserted dopants act as impurities, undoing all efforts of clean production. The solution is a spacial separation of the dopants and the electrons, called remote- or modulation doping. In a bulk crystal such a separation is not possible, only heterostructures enable such a technique.

The sample investigated in this work is a single GaAs/$Al_{0.3}Ga_{0.7}As$ heterojunction (HJ). The Si-doping sheet is situated in the $Al_{0.3}Ga_{0.7}As$ barrier, 80 $nm$ away from the GaAs/$Al_{0.3}Ga_{0.7}As$ interface, as shown in Fig. 5.1 (a). The electrons, supplied by the Si-doping sheet, tunnel to the energetically favorable GaAs region. The charge redistribution forms a potential notch near the HJs interface, where the electrons are trapped (Fig. 5.1 (b)) in a range of only about 20 $nm$. In the $x$-$y$ plane the electrons are virtually not influenced. The electrons form a so called *two-dimensional-electron gas* (2DEG). Compared to a quantum well, the single heterojunction usually provides higher mobilities. For a quantum well a reverse heterojunction is needed, which implies additional scattering.

In summary, the modulation doping together with the GaAs material system and the simple HJ enable high mobility values of more than $3 \cdot 10^6$ $cm^2/Vs$. Essentially this high mobility makes the sample a suitable

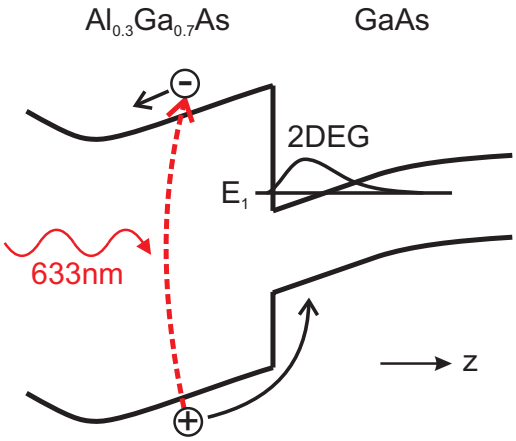


Figure 5.2: 2DEG depletion in the vicinity of the GaAs/$Al_{0.3}Ga_{0.7}As$ heterojunction. Conduction- and valence bands are schematically depicted in growth direction ($z$). The above barrier excitation is indicated by HeNe-laser excitation (633 $nm$).

choice to study narrow cyclotron resonances. The optical detection of cyclotron resonance is promoted by the choice of GaAs, as it has a direct band-gap at conveniently measurable wavelengths.

## 5.2 Variable electron density

In the studied sample, the charge redistribution balances at a 2DEG density of $n_e = 2 \cdot 10^{11} cm^{-2}$. However, the electron density can be modified by above barrier illumination, i.e. excitation by photons of energies, exceeding the $Al_{0.3}Ga_{0.7}As$ band-gap. The photogenerated electron hole pairs are separated by the electrostatic field: The electrons drift away from the HJ, attracted by the ionized Si donors and the holes travel in the opposite direction and drop in the 2DEG area of GaAs layer (Fig. 5.2). Here the, additional holes cause a depletion of the 2DEG and - assuming a sufficiently constant excitation intensity - a new equilibrium state at reduced 2DEG density is achieved. Varying the above barrier illumination intensity controls the 2DEG density efficiently and a reducing the density by a factor of two requires not more than 1 $mW/cm^2$ excitation power (see Fig. 5.3).

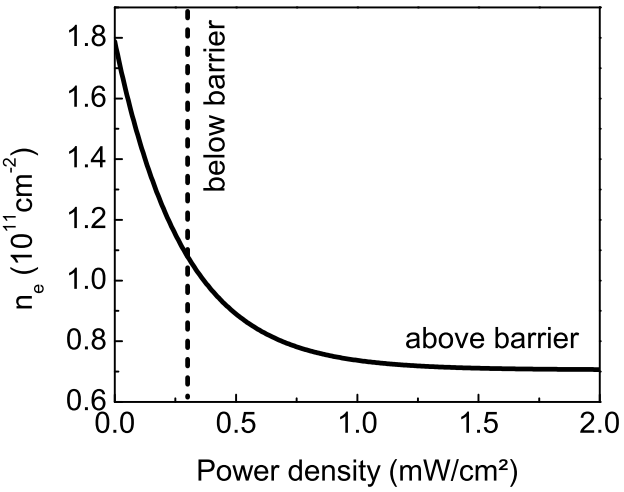


Figure 5.3: An exponential fit of the $n_e$-variation by above barrier illumination by a HeNe-laser (solid line). The dashed line shows the constant below barrier power density by $785nm$ light.

## 5.3 Comment on closely related structures

The sample discussed before is sometimes confused with other closely related heterojunctions. When reviewing literature in this thesis, it will be necessary to comment on such structures. They consists of a similar modulation doped GaAs/AlGaAs heterojunction but are modified by an additional $p$-type doping sheet in the GaAs layer. It is commonly placed at a distance of about 10 to 30 $nm$ away from the heterojuction. The acceptors, usually Be, bind holes which form the dominant optical recombination channel with the 2DEG electrons. While the 2DEG mobility is not too strongly affected by the acceptors, the optical recombination is changed drastically. Thus, optical experiments on samples with and without $p$-type doping in the GaAs layer are only hardly comparable. However, in literature it is not always clearly described, if the structure contains Be-doping or not, which might confuse the reader.

# 6 Magneto-photoluminescence

In this chapter, a detailed magneto-photoluminescence analysis of the GaAs/-AlGaAs HJ is presented. A good understanding of the plain PL is essential to interpret the PL modification by FIR radiation, discussed in later chapters.

The magneto-PL analysis of GaAs/AlGaAs HJs has gone through a vivid history of high attention and partly contradictory interpretations. A short summary with focus on the PL mechanism should be given in the following.

## 6.1 Previous publications

In 1985 a so far not reported PL line was measured in liquid phase epitaxy grown GaAs/AlGaAs HJs by Yuan et. al. [25]. By etching off sample layers in a controlled manner, the authors assigned this PL line to recombinations of electrons, confined in the potential notch at the interface, with holes in the GaAs layer. Probably related to the initial letter of *heterojunction*, the authors introduced the name $H$-band and since that it is regularly used to describe similar PL lines. In the following, the MBE growth technique provided samples of considerably higher quality with modulation and delta doping layers. The technical progress assisted increasing physical interest, which probably reached its peak in 1990, when the integer- and the fractional quantum Hall effect in PL attracted high attention [4, 5]. At the same time, less attention was paid to the fact, that actually two different types of GaAs/AlGaAs HJs were used since 1990. One had a $p$-type doping layer in the GaAs and the other was grown without such a layer of acceptors (see Sec. 5.3). The delta doping layer of the former sample type commonly consisted of Be-atoms in the vicinity of the GaAs/AlGaAs interface, "in order to maximize the efficiency of the radiative recombination of the 2D electrons" [26]. Magneto-PL studies show recombinations of several Landau levels, typical for electron gases of densities of several $10^{11}$ $cm^{-2}$. Transitions from the *second subband*, i.e. the second state of the confinement potential,

were identified without doubt as well. Simultaneously, magneto-PL studies on Be-free HJs were performed. Although the $p$-type Be doping was originally introduced as a technical additive to supply extra holes for optical recombinations only, it considerably modifies the PL compared to samples with a pure GaAs layer. An essential difference lies in the striking PL discontinuities [4] at certain magnetic fields, observed in the pure samples without a Be-layer. This phenomenon was initially used as a tool to proof the optical detection of the quantum Hall effect, while the physical mechanism behind the discontinuities played a secondary role.

Since this initial description, different approaches were presented to explain the PL discontinuities, in which not only the reason for the PL intensity redistribution is explained differently, but even the origin of the respective PL lines is attributed to different recombination processes.

While there is no doubt about the $H$-band character of the low energy PL band, there is some contradiction about the high energy band. Initially, in the late 1980s it was assigned to free GaAs excitons [27, 28]. Later, from 1990 on, the high energy band was attributed to recombinations from the second HJ subband, analogous to PL interpretations of the Be-doped samples [4, 29]. The PL discontinuities were explained by different screening effects of either completely filled Landau levels, being inert for recombination, or partially filled Landau levels, where screening is active and an increased electron-hole wavefunction overlap favours recombination. In the year 2000, the original exciton-like PL explanation was revived [6] and a phenomenological model of an exciton dissociation process was established [7]. Today, a suitable theoretical treatment is still not available.

In the following sections, the HJs PL is discussed in the frame of the most recent model, the exciton dissociation mechanism. It includes the coexistence of 2DEG-hole recombinations ($H$-band) and excitonic transitions from the wide GaAs sheet. From the very first, the terminology according to this interpretation is used, while experimental indications for its correctness are gathered step by step during the discussion.

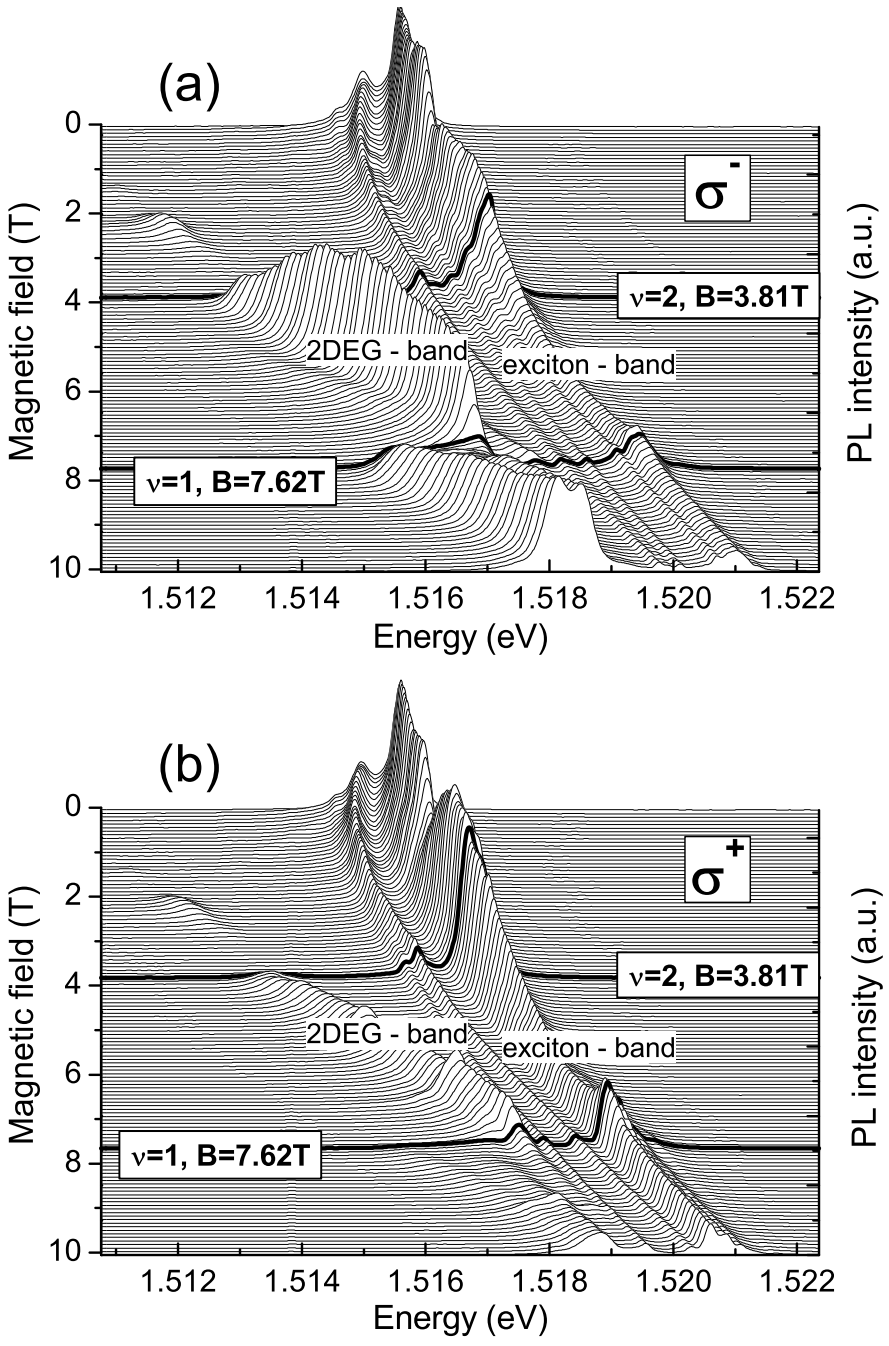


Figure 6.1: Magneto PL of the GaAs/AlGaAs HJ in (a) $\sigma^-$ polarization and (b) $\sigma^+$ polarization. $n_e = 1.84 \cdot 10^{11} cm^{-2}$, $P_{785nm} = 0.30\ mW/cm^2$ and $T = 2.2\ K$.

## 6.2 Experimental data

The magneto-PL of the GaAs/AlGaAs HJ (see Sec. 5) is displayed in Fig. 6.1 for $\sigma^-$- (a) and $\sigma^+$-polarization (b). The spectra were obtained under low intensity below barrier excitation (0.25 $mW/cm^2$) and low temperatures of $T = 2.2\ K$. Separately integrated PL intensities of the X-band and the 2DEG-band are plotted against the magnetic field in Fig. 6.2. The PL shows a complex magnetic field dependence. It is characterized by abrupt changes in peak energy and intensity on the one hand, and regions of smooth PL evolution on the other hand. The abrupt discontinuities turn out to coincide very well with integer filling factors [4] and can be used as an optical measure of the electron density according to Eq. 2.28. Over the whole field range there is an intensity interplay between the two bands: If one band looses intensity, the other band gains intensity and vice versa, while the total intensity varies only weakly. Three characteristic intervals of magnetic field can be specified:

**$B < 3.81\ T$, $\nu > 2$**

In low magnetic fields, only the X-band PL is visible at $E = 1.5155\ eV$. At $B = 2.25\ T$ however, a small contribution of the 2DEG-band appears for a narrow field range of 0.4 $T$, while at the same time the X-band looses intensity. In the range $2.25\ T < B < 3.81\ T$, again only PL from the X-band is visible. Already at these small fields the different polarization of 2DEG-band and X-band is noticeable: The 2DEG-band shows stronger intensity in the $\sigma^-$-polarization, while the X-band is more pronounced in $\sigma^+$-polarization.

**$3.81\ T < B < 7.62\ T$, $1 < \nu < 2$**

The 2DEG-band strongly gains intensity, while the X-band looses intensity at the same time. For fields larger than 5 $T$ the X-band intensity even exceeds that from the 2DEG-band. Meanwhile the X-band is split by the magnetic field and a rich spectrum of several lines in each polarization appears.

**$B > 7.62\ T$, $\nu < 1$**

X-band and 2DEG-band show a sharp discontinuity within a narrow field range of 0.5 $T$ around $\nu = 1$: The X-band intensity increases and the 2DEG-band intensity decreases in turn. For $\nu < 1$ the X-band continuously shifts to higher energies and remains slightly $\sigma^+$-polarized. The 2DEG-band, however, shows a more com-

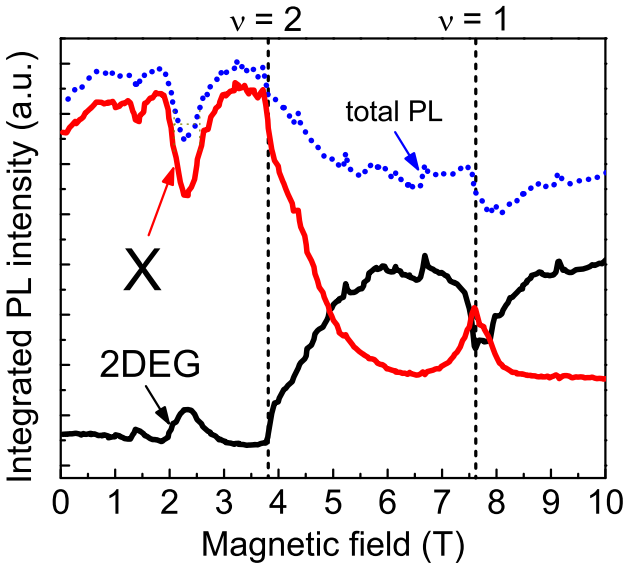


Figure 6.2: Integrated intensity of the unpolarized PL in dependence of the magnetic field. X (black line), 2DEG (red line) and the total PL intensity (blue dots). The magnetic fields, corresponding to filling factors $\nu = 1$ and $\nu = 2$ are shown by dashed auxiliary lines.

plex behaviour, including pronounced differences for $\sigma^+$- and $\sigma^-$-polarizations. In $\sigma^+$-polarization the 2DEG-band intensity is strongly reduced, while in $\sigma^-$-polarization there is strong 2DEG-band PL, which is abruptly shifted in energy by $\Delta E = 2\ meV$ at $\nu = 1$.

At first, X-band and 2DEG-band are discussed separately in sections 6.3 and 6.4, followed by the PL intensity interplay of the two bands in Sec. 6.5.

## 6.3 The exciton-band

In Fig. 6.3 the zero field PL is presented at 2.2 $K$ for a low excitation density of $0.30 mW/cm^2$ by 1.579 $eV$ below band-gap illumination only. The spectrum consists of two lines at 1.5155 $eV$ and 1.5149 $eV$. Both lines were assigned to exciton recombinations in the past and called the X-band in a nutshell. Transitions of the 2DEG are barely visible.

The stronger exciton peak at 1.5155 $eV$ coincides well with free 3D-excitons in bulk GaAs [6], which suggests the PL origin in the wide GaAs layer. This assumption is confirmed by etching off the GaAs/AlGaAs heterojunction from MBE grown samples, as the strong X-band PL does not

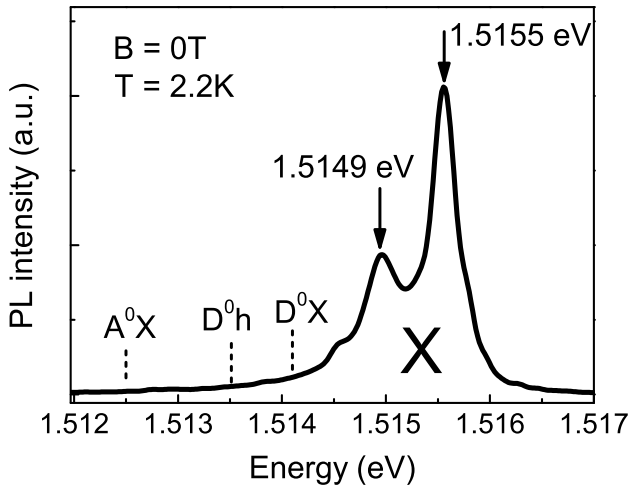


Figure 6.3: PL spectrum of the GaAs/AlGaAs heterojunction at $B = 0\ T$. $n_e = 1.84 \cdot 10^{11} cm^{-2}$, $P_{785nm} = 0.30\ mW/cm^2$ and $T = 2.2\ K$

change with removing the AlGaAs barrier layer [27]. Thus, the line is commonly called the *free exciton* line.

The weaker X-band line at 1.149 $eV$ does not appear in bulk GaAs. Its relative intensity, compared to the free exciton line, depends strongly on excitation conditions and the specific sample and might appear as a weak shoulder only.

The line is only rarely discussed in literature. In [30], a similar feature is assigned to so called *interface excitons*, which are trapped close to the interface in a "shallow potential minimum for the translational exciton motion" [28]. In later papers the interface excitons are not mentioned any more. Instead a "repulsive barrier"is described [7], which should cause the same shallow traps close to the interface.

The X-band lines in Fig. 6.3 show only weak inhomogeneous broadening of less than 0.4 $meV$ FWHM, which reflects high sample quality. Furthermore, no traces of impurity states on the low field shoulder of the X-band are visible. The three closest impurity states, an exciton bound to a neutral donor ($D^0X$), a free hole to neutral donor recombination ($D^0h$) and a neutral acceptor bound exciton ($A^0X$), are marked at their expected energy positions [27]. For none of them evidence is found in the $B = 0\ T$ PL.

With increasing magnetic field, the exciton line splits into several lines in both polarizations (see. Fig. 6.1). This splitting is attributed to a mixing of exciton states with total spin $S_X = 1$ and $S_X = 2$ [7, 31]. It arises from the bulk character of the thick GaAs layer: In bulk GaAs at $k = 0$ the heavy- and light hole states are degenerate, so that the exciton eigenstates $|X\rangle$ are

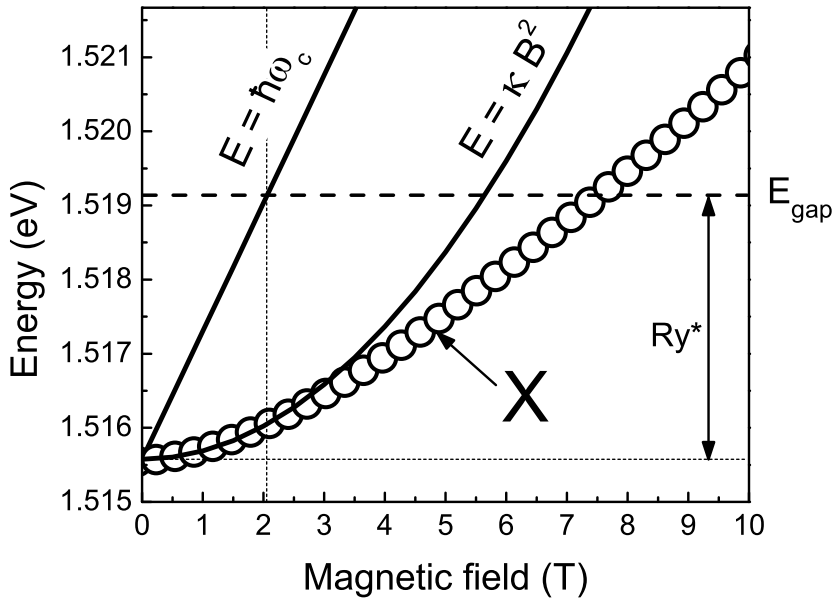


Figure 6.4: Measured exciton diamagnetic shift (open symbols). As a solid line the exciton diamagnetic shift is plotted according to Eq. 3.20 and assuming $m_e^* = 0.067\ m_0$, $m_h^* = 0.53\ m_0$, $a_b = 12.3\ nm$. Auxiliary lines illustrate the magnetic energy $E = \hbar\omega_c$ and the bulk GaAs band-gap energy $E_{gap}$.

a superposition of heavy- and light hole excitons ($|X_{hh}\rangle$, $|X_{lh}\rangle$),

$$|X\rangle = A\ |X_{hh}\rangle + B\ |X_{lh}\rangle\,, \tag{6.1}$$

with complex constants $A$ and $B$. A magnetic field in Faraday configuration mixes the $S_X = 1$ and $S_X = 2$ states, assigning a finite oscillator strength to otherwise dark states. If the X-band PL was not due to 3D-exciton recombination but would arise from close to the interface, the confinement potential would split off the light hole states and no mixing of the $S_X = 1$ and $S_X = 2$ states would be possible. Thus, the rich exciton spectrum might verify the bulk-like character of the X-band PL additionally.

Furthermore, the X-band diamagnetic shift confirms the bulk exciton hypothesis. As pointed out in section 3.3, one expects a free 3D-exciton diamagnetic shift according to equation Eq. 3.20 for magnetic energies $\hbar\omega_c$ smaller than $Ry^*$. Considering typical GaAs values for the Bohr radius $a_b = 12.3\ nm$ and the effective carrier masses $m_e^* = 0.067\ m_0$, $m_h^* = 0.53\ m_0$, one finds the diamagnetic shift plotted in Fig. 6.4 as a solid curve. The open symbols in Fig. 6.4 correspond to the measured diamagnetic shift of the strongest X line. The Zeeman shift is removed by calculating the mean energy value of $\sigma^+$- and $\sigma^-$-polarization PL lines. The calculated diamagnetic

shift corresponds well to the experimentally obtained shift up to $B = 2.06\ T$, where $\hbar\omega_C = Ry^*$. At higher fields, an increasing deviation appears, as expected due to the low field approximation introduced in section 3.3.

## 6.4 The 2DEG-band

Since its discovery, there was no doubt about the origin of the 2DEG-band: Quasi two-dimensional electrons, confined in the heterojunction's potential notch, recombine with 3D-holes from the GaAs layer.

The simplest reasonable approximation for the confinement potential is a triangular potential well (see Fig. 6.5)

$$\begin{aligned} V(z) &= eF(z - z_0) && z \geq z_0 \\ V(z) &= \infty && z < z_0, \end{aligned} \tag{6.2}$$

where the interface is expected at $z = z_0$ and the electric field $F$ is generated by the charge of the 2DEG

$$F = \frac{e\ n_e}{\epsilon}. \tag{6.3}$$

The ground state of such a potential can be expected to be in acceptable agreement with the real heterojunction [32].

The electrons' Schrödinger equation with eigenenergies $E_{tri}$

$$\left(\frac{p_z^2}{2m^*} + V(z)\right)\Psi(z) = E^{tri}\Psi(z) \tag{6.4}$$

is solved by Airy-functions

$$\Psi_n(z) = Ai_n\left(\frac{eFz - E_n^{tri}}{E_0^{tri}}\right), \tag{6.5}$$

where

$$E_0^{tri} = \left[\frac{(eF\hbar)^2}{2m^*}\right]^{1/3}. \tag{6.6}$$

The eigenenergies are

$$E_n^{tri} = c_n\ E_0^{tri}. \tag{6.7}$$

The $c_n$ have to be calculated numerically. In [32] $c_1 = 2.338$ is specified for the groundstate, which results in a confinement energy of $E_1^{tri} = 36.7\ meV$.

Due to Kohn's theorem, the Landau level spacing is not influenced by electron-electron interaction. However, the absolute energy of the 2DEG-band is shifted by carrier interactions, commonly called the *band-gap renormalization* (BGR). BGR leads to an electron-density dependent reduction of the PL energy.

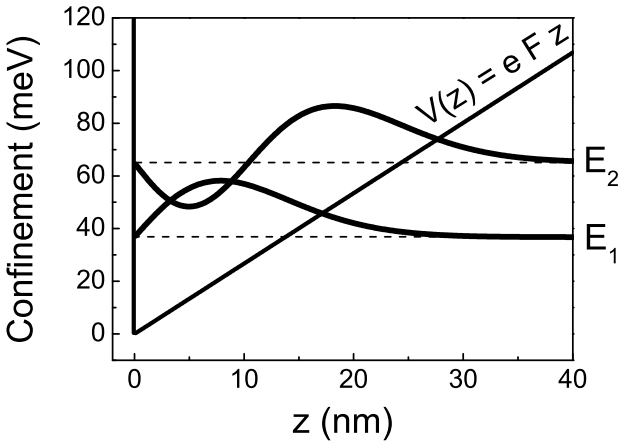


Figure 6.5: A triangular potential well according to Eq. 6.2, plotted for $n_e = 1.84 \cdot 10^{11} cm^{-2}$. Two energy levels $E_1^{tri} = 36.7\ meV$ and $E_2^{tri} = 65.12\ meV$ are depicted as dashed lines. As solid lines, the corresponding two eigenstates $\Psi_1$ and $\Psi_2$ are given according to Eq. 6.5.

BGR effects appear in Fig. 6.6. While the X-band is pinned at $E = 1.5155\ eV$, irrespective of the electron density, the 2DEG-band shifts to higher energies with decreasing electron density. Zero field extrapolations (dashed lines in Fig. 6.6) show the 2DEG-energy shifting from 1.5094 $eV$ at $n_e = 1.84 \cdot 10^{11} cm^{-2}$ to 1.5119 $eV$ at $n_e = 7.15 \cdot 10^{10} cm^{-2}$. Similar extrapolations for other electron densities provide a 2DEG-energy versus 2DEG-density dataset, which can be interpolated by the approximative formula

$$E_{\mathrm{BGR}}\,[meV] = C\ n_e\left[cm^{-2}\right]^{0.32}. \tag{6.8}$$

It describes BGR in GaAs at high electron densities [33]. A fit provides $C = 2.4{\cdot}10^{-3}$, being very close to $C = 2.2{\cdot}10^{-3}$, estimated for GaAs quantum wells [33]. Substituting $C = 2.4{\cdot}10^{-3}$ into Eq. 6.8, a BGR of $E_{\mathrm{BGR}} = 9.6\ meV$ is obtained for the native 2DEG density $n_e = 1.84 \cdot 10^{11} cm^{-2}$.

For all investigated electron densities, the 2DEG band is situated on the low energy side of the X-band (see Fig. 6.6). It shows a linear magnetic field dependence, typical for large electron densities. For parabolic bands, one would expect the carriers to occupy Landau levels, shifting linearly with magnetic field. The slope should correspond to the free carrier effective masses. Thus, the 2DEG-band PL signal should obey

$$E = 1.5097\ eV + 1/2\ \hbar e\left(\frac{1}{m_e^*} + \frac{1}{m_h^*}\right). \tag{6.9}$$

Basically Eq. 6.9 reproduces the experimental data quite well, as demonstrated in Fig. 6.7: The measured 2DEG-band energy positions for $n_e =$

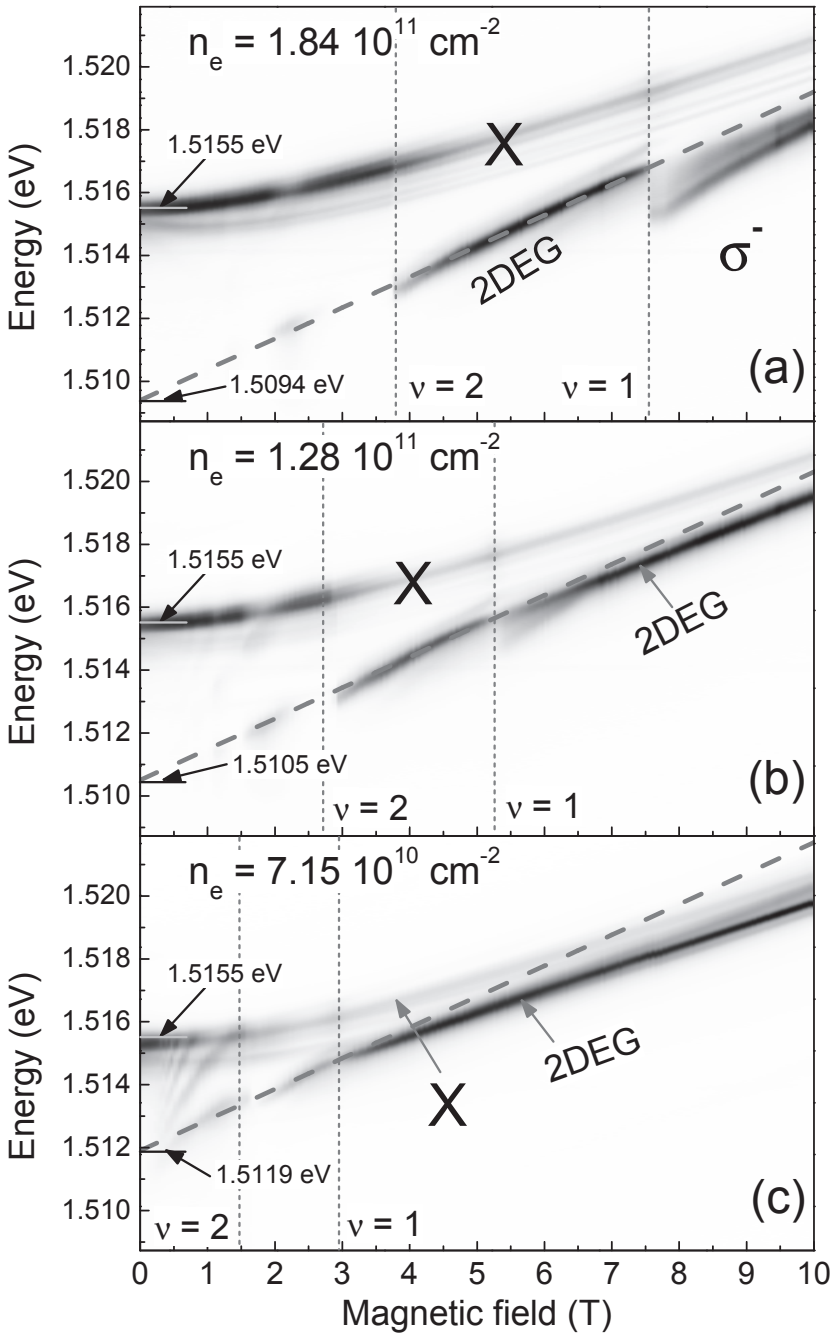


Figure 6.6: Contour plots of the magneto PL for three different electron densities, $n_e = 1.84 \cdot 10^{11} cm^{-2}$ (a), $n_e = 1.28 \cdot 10^{11} cm^{-2}$ (b) and $n_e = 7.15 \cdot 10^{10} cm^{-2}$ (c). The dashed lines are given by the sum of the lowest electron and hole Landau levels with $m_e^* = 0.067\ m_0$ and $m_h^* = 0.53\ m_0$ and a constant offset of 1.5094 $eV$ (a), 1.5105 $eV$ (b) and 1.5119 $eV$ (c). $T = 2.2K$.

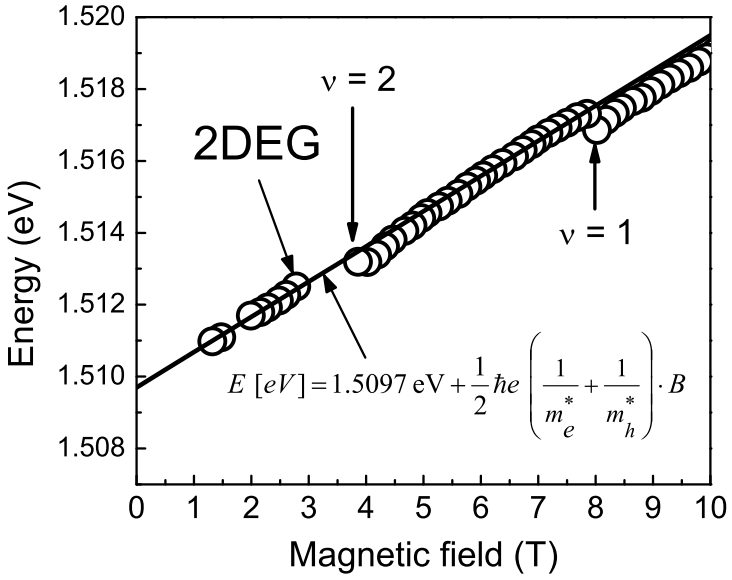


Figure 6.7: 2DEG peak energies (open symbols) without Zeeman splitting contribution. The solid line is the sum of the lowest electron and hole Landau level, shifted by 1.5097 $eV$. $m_e^* = 0.067\ m_0$ and $m_h^* = 0.53\ m_0$.

1.84 $10^{11} cm^{-2}$ are presented as open symbols. The Zeeman-splitting is removed by calculating the mean energy value of $\sigma^+$- and $\sigma^-$-polarizations. The energy according to Eq. 6.9 is drawn as a solid line.

For wide ranges of magnetic fields, there is reasonable agreement of the data and the calculated line. Major deviations are visible around $\nu = 2$ and for filling factors $\nu < 1$. These deviations are attributed to integer filling factor effects due to electron-electron interactions (see Sec. 6.5.2), which are not included in the simple model at hand.

The constant offset of 1.5094 $eV$ in Eq. 6.9 is needed to fit the absolute energy position of the 2DEG band. It is composed of several contributions of different physical origin. However, besides the plain GaAs band-gap, none of these contributions can be seriously quantified without careful theoretical treatment. Nevertheless, the following approximative values are illustrative and give at least the correct order of magnitude:

- The largest contribution is obviously given by the GaAs band-gap energy $E_{gap} = 1.5191\ eV$.

- The confinement potential of the heterojunction, approximated as a triangular well, contributes additional 36.7 $meV$, given by the ground state confinement energy $E_1^{tri}$ (Eq. 6.7).

- According to Eq. 6.8, BGR leads to a shift of $E_{\mathrm{BGR}} = 9.6\ meV$ to lower energies, for $n_e = 1.84 \cdot 10^{11} cm^{-2}$.

- The remaining energy shift is probably caused by the electric field induced displacement of the 2DEG and the 3D GaAs holes, leading to a reduction of the PL energy. As there is considerable band bending near the interface, the hole energy increases with increasing distance from the heterojunction (Fig. 5.2). As the electrons are confined close to the interface, an increasing electron hole displacement reduces the observed recombination energy effectively. The electric field, induced at $n_e = 1.84\ 10^{11} cm^{-2}$, is quite large at the interface $F = 26.7\ kV/cm$ but is weakened considerably with increasing distance from the heterojunction. The situation is further complicated by the fact, that the exciton dissociation mechanism (see. Sec. 6.5) is not theoretically discussed yet. Thus no numbers for the displacement of the holes, recombining with the 2DEG, are known. However, experiments on GaAs QWs reveal displacement energies of 30 - 40 $meV$ [34], suggesting the correct order of magnitude to explain the 2DEG PL-position.

## 6.5 Exciton dissociation

As shown in Sec. 6.2, the X-band and the 2DEG-band coexist in the PL and interact strongly with each other at certain magnetic fields. The most recent attempt for an explanation is based on an initial generation of bulk excitons, which drift to the GaAs/AlGaAs interface and dissociate there into a 2D electron and a 3D-hole, supplying the holes for 2DEG-hole recombination [7]. This model is able to explain the strong PL intensity exchange between the two bands. The PL anomalies at $\nu = 1$ and at $\nu = 2$ are interpreted as follows:

### 6.5.1 Filling factor $\nu$=2

The zero field 2D Fermi energy

$$E_F^0 = \frac{n_e \pi \hbar^2}{m^*}, \tag{6.10}$$

follows the energy of the lowest filled Landau level, as shown in Fig. 6.8. At integer filling factors $E_F$, singularities are observed [32]. At $\nu = 2$ the most pronounced drop of $E_F$ occurs. For filling factors $\nu > 2$ the Fermi energy is so large, that mainly no exciton dissociation is possible. At $\nu = 2$, however,

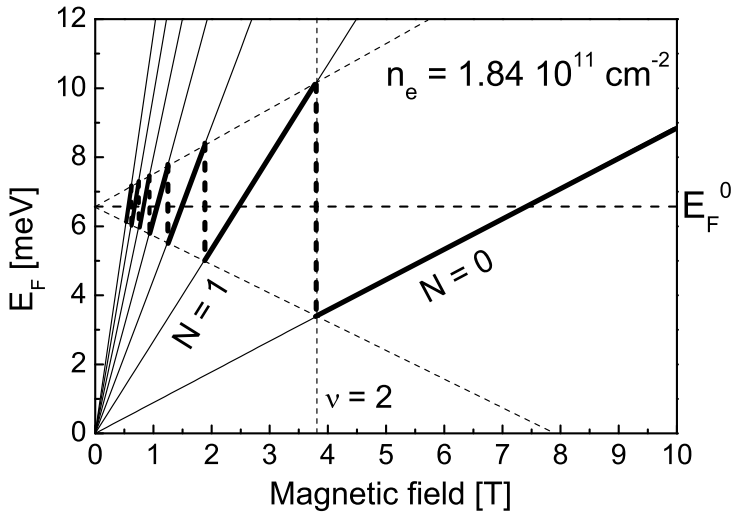


Figure 6.8: Magnetic field dependence of the Fermi energy (thick lines) for an electron density of $n_e = 1.84 \cdot 10^{11} cm^{-2}$ and a zero magnetic field Fermi energy $E_F^0 = 6.6\ meV$. The thin lines represent the low energy Landau levels. The Figure is plotted in analogy to Ref. [32].

the 2DEG-hole recombination energy drops below the X-band energy. Thus exciton dissociation becomes more favorable and the 2DEG-band suddenly appears in PL [7].

### 6.5.2 Filling factor $\nu$=1

At $\nu = 1$ there are two effects that should be discussed separately. At first, the exciton PL intensity increases resonantly at $\nu = 1$, while its intensity is on about the same level in the vicinity of the resonance for $\nu < 1$ and $\nu > 1$. Second the 2DEG-band PL experiences a shift in energy and redistributions of PL-intensity between its two polarizations.

The X-band intensity change is commonly attributed to the *incompressibility* of the 2DEG at $\nu = 1$. In such a state, scattering is strongly suppressed, compared to a partially filled spin level, where the electrons can scatter into unoccupied states. In the incompressible state, the 2D-electron 3D-hole wavefunction overlap is reduced due to suppressed electron scattering [4]. This in turn decreases the electron-hole interaction energy and eventually restrains the excitons from dissociating into the 2DEG [7].

The 2DEG-band modification is explained by different electron-hole interaction for $\nu < 1$ and $\nu > 1$ [7, 34]. At sufficiently large electron hole separation, where the electron-hole binding energy is small, there is a tran-

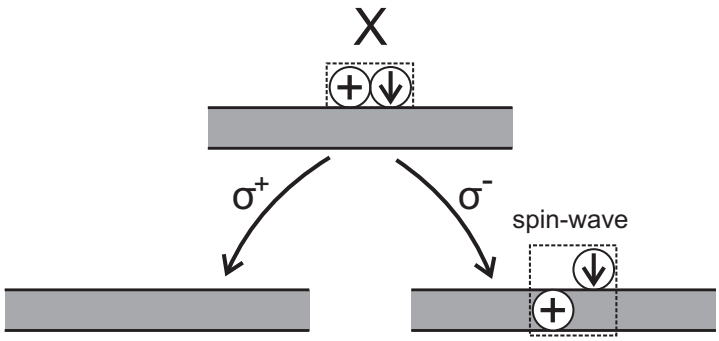


Figure 6.9: Optical transitions of *excitonic states*. The gray bars represent a completely filled lowest spin level of spin-↑ electrons and a single spin-↓ electron is represented by an open circle, filled with ↓. A valence band hole is drawn by an open circle, filled with "+", a *spin hole* is given by the same symbol, printed in the bar of the filled spin level. The figure is plotted in analogy to [35].

sition in the ground state from so called *excitonic* to *non-excitonic* states at $\nu = 1$.

The terminology of excitonic- and non-excitonic 2DEG-states was developed by Cooper and Chklovskii [35]. The authors consider a 2DEG, very close to filling factor $\nu = 1$, with a Zeeman splitting energy $Z$. The valence band holes interact differently with the few spin down electrons in the higher spin level, compared to the many spin down electrons in the strongly populated lowest spin level: A significant Coulomb interaction is only expected for the spin down electrons of the upper spin level. A state with such a bound complex is named excitonic, labelled as $X$ in Fig. 6.9. For spin up electrons such an excitonic state is not considered, probably due to the incompressibility of the completely filled spin level. For large excitonic binding energies $E_X$, the excitonic states might be the ground state of the system. This holds even for $\nu < 1$, where it is energetically favorable for the electrons to flip their spin (requiring the energy $Z + E_{\mathrm{SW}}$) into the higher spin state and form an exciton with a valence band hole (gaining the energy $E_X$). Here, $E_{\mathrm{SW}}$ is the energy of a spin-wave, which is induced by the electron spin flip [36]. For small $E_X$ however, the non-excitonic state might be the ground state.

$E_X$ can be controlled by the electron-hole displacement, e.g. by the strength of a static electric field, as done in Ref. [34] in quantum wells. For strong displacements an excitonic ground state is found for $\nu > 1$ and a non-excitonic for $\nu < 1$. This transition of the ground state is identified by similar 2DEG-PL anomalies, observed in the PL of the HJ investigated here

(see Fig. 6.1):

Firstly, the $\sigma^-$-polarized PL exhibits a red shift in energy at $\nu = 1$ for increasing magnetic field. It corresponds to $\Delta E = E_{\mathrm{SW}} - E_X$, as with increasing field, the initial state looses the exciton binding energy and in the final state, there is no spin wave excitation any more (compare Fig. 6.9).

Secondly, the $\sigma^+$-polarized PL is strongly reduced at $\nu = 1$, as there is no significant spin down electron population for $\nu < 1$, when $E_X$ is too small to have a ground state of excitonic nature. Consequently the spin polarization favors $\sigma^-$ polarized recombinations and the $\sigma^-$ PL gains additional intensity (compare Fig. 6.9).

## 6.6 Summary

The exciton dissociation mechanism turns out to be a suitable model to explain the GaAs/AlGaAs HJs PL. The interpretation of simultaneous observation of 3D-excitons and 2DEG to 3D-hole recombinations could be confirmed by the X-band energy position, the diamagnetic shift and linear field dependence of the respective PL features, as well as by the electron density dependence. The intensity interplay of the main PL bands is an expression of the exciton dissociation and subsequent supply of free holes for 2DEG-hole recombinations. However, profound theoretical treatment is essential to verify the exciton dissociation and the related PL discontinuities beyond any doubt.

# 7

# Far-infrared modulated photoluminescence

A wide variety of semiconductor intraband excitations can be addressed by FIR-radiation. For instance, it can induce transitions between Landau levels, between quantum confinement subbands or between excitonic states. Although the FIR spectral range is technically challenging, FIR experiments developed into an established field of semiconductor research.

Especially cyclotron resonance was widely studied in the past. After initial attempts in the 1950s, FIR transmission measurements have been started in 1961 to investigate electron cyclotron resonance in GaAs [37]. Mainly electronic band parameters, electron-electron interaction and polaron effects were investigated, using either FIR-Lasers with a discrete spectrum of narrow lines or alternatively Fourier-transform-spectrometers with tunable FIR-sources. Some drawbacks of the problematic FIR-technique have been partly overcome by using detection techniques in the more convenient visible spectral range. PL modifications were used as a detector for resonant FIR absorption - the idea of optically detected resonance (ODR) was born. In general, the term ODR includes more than just CR detection and is used for any kind of FIR induced resonance. In the specific case of CR, the technique is is commonly called *optically detected cyclotron resonance* (ODCR)). The ODCR technique provides advantages compared to conventional FIR transmission experiments:

In the early days of ODCR optical excitation was important to neutralize impurities by photogenerated carriers and thus increase the electron scattering times $\tau$. Especially at low frequencies in the microwave range and for bulk samples of limited purity, the required CR condition $\omega_c\tau \geq 1$ was not necessarily fulfilled and the optical excitation could have been decisive for successful CR. Higher cyclotron frequencies, such as in the case of FIR radiation, further contribute to large values of $\omega_c\tau$ and enable measurements at higher magnetic fields, providing more precise effective mass values [38]. Today,

using high quality nanostructures, the scattering is a less important issue. However, not only scattering is reduced by photoexcited carriers. Furthermore photoexcited carriers enable CR studies in structures, which naturally do not supply sufficient resident carriers to provide acceptable FIR absorption. Together with highly sensitive optical detectors, CR can be measured even in undoped quantum wells [3].

The most promising feature of ODR in general, is directly related to the optical detection technique. ODR opens up possibilities to investigate PL lines separately on their specific FIR response and thus there is principally extended insight into the resonance mechanism. Especially the combination of FIR-ODR and GaAs/AlGaAs HJs is very promising, as at the magnetic field of electron-CR both main PL lines are visible. Microwave-ODCR studies on similar samples can detect PL modulations of the exciton band only [6] - the influence on the 2DEG-band remains hidden.

However, quite often the exact physical ODCR mechanism could not be deduced from the PL modifications unambiguously and remains only superficially discussed.

First ODR studies were performed with microwave radiation instead of FIR. Initially ODCR in Ge-crystals was investigated in 1977 [39] and in 1980 for the first time in GaAs [40]. Another decade passed until in 1990 the first FIR-ODCR was performed in bulk GaAs [1]. Since that several FIR ODR studies have been published, treating mainly four different FIR absorption mechanisms:

(1) Impurity transitions [2, 41, 42].

(2) Internal exciton and trion transitions [43, 44, 45, 46, 47, 48].

(3) Transitions between quantum dot states [49, 50].

(4) Free electron CR in different material systems, like bulk GaAs [51, 41], GaAs quantum wells [52, 53, 54, 55, 2], GaInAs quantum wells [56], CdTe quantum wells [57, 3] and GaAs HJs [8, 9, 10, 11].

While the discussion of FIR ODCR in GaAs/AlGaAs HJs took place from 1992 to 1999, the most recent PL interpretation was outlined in 2000 [6] and extensively formulated in reference [7], one year after the last FIR ODCR study of GaAs/AlGaAs HJs was published. As the picture of the physical origin of the HJ PL changed quite considerably with that, there is the need for another review of the FIR-ODR mechanism as well, which is still missing in literature.

In this chapter FIR-ODR measurements on GaAs/AlGaAs HJs are presented and the interpretations follows the most recent suggestions for the HJ PL mechanism. In Sec. 7.1.1 an ODCR model, based on nonequilibrium phonons, is suggested. Time resolved FIR ODR experiments (Sec. 7.1.4) and temperature dependent PL measurements (Sec. 7.1.3) indicate that simple lattice heating can be excluded to cause the PL modulation.

Beyond the basic question about the ODR mechanism, the potential of ODCR experiments on GaAs/AlGaAs HJs is not fully used so far. As pointed out in Sec. 5, GaAs/AlGaAs HJs supply very high electron mobilities, due to minimal perturbation effects. Together with very low FIR laser excitation densities, especially narrow ODCR resonances are measured and presented in this thesis. Taking into account FIR reflections at the 2DEG interface, a basic Drude model allows to estimate realistic electron mobility values and provides a suitable description of the electron-density dependence of the ODCR linewidth.

Furthermore the narrow ODCR-lines allow to resolve nonparabolicity effects (Sec. 7.2.1) and CR satellite resonances (Sec. 7.2.4). Thanks to the large electron densities, ODCR can be compared with conventional FIR transmission and thus it is possible to isolate the origin of the additional resonances.

## 7.1 The native electron density

Naturally, it is desirable to avert unwanted external perturbations to investigate the intrinsic properties of the sample. Especially the excitation conditions offer many possibilities to modify the systems equilibrium state. The generation of photoexcited carriers is essential to measure PL, however it is accompanied by changes in the electron density and carrier heating effects, which are not necessarily desirable. Weak below barrier illumination of $P_{ex} = 0.33\ mW/cm^2$ reduces density variations and heating effects to a minimum and the samples native electron density is barely influenced. ODCR experiments under these conditions are most likely a promising starting point to investigate the ODR mechanism.

An example of PL modulation by FIR radiation is presented in Fig. 7.1. Three spectra are shown, the pure PL (black), the PL under FIR radiation (blue) and the modulation spectrum (red). With FIR illumination the 2DEG-band PL amplitude is reduced by 16%, while the X-band intensity increases by about the same fraction. The spectra are shown for $B_{res} = 6.135\ T$, which is the magnetic field of the strongest FIR modulation. Fig. 7.2 (a) shows the PL modulation spectra in a small magnetic field range around this resonance field. The shape of the modulation is similar

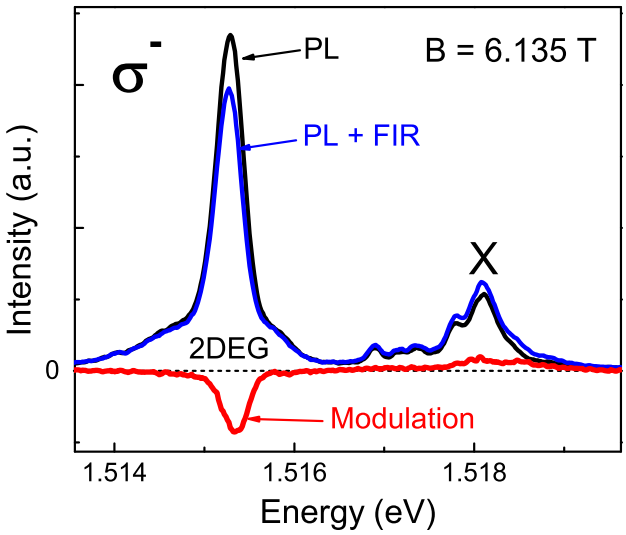


Figure 7.1: PL (black), PL+FIR (blue) and modulation (red) spectra for the native electron density $n_e = 1.84 \cdot 10^{11} cm^{-2}$ and a low FIR excitation density of $P_{\mathrm{FIR}} = 1.8\ mW/cm^2$. $T = 2.2\ K$, $P_{785nm} = 0.30\ mW/cm^2$ and $E_{\mathrm{FIR}} = 10.433\ meV$.

for all fields, while the modulation amplitude drops rapidly, with increasing distance from $B_{res}$. Best visibility of this drop in the modulation intensity is provided by panel (b) of Fig. 7.2, where the correspondig ODR-signal (see Eq. 4.2) is plotted for the same magnetic field scale as panel (a).

### 7.1.1 The ODR mechanism

The mechanism behind the PL modulation under FIR radiation can be understood as a two-step process - the FIR radiation is resonantly absorbed by 2DEG-CR and subsequently the hot electrons modify the PL:

#### FIR absorption by electron-CR

FIR absorption by a 2DEG in GaAs/AlGaAs HJs has been extensively studied in the past by FIR transmission experiments [58, 59] and could be assigned to electron-CR without a doubt. In the experiments presented here, the same FIR absorption by electron-CR could be expected. In fact, the ODR signal in Fig. 7.2 (b) shows a similar resonance behaviour, as the typical FIR absorption measurements (see Fig. 7.19). Entering its resonance center position $B_{res}$ in Eq. 2.66 reveals a carrier mass of 0.068 $m_0$, very close to the free effective electron mass in GaAs (0.067 $m_0$). Apparently the ODR

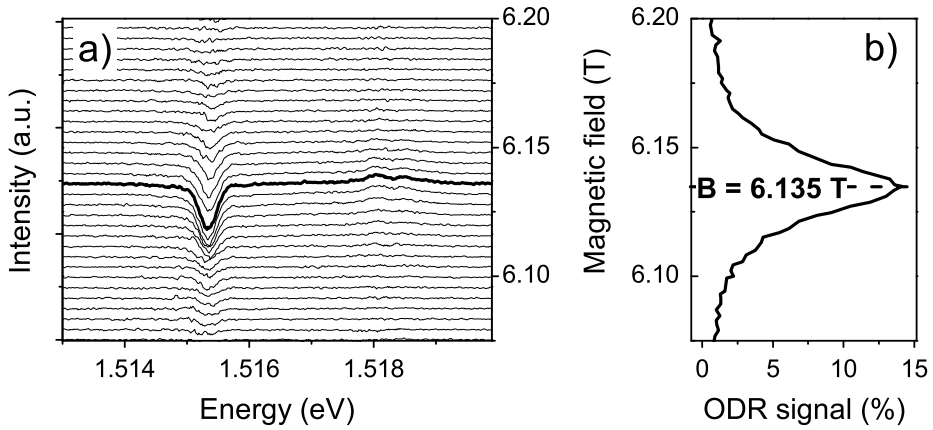


Figure 7.2: Waterfall plot (a) of the modulation spectra in the vicinity of the CR magnetic field $B = 6.135\ T$ and the ODR signal according to Eq. 4.2 (b). $T = 2.2\ K$, $n_e = 1.84 \cdot 10^{11} cm^{-2}$, $P_{\mathrm{FIR}} = 1.8\ mW/cm^2$, $P_{785nm} = 0.30\ mW/cm^2$ and $E_{\mathrm{FIR}} = 10.433\ meV$.

is based on the resonant absorption of FIR radiation, causing a so called *resonant heating* of the electrons.

### PL modulation by hot electrons

Some proposals for PL modulation mechanisms by hot electrons can be found in literature. Most of them require direct contact of the electron gas and the optically active electron hole pairs, e.g. impact ionization [56] or the modification of trion formation probabilities by hot electrons [57]. Typically a direct contact is given in common quantum well structures, where both, the electron gas and the optically active electron hole pairs are situated in the quantum well, having a significant wavefunction overlap. Similar assumptions were made for GaAs/AlGaAs HJs [8, 9, 10]: The authors assume all main PL-features to arise from the potential notch at the interface, where the 2DEG is situated, too. At CR the electrons might gain sufficient energy to reach the long living second HJ subband and increase its electron population consequently. This in turn favors optical recombinations with second subband electrons and reduces first subband transitions in the PL. As a result, a PL intensity redistribution is induced by CR.

While this explanation is suitable for Be-doped structures, as presented in [9], a contradiction appears together with recent HJ PL interpretations for the Be-free HJs, studied here and in [8, 10]. The latest HJ PL interpretations propose, that the 2DEG and the X-band PL arise from different regions in

the sample (see Sec. 6.2), so that any kind of direct interaction is rather unlikely. While the 2DEG is directly influenced by the FIR radiation, the FIR modulation of the X-band PL requires a model which does not involve direct electron-exciton scattering, but provides a long-ranging interaction mechanism. Such an interaction might be mediated by phonons, as discussed in the following section.

### 7.1.2 Phonon-assisted 2DEG - X interaction

It is known, that a hot 2DEG largely dissipates its excess energy by acoustic phonon emission [60, 6]. Acoustic phonons of sufficiently low energy are able to travel long distances without scattering, easily exceeding the 1 $\mu m$ wide GaAs layer and thus providing a possible long-ranging interaction channel beyond plain overall lattice heating. Those non-scattering phonons are said to travel *ballistically* and are commonly called *nonequilibrium* phonons, as their energy is larger than that of the phonons at equilibrium lattice temperature.

For microwave-CR it was already estimated, that the emitted phonons fulfill all requirements for ballistic propagation [6]. For FIR-CR a short evaluation provides clarity: Assuming mainly CR transitions from the first to the second Landau level, the energy of the emitted phonons should barely exceed the FIR photon energy $E_{\mathrm{FIR}} = 10.433\ meV$. Phonons with $E_{phonon} = 10.433\ meV$ decay within 1.3 $ns$ [61], sufficient time to travel 6.7 $\mu m$ in GaAs [1]. All phonons with lower energy have an even larger mean free path, as their decay time increases with decreasing phonon energy [61]. Thus one could expect the resonantly heated 2DEG to emit nonequilibrium phonons, traveling ballistically through the whole GaAs layer.

Such a flux of phonons, arising from the hot 2DEG in the potential notch is known as a *phonon wind* [62]. It is able to transfer momentum and energy to the free excitons in the GaAs layer. That way the excitons are heated and experience a force, known as *exciton drag* [6, 62, 63, 64, 65], pushing them away from the HJ. However, it is not immediately clear, how many nonequilibirium phonons scatter with the excitons and how many of them travel on unperturbed, out of the GaAs layer and finally contribute to an increase of the overall lattice temperature. Thus, it cannot be excluded, that the PL modulation is mainly caused by an equilibrium lattice heating rather than by a phonon wind.

[1] Typical sound velocity in GaAs is $5 \cdot 10^3\ m/s$.

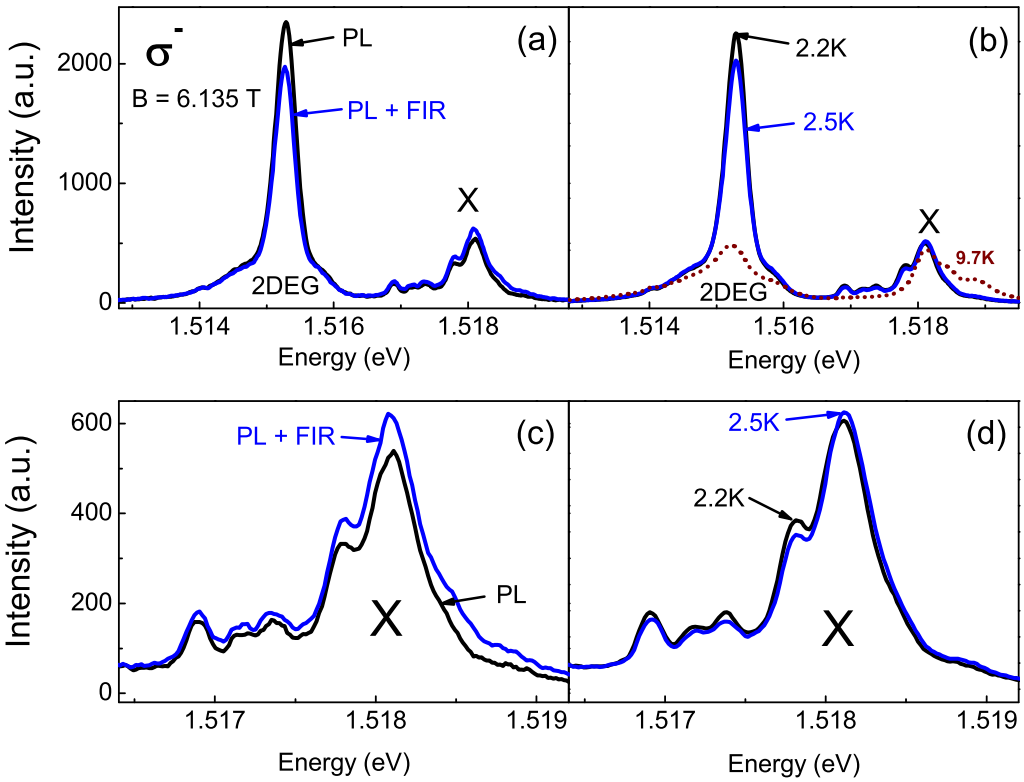


Figure 7.3: PL modulation by FIR radiation in comparison to temperature induced PL variations at $n_e = 1.84 \cdot 10^{11} cm^{-2}$. (a) Pure PL at $T = 2.2\ K$ and PL with FIR radiation ($P_{\mathrm{FIR}} = 1.8\ mW/cm^2$ and $E_{\mathrm{FIR}} = 10.433\ meV$). (b) PL at $T = 2.2\ K$, $T = 2.5\ K$ and $T = 9.7\ K$ respectively. Panels (c) and (d) show closeups of the X-band under FIR irradiation and temperature changes, respectively. $P_{785nm} = 0.30\ mW/cm^2$.

### 7.1.3 FIR induced 2DEG heating

To clarify, if simple lattice heating, or a phonon wind dominates the ODR mechanism, a comparison of the PL temperature dependence and the PL modulation by FIR radiation is helpful. The PL temperature dependence provides a reference of pure lattice heating. If the FIR PL modulation is based on an overall temperature increase, the FIR PL modulation should coincide with the PL modulation induced by slight temperature changes.

In Fig. 7.3 (a) the pure PL and PL with additional low power FIR irradiation are shown at $B = B_{res}$. The 2DEG-band PL intensity decreases under the influence of FIR, while the X-band PL intensity slightly increases at the same time. Fig. 7.3 (b) demonstrates the influence of a slight tem-

perature increase from $T = 2.2\ K$ to $T = 2.5\ K$ at the same magnetic field $B_{res} = 6.135\ T$, as in panel (a). Naturally, the pure 2.2 $K$-PL of both panels (a) and (b) coincide exactly.

The FIR modulated PL of panel (a) and the PL at 2.5 $K$ of panel (b) demonstrate similar behaviour of the 2DEG-band. In both cases the 2DEG-band PL decreases by a few percent. By careful tuning of the temperature, it would be easily possible to match exactly the same percentage of 2DEG-band intensity reduction by both, FIR modulation and an externally induced lattice temperature increase. In a nutshell, it would be hard to distinguish between FIR influence and simple lattice heating just by the means of 2DEG-band PL modulation.

The X-band PL modification, however, allows to distinguish between an equilibrium temperature increase and FIR induced 2DEG heating. For better visibility Fig. 7.3 (c) and (d) show the X-band PL only, under FIR modulation (c) and lattice temperature increase (d). While FIR irradiation increases the overall X-band PL intensity by 12%, the temperature increase from $T = 2.2\ K$ to $T = 2.5\ K$ leads to an intensity redistribution between the respective X-band lines. Namely low energy X-band features are weakened and the high energy peak is intensified. With further increasing temperatures ($T = 9.7\ K$, see Fig. 7.3 (b)) the X-band PL shape modification becomes more and more pronounced: the low energy lines virtually disappear and the former weak high energy shoulders develop to pronounced features, larger than 50% of the main X line. The main X feature only barely varies in intensity, even for high temperatures.

In summary, the experiments indicate the FIR PL modulation to be dominated by a phonon wind: While the 2DEG barely feels the difference of FIR heating or external temperature increases, the excitons experience a directed force of a phonon wind only for 2DEG heating and not for an overall temperature increase. In that case, the exciton dissociation at the HJ should be reduced, as the phonon wind reduces the exciton drift towards the 2DEG. A reduced exciton dissociation in turn means an increased exciton density which manifests experimentally in the increased X-band PL. For low FIR powers, as it is the case in Fig. 7.3 (a), no pronounced X-band shape modification is observed. This demonstrates, that the exciton temperature barely increases by FIR irradiation. Consequently, the X-band PL modulation under FIR radiation seems to be dominated by an exciton drag.

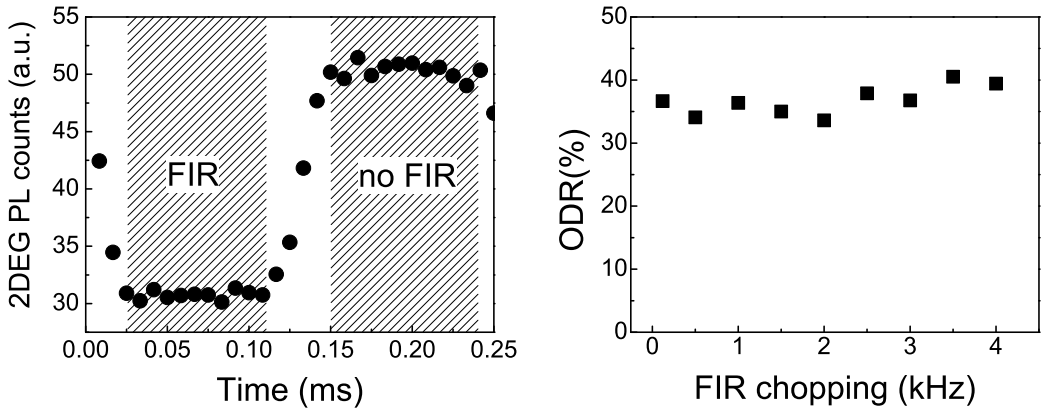


Figure 7.4: Time resolved ODCR in the linear ODR regime. Panel (a) shows the 2DEG amplitude variation over time for 4 $kHz$ FIR modulation. In panel (b) the 2DEG ODR signal is plotted against the modulation frequency. $T = 2.2\ K$, $n_e = 1.84 \cdot 10^{11} cm^{-2}$, $P_{785nm} = 0.30\ mW/cm^2$ and $E_{\mathrm{FIR}} = 10.433\ meV$.

### 7.1.4 Time-resolved ODR

More indicators for a phonon mediated 2DEG-exciton interaction can be found in a time resolved FIR-ODR experiment.

Assuming, purely hypothetically, the ODR would be based on overall lattice heating, such that the samples temperature $T$ exceeds the ambient temperature $T_a$, there must be heat transfer via the samples surface to the surrounding helium. Depending on the cooling efficiency of the helium bath, the sample temperature will exceed the ambient temperature by a small temperature difference $\Delta T$. At a certain time $t = 0$ the FIR illumination is abruptly interrupted and consequently the sample cools down to the ambient temperature $T_a$. The characteristic timescale for that process is given by the cooling time $\tilde{\tau}$. A rough estimation of $\tilde{\tau}$ is provided by Newtons law of cooling

$$\frac{\delta T}{\delta t} = \frac{hA}{C}(T(t) - T_a). \tag{7.1}$$

Here, $C$ is the samples heat capacity, $A$ is its surface and $h$ is the heat transfer coefficient. Eq. 7.1 is solved by an exponential decay

$$T(t) = \Delta T\ exp\left(\frac{hA}{C}t\right) + T_a. \tag{7.2}$$

Therefore the typical timescale for temperature equalization is

$$\tilde{\tau} = \frac{C}{hA}. \tag{7.3}$$

In a bath of liquid helium the large heat transfer coefficient of about $h = 5\ kW/m^2K$ [66] leads to a fast temperature equalization within a few $\mu s$ only. In helium gas, however, the heat transfer coefficient is much smaller $h = 0.025\ kW/m^2K$ [66], causing a slow cooling process, not faster than $1\ ms$. This means that the ODCR signal, based on overall lattice heating, in a sample, exposed to helium gas, should decay on a timescale $\tilde{\tau} > 1\ ms$.

In contrast to the $\mu s$-range in liquid helium, ODR decay timescales of a few $ms$ are easily accessible by a mechanically chopped FIR laser (see Sec. 4). For that purpose the sample is exposed to helium gas and the time dependent ODR amplitude is recorded, as shown in Fig. 7.4 (a) for the 2DEG-band at $4\ kHz$ chopping frequency. One full $0.25\ ms$ period of opened and closed FIR beam is presented and in well agreement with previously shown multichannel detector experiments, the 2DEG-band PL decreases under FIR illumination. The regions of full FIR illumination and complete blocking of the FIR beam are marked by dashed boxes, in which the PL amplitude is virtually constant. In between, the ODR signal transfers from the low to the high plateau within less than 41 $\mu s$, much faster than the estimated cooling times of a few $ms$. However, a phonon wind could react on such timescales, as the full relaxation time of the phonon hotspot in the 2DEG does not exceed several $\mu s$ [67].

For temperature relaxation times in the $ms$-range, one would expect the ODR signal to drop significantly for frequencies exceeding $1/\tilde{\tau} = 1\ kHz$ [68], as the slow cooling of the sample does not allow a lattice heating based ODR to react sufficiently fast. However, the ODR signal presented in Fig. 7.4 (b) is definitely not dropping, up to chopper frequencies of $4\ kHz$. The 2DEG-band ODR sticks at $38 \pm 5\%$ for the whole investigated frequency range. Together with the fast transition time of 41 $\mu s$, everything points to an ODR mechanism which cannot be explained by simple lattice heating effects only.

### 7.1.5 FIR power dependence

All the data presented previously was measured at the same low FIR excitation density of $P_{\mathrm{FIR}} = 1.8\ mW/cm^2$. It turns out, that $P_{\mathrm{FIR}} = 1.8\ mW/cm^2$ is a particularly good choice to discuss the ODR mechanism.

Comparing several FIR excitation densities, as done in Fig. 7.5, essentially different X-band PL modulations appear at different FIR excitation powers, while the typical 2DEG-band PL quenching is present for all FIR excitation densities.

The X-band PL of the already extensively discussed $P_{\mathrm{FIR}} = 1.8\ mW/cm^2$ shows a significant modulation by FIR radiation which is fundamentally different to that, induced by external temperature variations (compare Sec. 7.1.2).

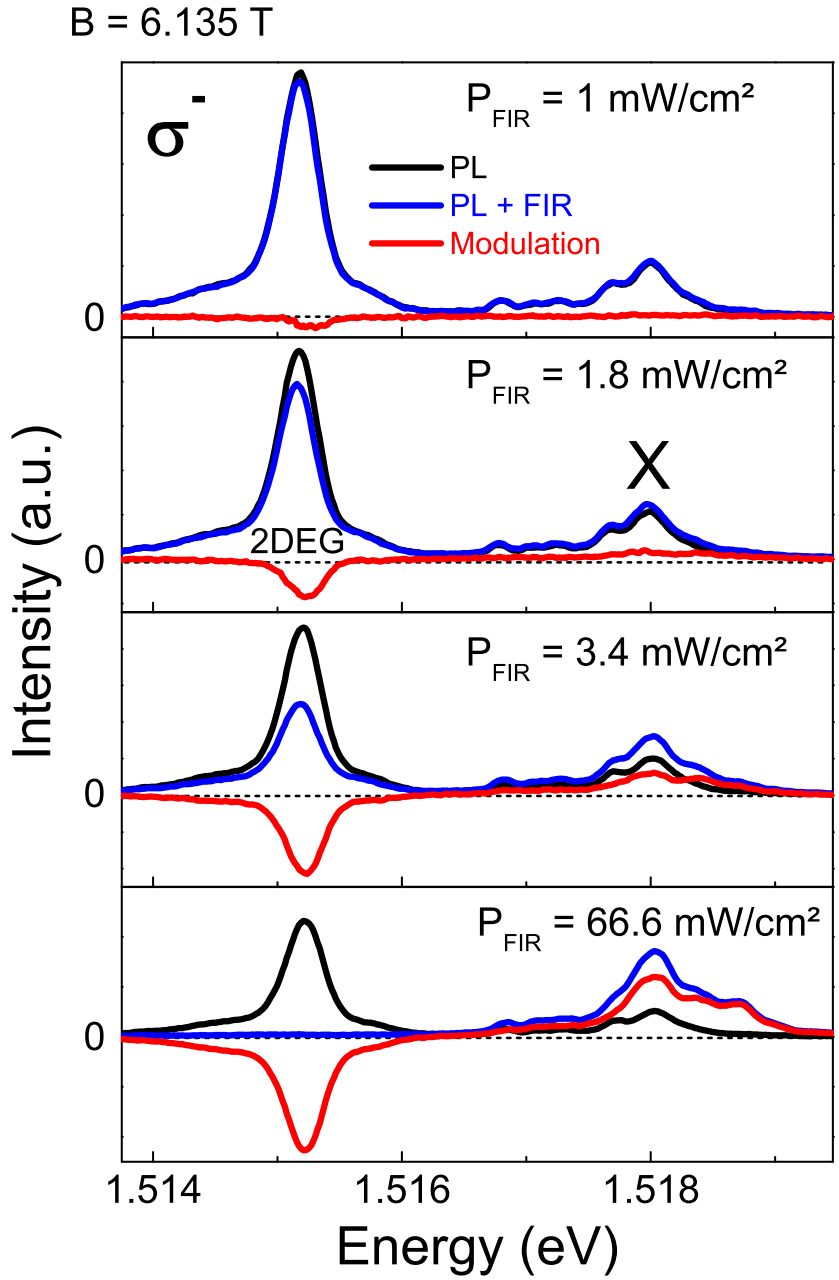


Figure 7.5: FIR power dependence of the PL modulation: PL (black), PL+FIR (blue) and modulation spectra (red) for four different FIR power densities $P_{\mathrm{FIR}}$ at the CR magnetic field for $T = 2.2K$, $n_e = 1.84 \cdot 10^{11} cm^{-2}$, $P_{785nm} = 0.30\ mW/cm^2$ and $E_{\mathrm{FIR}} = 10.433\ meV$.

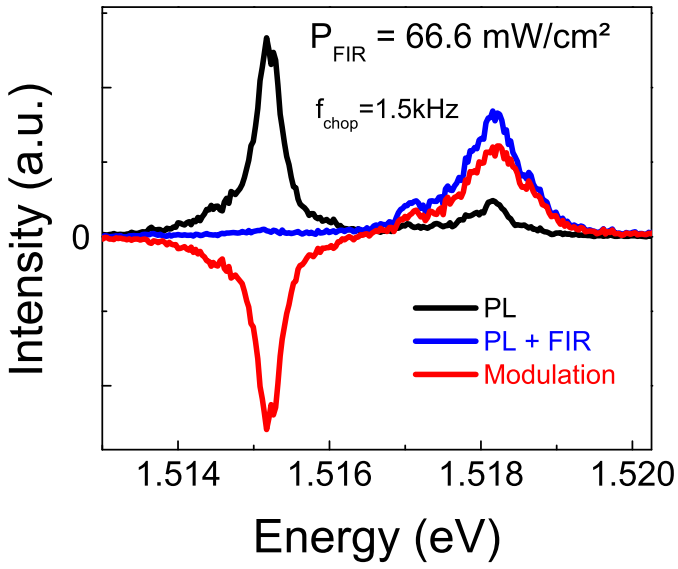


Figure 7.6: FIR PL modulation with a mechanically chopped FIR laser at 1.5 $kHz$: The curves show the pure PL (black), the PL with full FIR irradiation (blue) and the respective modulation spectrum (red) at the highest FIR excitation density $P_{\mathrm{FIR}} = 66.6\ mW/cm^2$ at the CR magnetic field $B = 6.135\ T$ for $T = 2.2K$, $P_{785nm} = 0.30\ mW/cm^2$, $n_e = 1.84 \cdot 10^{11} cm^{-2}$ and $E_{\mathrm{FIR}} = 10.433\ meV$.

Here a phonon wind, emitted by the hot 2DEG, is probably the dominant ODR mechanism. For even lower FIR powers, namely $P_{\mathrm{FIR}} = 1\ mW/cm^2$, the 2DEG-band PL slightly decreases under FIR influence by 3 %, correspontding to the typical hot electron PL modulation character. The X-band PL on the other hand does not change at all. It seems the 2DEG heating is too weak to emit sufficient phonons for a significant exciton drag. At higher powers $P_{\mathrm{FIR}} = 3.4\ mW/cm^2$ the 2DEG-band PL indicates strong 2DEG heating, reducing its intensity by 45 %. The X-band PL basically increases in the same way as for $P_{\mathrm{FIR}} = 1.8\ mW/cm^2$, suggesting the same physical interpretation. However, there seems to be a weak X-band intensity redistribution as well. This becomes clearly obvious for the highest FIR excitation density $P_{\mathrm{FIR}} = 66.6\ mW/cm^2$. The main X-band PL feature increases dramatically by 230 % and in particular the high energy exciton lines are strongly amplified under FIR irradiation. There is no doubt about X-band intensity redistribution here, clearly indicating exciton heating at this FIR excitation density. Again, it is no pure effect, as the huge increase of the main X-band line cannot be explained by exciton heating only. Probably there is a superposition of exciton drag and heating. The exciton heating is

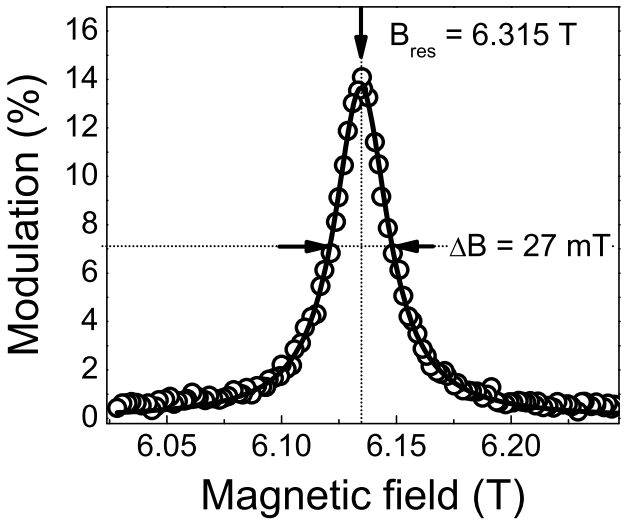


Figure 7.7: ODCR at a low FIR excitation density of $P_{\mathrm{FIR}} = 1.8\ mW/cm^2$. The measured data (open symbols) is fitted by Eq. 7.6 (solid line). $T = 2.2\ K$, $n_e = 1.84 \cdot 10^{11} cm^{-2}$, $P_{785nm} = 0.30\ mW/cm^2$ and $E_{\mathrm{FIR}} = 10.433\ meV$.

probably caused by nonequilibrium phonons rather than by lattice heating, as the following experiment with chopped FIR beam demonstrates:

In Fig. 7.6 PL spectra of a gated CCD are presented for full FIR illumination and no FIR illumination at a chopping frequency of $f = 1.5\ kHz$, again with a sample surrounded by helium gas. Simple lattice heating based ODR should not be able to react fast enough under these conditions to follow a FIR modulation by $f = 1.5\ kHz$ (see Sec. 7.1.4). However, the X-band PL is strongly modulated by the chopped FIR radiation, indicating a significant exciton heating contribution by nonequilibrium phonons.

### 7.1.6 CR linewidth and 2DEG mobility

In the previous sections the resonance field of the ODR was used to identify the basic resonance principle as electron CR. Here, the same ODR should be picked up again and investigated in more detail in terms of of resonance width and lineshape.

Fig. 7.7 shows the same data points, as already presented in Fig. 7.2 (b). A linewidth of $\Delta B = 27\ mT$ is measured, which is, to the best of our knowledge, the narrowest FIR ODCR in semiconductors reported to date. The narrow linewidth enables to estimate realistic values of the 2DEG mobility by applying a simple Drude model based calculation of FIR absorption, pre-

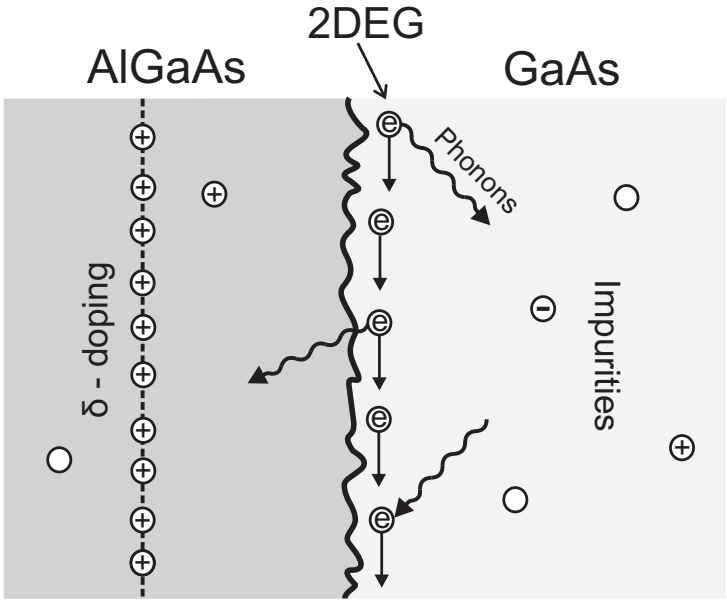


Figure 7.8: Schematic depiction of the scattering mechanisms of a 2DEG, confined in a GaAs/AlGaAs HJs potential notch. Impurities are shown as open symbols, marked by its respective charge, phonons are shown as curly arrows, electrons are marked by "$e$"and the rough GaAs/AlGaAs interface is given by a thick black line. The figure is plotted in analogy to [69].

sented in the following paragraphs. The resulting data interpolation is given as a black solid line in Fig. 7.7.

The electron mobility is introduced in the Drude model (see Sec. 2.2) to describe a limited electron mean free path by the means of finite electron scattering times. Several electron scattering mechanism are known in GaAs/AlGaAs HJs [69, 70]. A schematic depiction of the electron scattering at the HJ is presented in Fig. 7.8. Even in a perfect sample, electron scattering by phonons, alloy scattering due to penetration of carriers into the AlGaAs layer barrier and scattering by remote ionized impurities in the $\delta$-doping sheet is not avoidable. Due to imperfections in the sample growth process ionized and neutral impurities in the GaAs layer and a certain interface roughness cannot be averted and additional electron scattering occurs. Depending on the temperature, different mechanisms dominate the scattering. At low temperatures acoustic phonon scattering and impurity scattering play the main role [71]. In high quality samples remote impurity scattering is especially important [69, 72]. The particular scattering times are summarized

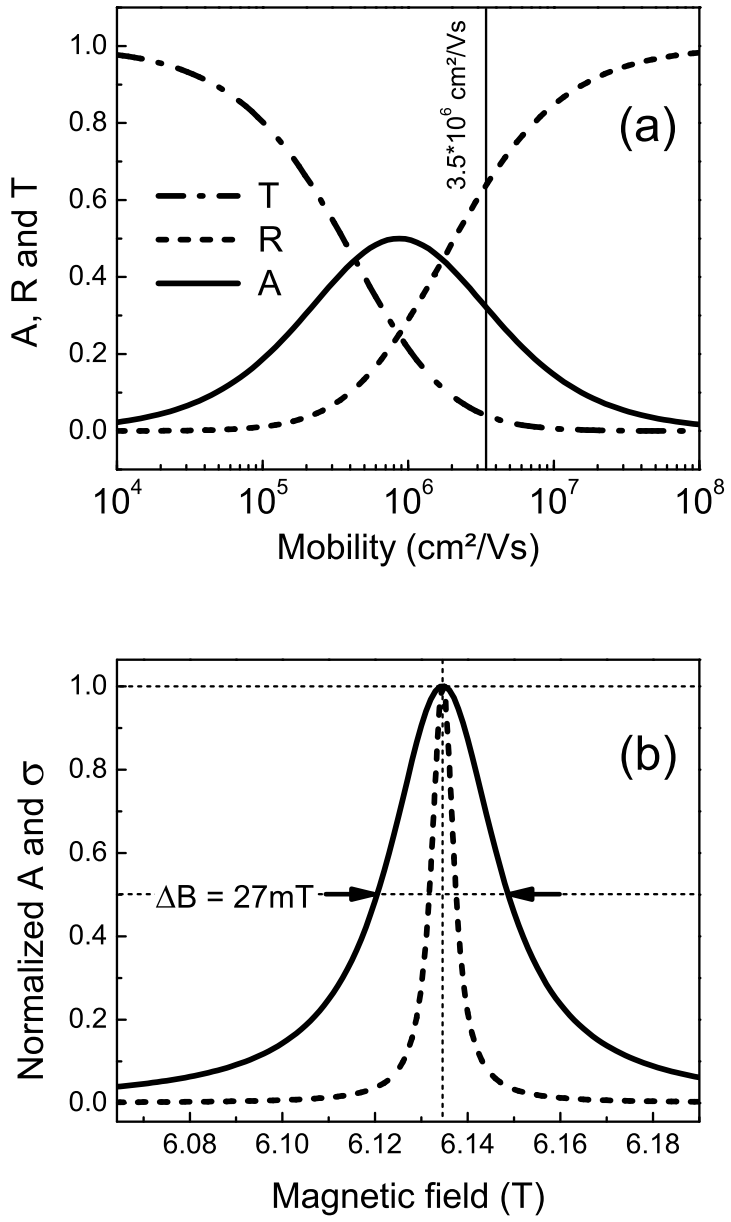


Figure 7.9: (a): Calculated FIR absorption $A$, reflection $R$ and transmission $T$ according to Eq. 7.6 versus the 2DEG mobility for a constant electron density $n_e = 1.84 \cdot 10^{11} cm^{-2}$ at $B = B_{res}$ and $n_{GaAs} = 4.9$. (b): Normalized FIR absorption (solid line) and the real part of the cyclotron active component of the Drude conductivity $\sigma'_+$ (dashed line) in the vicinity of the electron-CR magnetic field $B_{res} = 6.135\ T$ for $n_{GaAs} = 4.9$, $\mu = 3.5\ cm^2/Vs$, $n_e = 1.84 \cdot 10^{11} cm^{-2}$ and $E_{\mathrm{FIR}} = 10.433\ meV$.

to a total scattering time $\tau$, which is typically assumed to follow

$$\frac{1}{\tau} = \sum_i \frac{1}{\tau_i}, \tag{7.4}$$

where $i$ runs over all scattering mechanisms. $\tau$ is the same total scattering time, used in the Drude formalism (see Sec. 2.2). The total mobility $\mu$ is obtained according to Eq. 2.67

$$\mu = \frac{e\tau}{m^*}. \tag{7.5}$$

The Drude model predicts a Lorentzian CR lineshape (Eq. 2.64) and the electron mobility can be directly estimated by the CR full linewidth $\Delta B$ (Eq. 2.67). However, this assumption is not generally true, as the Drude conductivity is not directly accessible by FIR transmission or FIR ODCR measurements. The former measures the transmitted FIR power, while the latter is related to the absorbed FIR power, both absorption and transmission do not reflect the lineshape of the conductivity necessarily: For high electron densities and high mobilities, the 2DEG at CR condition behaves as a metallic mirror and strong FIR reflections might occur. This results in a broadening of absorption and transmission linewidths, obscuring the real electron mobility. To obtain realistic values it is necessary to take into account the reflected FIR.

Following the boundary conditions for the FIR electric field at the 2DEG plane [73, 74, 75], FIR transmission $T$, reflection $R$ and absorption $A$ read

$$\begin{aligned} T &= \left( \frac{2\, n_{\mathrm{GaAs}}/Z_0}{2(n_{\mathrm{GaAs}}/Z_0) + \sigma} \right)^2 \\ R &= \left( \frac{\sigma}{2\,(n_{\mathrm{GaAs}}/Z_0) + \sigma} \right)^2 \\ A &= 1 - T - R. \end{aligned} \tag{7.6}$$

$Z_0 = 377\ \Omega$ is the impedance of the free space and $n_{\mathrm{GaAs}} = 4.9$ is the refractive index of GaAs at $E_{\mathrm{FIR}} = 10.433\ meV$ [76]. The refractive index of AlGaAs at that photon energy barely differs from $n_{\mathrm{GaAs}}$ and is be considered as identical consequently. $\sigma$ is the complex Drude conductivity according to Eq. 2.62.

Using Eq. 7.6 FIR absorption, transmission and reflection are plotted against the electron mobility in Fig. 7.9 (a) for the native electron density at $B = B_{res}$. For low mobilities $\mu = 10^4\ cm^2/Vs$, there is a small amount of radiation absorbed and the largest part is transmitted. Larger 2DEG

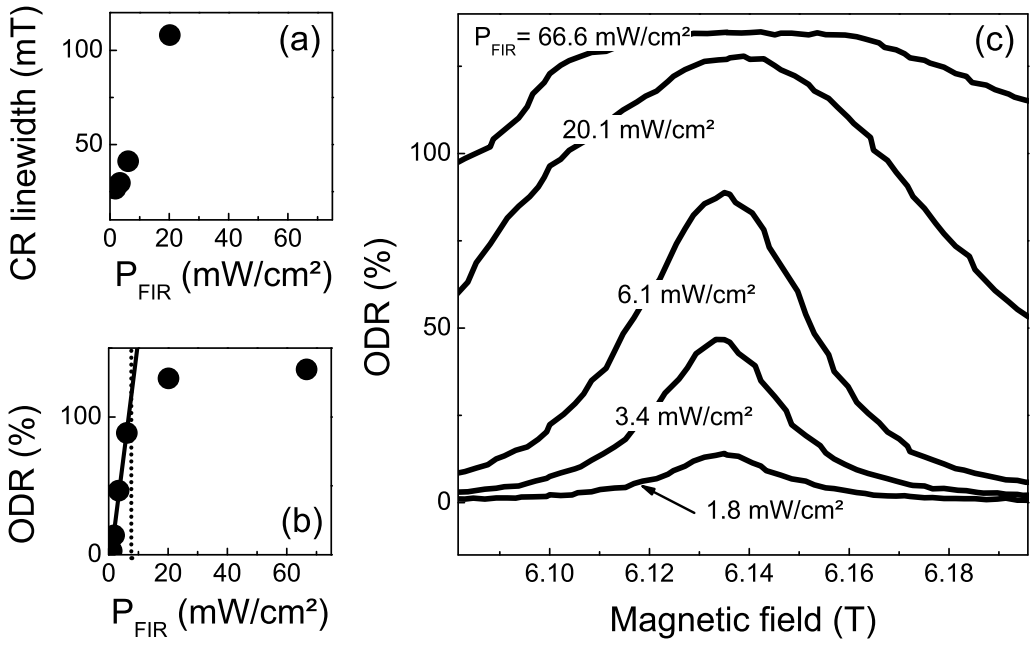


Figure 7.10: FIR power density dependencies of the ODR linewidth (a) and the ODCR signal strength (b) plotted against $P_{\mathrm{FIR}}$ . The linear ODR-regime is represented by a solid line. Panel (c) shows the ODCR-signal vs. the magnetic field at different $P_{\mathrm{FIR}}$. $T = 2.2\ K$, $n_e = 1.84 \cdot 10^{11} cm^{-2}$, $P_{785nm} = 0.30\ mW/cm^2$ and $E_{\mathrm{FIR}} = 10.433\ meV$.

mobilities cause the absorption to increase to $A = 0.5$ at $\mu \approx 10^6\ cm^2/Vs$, where also the reflection starts to increase noticeably until the FIR-radiation is almost completely reflected at $\mu = 10^8\ cm^2/Vs$. Consequently, one should expect significant reflections for the investigated HJ with a 2DEG mobility of $\mu \approx 3 \cdot 10^6\ cm^2/Vs$ [2].

Without reflections, i.e. for sufficiently low mobilities, the shape of the CR line coincides with the real part of the cyclotron active component of the Drude conductivity $\sigma'_+$. For finite reflection however, the CR line is considerably broadened, as exemplarily shown in Fig. 7.9 (b). Here $\sigma'_+$ and the broadened FIR absorption are plotted and normalized for better comparability of the lineshapes. Apart from different amplitudes, transmission and reflection have exactly the same shape as the absorption line. The parameters for the plots in Fig. 7.9 (b) are obtained by a fit of the experimental data of Fig. 7.7 by Eq. 7.6. Assuming $n_{\mathrm{GaAs}} = 4.9$, $n_e = 1.84 \cdot 10^{11} cm^{-2}$ and $E_{\mathrm{FIR}} = 10.433\ meV$ the interpolation provides $B_{res} = 6.135\ T$ and

[2]Estimated from transport measurements.

$\mu = 3.5 \pm 0.5\ 10^6\ cm^2/Vs$.

Although the uncertainty of the mobility does not allow to calculate highly precise values, the successful fitting and the realistic output parameters indicate that the model includes the main mechanisms of the ODCR linewidth broadening: First a finite electron scattering time according to the Drude model and second a broadening due to reflections at the highly conductive 2DEG.

Furthermore the successful fitting of the ODCR by the calculated FIR absorption indicates a linear dependence

$$ODCR(B) = \alpha\ A(B). \tag{7.7}$$

If there was no pure linear relation, the ODCR lineshape would be deformed in respect to the absorption and the fitting would fail or result in wrong output parameters. At higher FIR powers such a deformation is easily realized, as presented in Fig. 7.10 (c). Already for $P_{\mathrm{FIR}} = 6.1\ mW/cm^2$ the ODCR line is broadened to $\Delta B = 41\ mT$, for even higher excitation densities the resonance is increasingly broadened until it is drastically deformed at $P_{\mathrm{FIR}} = 66.6\ mW/cm^2$. For $P_{\mathrm{FIR}} < 6.1\ mW/cm^2$ the ODCR linewidth is about constant $\Delta B = 28 \pm 1\ mT$, as expected for a linear ODR regime (Eq. 7.7). In fact, the assumption of a linear ODR regime is valid for $P_{\mathrm{FIR}} < 6.1\ mW/cm^2$, as Fig. 7.10 (b) confirms. The ODR amplitude increases linearly with increasing FIR power. Beyond $P_{\mathrm{FIR}} = 6.1\ mW/cm^2$ the ODCR amplitude does not increase linearly any more and tends to saturate. This strong nonlinearity explains the deformation of the resonance at high excitation powers.

## 7.2 Electron-density dependence

As described in Sec. 5, gentle above barrier illumination allows to modify the 2DEG density conveniently. Starting from the native electron density $n_e = 1.84 \cdot 10^{11} cm^{-2}$, the 2DEG is depleted gradually down to a density of $n_e = 0.72 \cdot 10^{11} cm^{-2}$ and the ODCR is measured as a function of the electron density. For the sake of overview, a selection of ODCRs for different electron densities is shown in Fig. 7.11. On the basis of this figure, mainly two influences of the electron density on the ODCR attract attention. Firstly, there is a shift in the resonance position. Apart from minor deviations the resonance position shifts to lower magnetic fields with decreasing electron density for the whole studied field range. Secondly, there is a resonant increase of the ODCR amplitude at $n_e = 1.46 \cdot 10^{11} cm^{-2}$ (red line in Fig. 7.11) which cor-

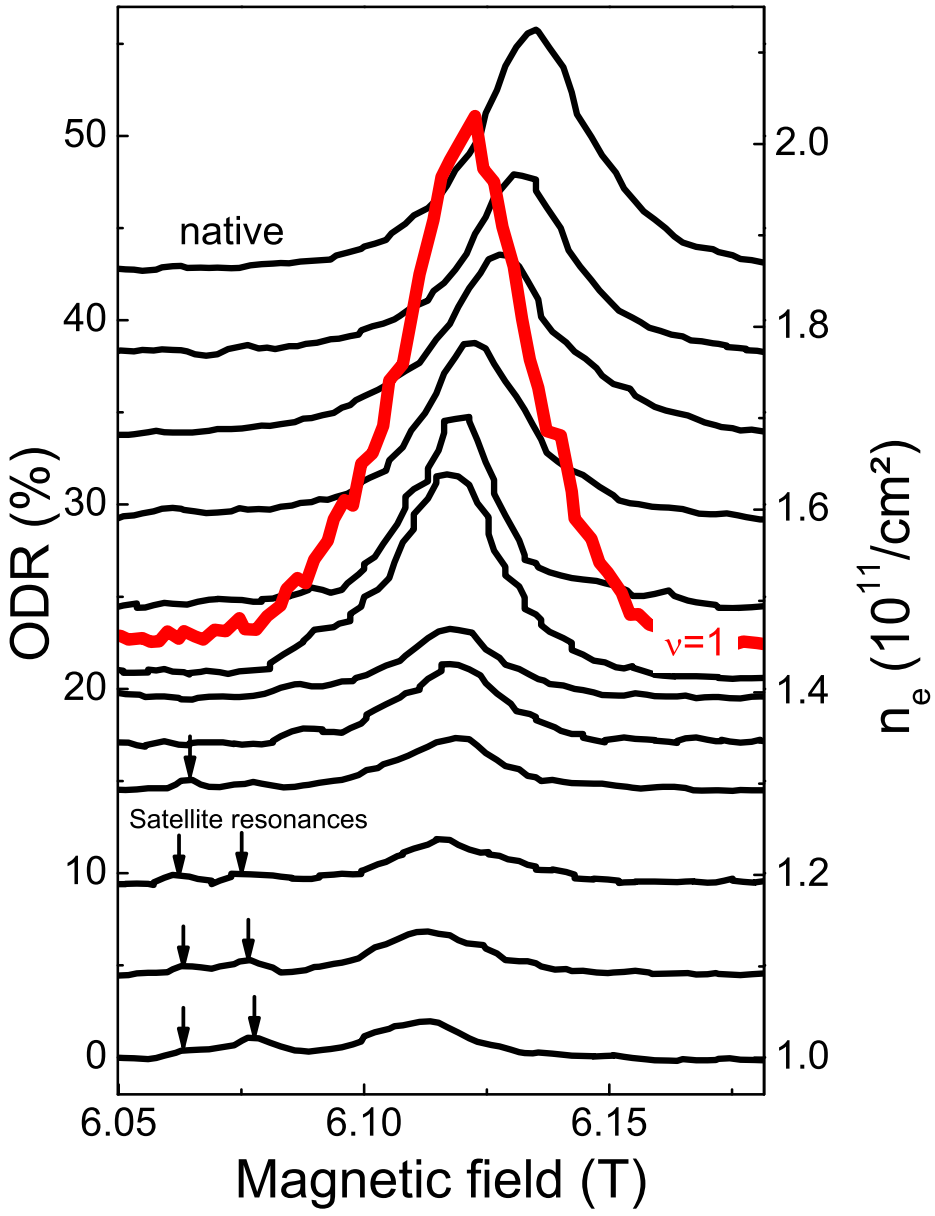


Figure 7.11: ODCR signal versus $B$ for several different electron densities. The ODCR curves are shifted vertically, according to the respective electron density, shown on the right y-axis. The ODCR at filling factor $\nu = 1$ at is highlighted by a thick red line. $P_{\mathrm{FIR}} = 1.8\ mW/cm^2$, $T = 2.2\ K$ and $E_{\mathrm{FIR}} = 10.433\ meV$.

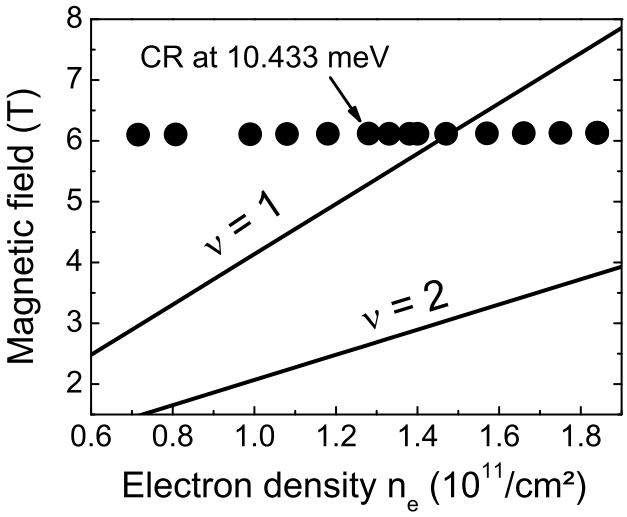


Figure 7.12: Filling factors $\nu = 1$ and $\nu = 2$ (solid lines) in the coordinates of electron density $n_e$ and magnetic field $B$ according to Eq. 2.28. The measured ODCR resonance fields $B_{res}$ for $E_{\mathrm{FIR}} = 10.433\ meV$ are shown by solid symbols.

responds well to filling factor $\nu = 1$ (see Fig. 7.12). It is accompanied by a constant difference of ODCR amplitude for $\nu < 1$ and $\nu > 1$.

A detailed analysis of the main ODCR under variation of the electron density will be given in sections 7.2.1, 7.2.2 and 7.2.3. Fundamental parameters as the ODCR linewidth, the ODCR amplitude and the effective mass are treated separately in there. Amplitude and linewidth are directly obtained by fitting the respective ODCR with a Lorentz-function, the effective electron mass is calculated by Eq. 2.66 via the center magnetic field from the Lorentz-fit.

Besides the dominant effects related to the main resonance, weak satellite resonances close to the CR position can be revealed. They are barely visible in Fig. 7.11 (black arrows) but appear clearly in a more detailed data presentation (see Sec. 7.2.4).

### 7.2.1 The effective mass

This section is dedicated to the ODCR center field under electron density variations. The ODCR line in Fig. 7.11 shifts to lower magnetic fields with increasing 2DEG depletion. According to Eq. 2.66 this means the effective mass to increase with the electron density. This could be verified by extracting the center magnetic field positions from ODCR interpolations with

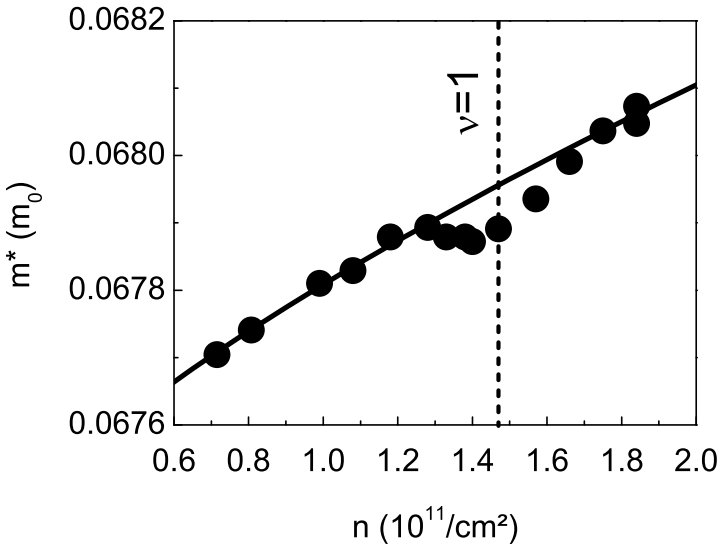


Figure 7.13: Electron-density dependence of the effective electron mass, estimated from Lorentz-fitting of ODCR curves, shown in Fig. 7.11. The solid line represents a calculation according to Eq. 7.11. Filling factor $\nu = 1$ at $B = B_{res}$ is illustrated by a dashed line. $P_{\mathrm{FIR}} = 1.8\ mW/cm^2$, $T = 2.2\ K$ and $E_{\mathrm{FIR}} = 10.433\ meV$.

Lorentz-functions and translating them to effective mass values, as presented in Fig. 7.13.

All effective mass values are slightly larger than the typical bulk GaAs electron mass $m^*_{GaAs} = 0.067\ m_0$. The effective mass of the native electron density is found to be $m^* = 0.0680\ m_0$, decreasing almost linearly down to $0.0677\ m_0$ at $n_e = 0.72 \cdot 10^{11} cm^{-2}$. At $\nu = 1$ a kink in the otherwise smooth effective mass dependence appears.

Obviously a constant effective electron mass could not provide a satisfying explanation for the experimental data. It seems the approximations assumed in Sec. 2.1.1 do not hold for the electron density variations presented here. Going beyond the approximation of a constant effective mass means assuming a not fully parabolic conduction band, namely including higher orders of $k$ to the electron dispersion. Presuming a symmetric conduction band, the 3D-dispersion for zero magnetic field reads

$$E(k) = \frac{\hbar^2 k^2}{2m_0^*} + \frac{K_2}{E_G}\left[\frac{\hbar^2 k^2}{2m_0^*}\right]^2 \tag{7.8}$$

up to the fourth order in $k$. $m_0^*$ corresponds to the effective mass of a fully parabolic band. $K_2$ is a parameter, representing the band nonparabolicity.

It was initially introduced by Palik et al. [37] according to a three band $kp$-perturbation model [77, 78]. In magnetic fields and with a confinement potential in the $z$-direction the conduction band energies are

$$E(N, \langle T_z \rangle) = (N + 1/2)\,\hbar\omega_c + \langle T_z \rangle + \frac{K_2}{E_g}\left((N + 1/2)\,\hbar\omega_c + \langle T_z \rangle\right)^2 . \quad (7.9)$$

$\langle T_z \rangle$ is the kinetic energy in the $z$-direction. Note, that spin effects are neglected in this simple picture. The effective mass, measured by ODCR is consequently defined according to the energy difference of Landau levels $N$ and $N + 1$

$$\frac{1}{m^*} = \frac{1}{e\,B}\,E(N + 1, \langle T_z \rangle) - E(N, \langle T_z \rangle) \quad (7.10)$$

$$= \frac{1}{m_0^*}\left[1 + \frac{2\,K_2}{E_g}\left((N + 1)\,\hbar\omega_c + \langle T_z \rangle\right)\right] . \quad (7.11)$$

Eq. 7.11 is widely used to describe effective mass variations due to nonparabolicity effects in FIR transmission experiments [58, 79, 41, 12]. The ODCR lines presented in this work are very narrow. That provides sufficient resolution in $B$ to investigate nonparabolicity effects in ODCR studies.

The kinetic energy in $z$-direction is related to the confinement potential, naturally. It can be shown, that in a triangular confinement potential, $\langle T_z \rangle = \frac{1}{3}\,E_1^{tri}$ is a good approximation [58]. As $E_1^{tri}$ is a function of the electron density (see Eq. 6.6), the effective mass in a nonparabolic band becomes a function of the electron density as well, described by inserting $\langle T_z \rangle = \frac{1}{3}\,E_1^{tri}$ into Eq. 7.11.

The solid line in Fig. 7.13 is a fit of the experimental data, according to Eq. 7.11 and assuming $\langle T_z \rangle = \frac{1}{3}\,E_1^{tri}$. Five data points in the vicinity of $\nu = 1$ were not included in the interpolation, as such integer filling factor anomalies can not be described by the simple model applied. Apart from the kink at $\nu = 1$ the fit coincides well with the experiment, resulting in $K_2 = -0.68$ and $m_0^* = 0.067$. $m_0^*$ corresponds to the well known values for GaAs. $K_2 = -0.68$ however deviates from other publications. A summary of reported $K_2$ values can be found in reference [58] and reference [12], where $K_2 = -0.83$ is obtained from a basic three band $kp$-perturbation calculation. More complex band structure calculations result in even stronger nonparabolicity $K_2 < -1.1$. Additionally, polaron effects are expected to increase the measured nonparabolicity even more [80]. The significant deviations of $K_2$ from literature values can not be attributed to the optical detection technique, as the estimated effective masses from ODCR measurements coincide with values obtained from absorption measurements, presented in Sec. 7.2.4.

Probably the simple model for the confinement potential and consequently poor approximation of $\langle T_z \rangle$ cause the abnormal value of nonparabolicity. Most likely more complex theoretical treatment of the confinement potential is needed to get quantitatively reliable values for $K_2$.

A dip in the effective mass at $\nu = 1$, similar to that one in Fig. 7.13 is reported by Manger et. al. [81]. The authors present a physical explanation which requires to consider both, electron-electron interaction and electron-phonon interaction: At $\nu < 2$ the 2DEG can populate both spin states of the lowest Landau level, resulting in two subsystems of electrons with different effective masses, due to band nonparabolicity [82]. Only one resonance is observed nevertheless due to strong electron-electron interaction of the two subsystems and therefore the respective single resonances are "hidden by interaction"[81]. Assuming such a 2DEG system and taking into account polaron effects, an effective mass anomaly at $\nu = 1$ is predicted, as shown in Fig. 3 of [81]. The dip in the effective mass in Fig. 7.13 is probably based on the same physics.

### 7.2.2 ODCR linewidth

The ODCR linewidth is strongly affected by FIR reflection at the highly conductive 2DEG (see Sec. 7.1.6). While the width of the Drude-conductivity peak at electron CR is determined by the carrier mobility exclusively (see Eq. 2.67), the FIR absorption depends on the electron density as well (Eq. 7.6), especially at high electron densities and high mobilities. The experimentally obtained ODCR linewidth versus the 2DEG density is presented in Fig. 7.14. The relative noise level of $\pm 3\ mT$ suggests not to over-interpret the data but nevertheless an overall ascending linewidth with increasing electron density could be identified. In fact, Eq. 7.6 predicts a very similar behaviour. The solid black line in Fig. 7.14 corresponds to the calculated FIR absorption linewidth. Here, the same parameters are used, as in Sec. 7.1.6 for the ODCR fit at the natural electron density: $n_{GaAs} = 4.9$, $n_e = 1.84 \cdot 10^{11} cm^{-2}$, $E_{\mathrm{FIR}} = 10.433\ meV$ and $\mu = 3.5 \pm 0.5\ 10^6\ cm^2/Vs$. The 2DEG density dependent resonance field $B_{res}$ is taken from the experimental data, presented in Sec. 7.2.1.

Within the measurement accuracy, the basic Drude model for FIR absorption is able to explain the observed ODCR linewidth.

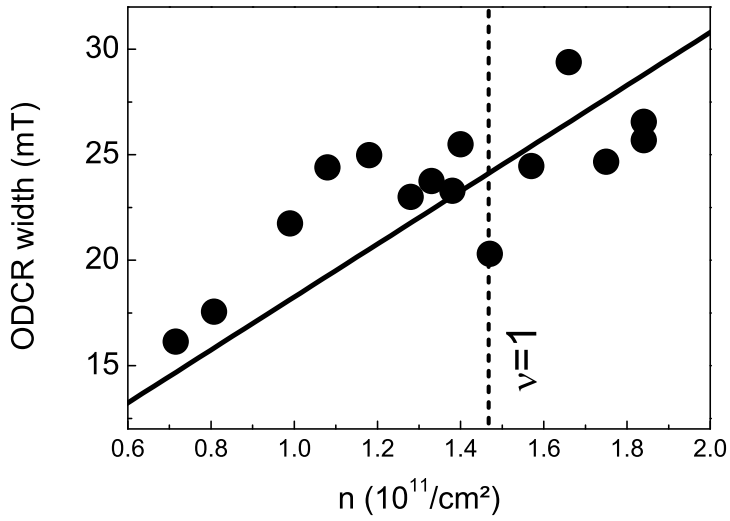


Figure 7.14: Electron-density dependence of the ODCR linewidth, estimated from Lorentz-fitting of ODCR curves, shown in Fig. 7.11. The solid line represents a calculation according to Eq. 7.6. Filling factor $\nu = 1$ at $B = B_{res}$ is illustrated by a dashed line. $P_{\mathrm{FIR}} = 1.8\ mW/cm^2$, $T = 2.2\ K$ and $E_{\mathrm{FIR}} = 10.433\ meV$.

### 7.2.3 ODCR amplitude

The ODR mechanism can be understood as a two step process, consisting of an initial 2DEG heating and a subsequent PL modulation by the hot electrons (see Sec. 7.1.1). Both steps naturally influence the ODCR spectrum.

The electron density dependencies of the ODCR position and linewidth can be clearly attributed to variations in the 2DEG heating exclusively. Non-parabolicity and polaron effects on the one hand and FIR reflection at the 2DEG on the other hand would be observed in the same way in FIR transmission CR experiments, i.e. the indirect CR detection by PL modifications simply works as a sensitive substitution of a FIR detector and shows no particular influence on CR position and linewidth. For the electron-density dependence of the ODCR amplitude the situation is different and the PL modulation mechanism shows strong influence on the ODCR amplitude.

Starting from the natural electron density $n_e = 1.84 \cdot 10^{11} cm^{-2}$ the ODCR amplitude remains on a constant level of $11 \pm 2$ % with increasing 2DEG depletion down to $n_e = 1.5 \cdot 10^{11} cm^{-2}$, as depicted by the solid black symbols in Fig. 7.13. Then the amplitude sharply increases, reaching 29% at $n_e = 1.46 \cdot 10^{11} cm^{-2}$. After that the amplitude drops abruptly and settles at $n_e = 1.46 \cdot 10^{11} cm^{-2}$ to another constant level of $3 \pm 1$ % and stays there for all

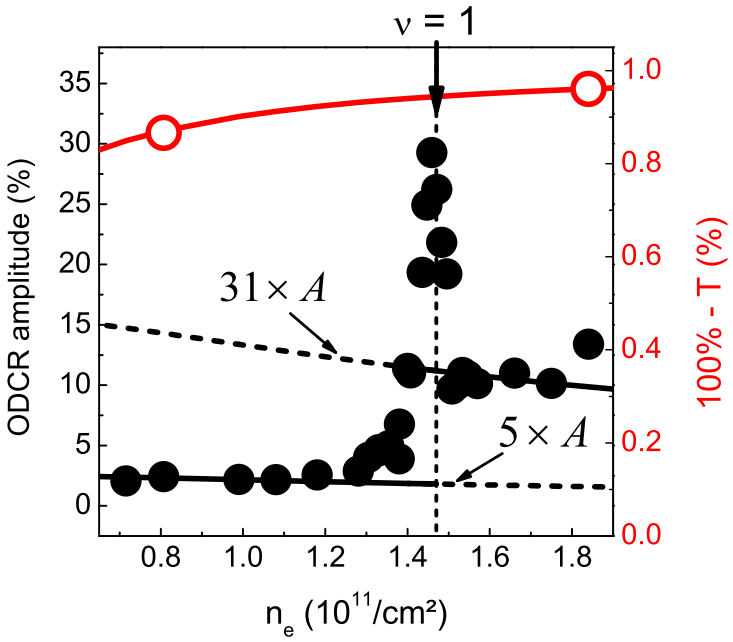


Figure 7.15: Electron-density dependence of the ODCR amplitude (black symbols), estimated from Lorentz-fitting of ODCR curves, shown in Fig. 7.11. The resonant FIR absorption $A$ is calculated according to Eq. 7.6 and illustrated by black lines. Two different scaling-factors, $\alpha = 31$ and $\alpha = 5$, fit the ODCR amplitudes for $\nu > 1$ and $\nu < 1$ respectively. Filling factor $\nu = 1$ is illustrated by a dashed line. As a red line the calculated FIR transmission CR amplitude $100\% - T$ is given. $T$ obeys Eq. 7.6 at $B = B_{res}$. Two open red symbols represent measured CR transmission data, extracted from Fig. 7.19. $P_{\mathrm{FIR}} = 1.8\ mW/cm^2$, $T = 2.2\ K$ and $E_{\mathrm{FIR}} = 10.433\ meV$.

lower 2DEG densities investigated. The ODCR discontinuity lies remarkably close to $\nu = 1$, shown as a dashed line in Fig. 7.15.

To find out, whether the 2DEG heating or the PL modulation is responsible for the discontinuity, it is illustrative to compare ODCR and the plain FIR transmission. FIR transmission experiments are naturally not affected by the PL modulation mechanism so that transmission experiments should not show anomalies in the electron-density dependence if the ODR mechanism is responsible for the discontinuity.

Literature investigations indicate that the discontinuity is caused by the PL modulation mechanism, as there is a number of FIR transmission experiments [58, 41, 83, 84, 79] and none of them mentions a discontinuity in the CR amplitude at $\nu = 1$. In contrast to that, the only study discussing the ODCR amplitude [10] shows a rapid drop in the ODCR amplitude at $\nu = 1$,

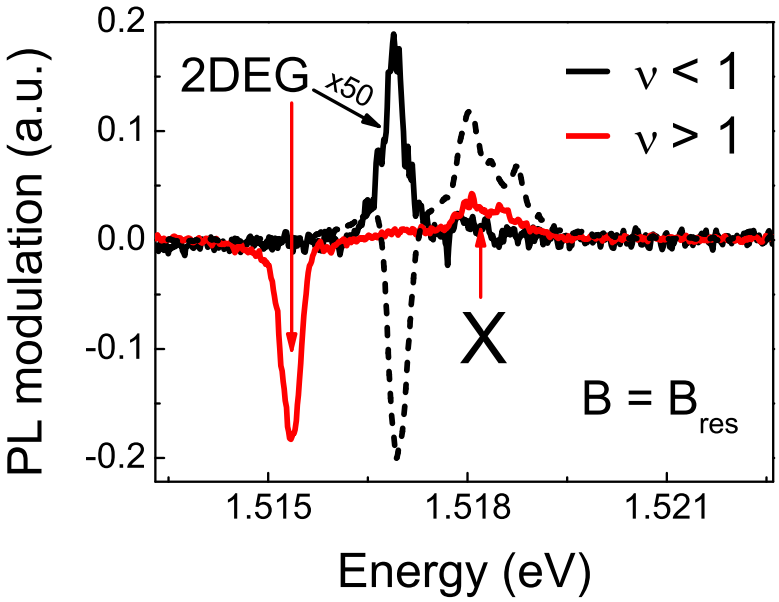


Figure 7.16: Modulation spectra for different experimental conditions: $n_e = 1.84 \cdot 10^{11} cm^{-2}$ and $P_{\mathrm{FIR}} = 1.8\ mW/cm^2$ (red), $n_e = 0.81 \cdot 10^{11} cm^{-2}$ and $P_{\mathrm{FIR}} = 1.8\ mW/cm^2$ (black), $n_e = 0.81 \cdot 10^{11} cm^{-2}$ and $P_{\mathrm{FIR}} = 20.2\ mW/cm^2$ (dashed black line). $B = B_{res}$, $T = 2.2\ K$ and $E_{\mathrm{FIR}} = 10.433\ meV$.

comparable to the one presented in Fig. 7.15.

Further evidence is obtained by a direct experimental comparison of ODCR and FIR transmission. For that purpose Fig. 7.15 shows CR transmission amplitudes for two electron densities, $n_e = 1.84 \cdot 10^{11} cm^{-2}$ and $n_e = 0.81 \cdot 10^{11} cm^{-2}$ (open red symbols). The transmission CR amplitude is defined as the difference of the non-resonant FIR transmission $T_0$ and the FIR transmission $T$ at cyclotron resonance. It can be easily simulated by assuming $T_0 = 100$ % and using Eq. 7.6 to calculate $T$ at $B = B_{res}$. Such a calculation is shown by the solid red line. It runs smoothly over all investigated electron densities, fitting well to both data points. No indication for abrupt intensity changes can be found.

Similar calculations for the ODCR base on the FIR absorption $A$ (Eq. 7.6), multiplied by a constant factor $\alpha$ (see Eq. 7.7)[3]. However, the model for the absorption does not reveal a discontinuity at $\nu = 1$ neither and no reasonable approximation for the whole range of 2DEG densities can be found. Omitting the narrow resonant amplitude increase at $\nu = 1$ for the first instance,

[3]Low FIR powers ($P_{\mathrm{FIR}} = 1.8\ mW/cm^2$) rectify the assumption of a linear ODR regime.

acceptable approximations can be only obtained by assuming different ODR dependencies for $\nu < 1$ and for $\nu > 1$, namely for $\alpha = 5$ and $\alpha = 31$. For both values of $\alpha$ the calculated ODCR amplitudes are plotted in Fig. 7.15 as black lines. Solid lines are used in the range fitting to the experimental values and dashed lines in the regions which do not fit the data. The resonant increase of ODCR amplitude at $\nu = 1$ is not comparable to the calculated FIR absorption in any way.

Beyond different values of $\alpha$ for $\nu < 1$ and for $\nu > 1$, the PL modulation shows even qualitative differences as summarized in Fig. 7.16. Two modulation spectra are presented for $n_e = 1.84 \cdot 10^{11} cm^{-2}$ and $n_e = 0.81 \cdot 10^{11} cm^{-2}$, exemplifying $\nu > 1$ and $\nu < 1$ respectively. The strong modulation signal for $\nu > 1$ shows an intensity decrease of the 2DEG-band and an intensity increase of the X-band. The $\nu < 1$ modulation shows no influence on the X-band, also typical for very weak ODCR at $\nu > 1$. However, the 2DEG-band PL intensity increases under FIR illumination, which could not be reproduced under any tested experimental conditions for $\nu > 1$ and could not be explained by the model of PL modulation presented in Sec.7.1.1. Probably there is another mechanism for very low ODCR signals, which frees additional holes for recombinations with the 2DEG. However, the effect is very weak (note a scaling factor of 50 in Fig. 7.16) and for higher FIR intensities the typical shape of PL modulation is recovered, shown as a dashed black line in Fig. 7.16).

In summary, the fundamental differences in the modulation spectra suggest the PL modulation mechanism to cause the ODCR discontinuity. This is supported by the fact that the PL is sensitive to the 2DEG ground state, which abruptly changes at $\nu = 1$ (see Sec. 6.2) and thus it could be expected that the PL modulation by hot electrons is also different for $\nu < 1$ and $\nu > 1$.

### 7.2.4 Satellite resonances

At all investigated electron densities with $\nu < 1$, two weak satellite resonances appear on the low field shoulder of the main CR, marked as S1 and S2 in Figures 7.17 (a) and 7.18 (a).

While the center field of the main CR is shifted with changing 2DEG density due to nonparabolicity effects (see Sec. 7.2.1), S1 and S2 stay at $B_{S1} = 6.077 \pm 3\ T$ and $B_{S2} = 6.063 \pm\ 3\ T$ for all electron densities. Furthermore the PL modulation of S1 and S2 differs essentially from that of the CR. While the CR shows a simple 2DEG-band intensity decrease or increase at low FIR excitation densities (Figures 7.17 (b) and 7.18 (b)), at the resonances S1 and S2 the 2DEG band experiences a shift to higher energies and the intensity is basically unchanged (Figures 7.17 (c), (d) and 7.18 (c)

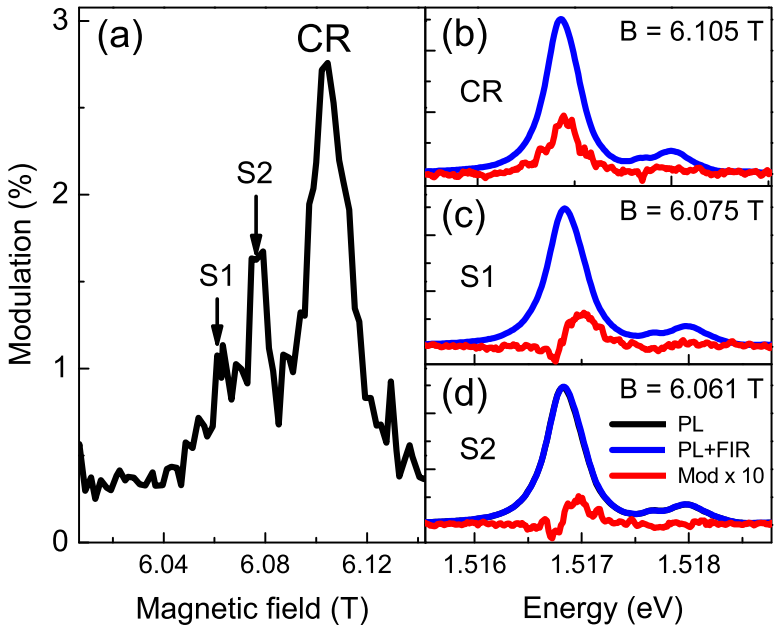


Figure 7.17: ODR curve (a) and the PL (black) PL+FIR (blue) and modulation spectra at the respective resonances. CR (b), S1 (c) and S2 (d). $P_{\mathrm{FIR}} = 1.8\ mW/cm^2$, $n_e = 0.81 \cdot 10^{11} cm^{-2}$, $T = 2.2\ K$ and $E_{\mathrm{FIR}} = 10.433\ meV$.

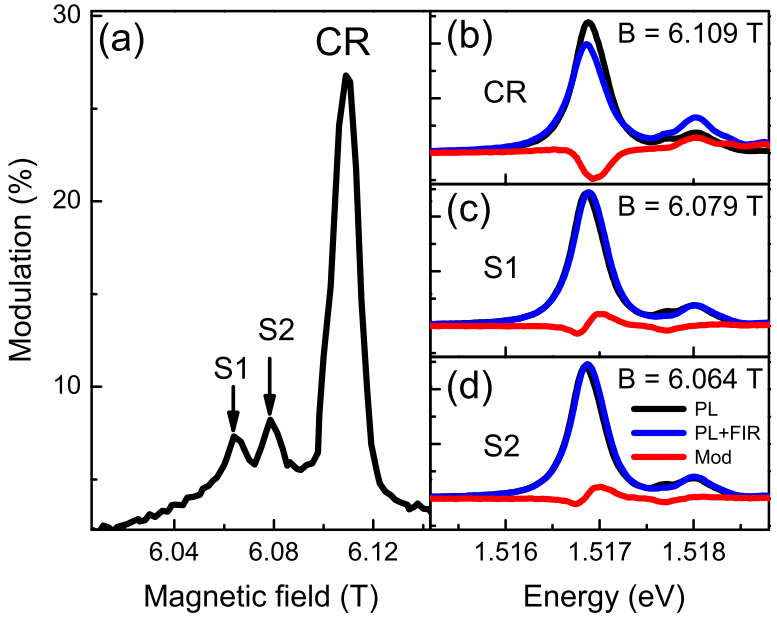


Figure 7.18: ODR curve (a) and the PL (black) PL+FIR (blue) and modulation spectra at the respective resonances. CR (b), S1 (c) and S2 (d). $P_{\mathrm{FIR}} = 20.2\ mW/cm^2$, $n_e = 0.81 \cdot 10^{11} cm^{-2}$, $T = 2.2\ K$ and $E_{\mathrm{FIR}} = 10.433\ meV$.

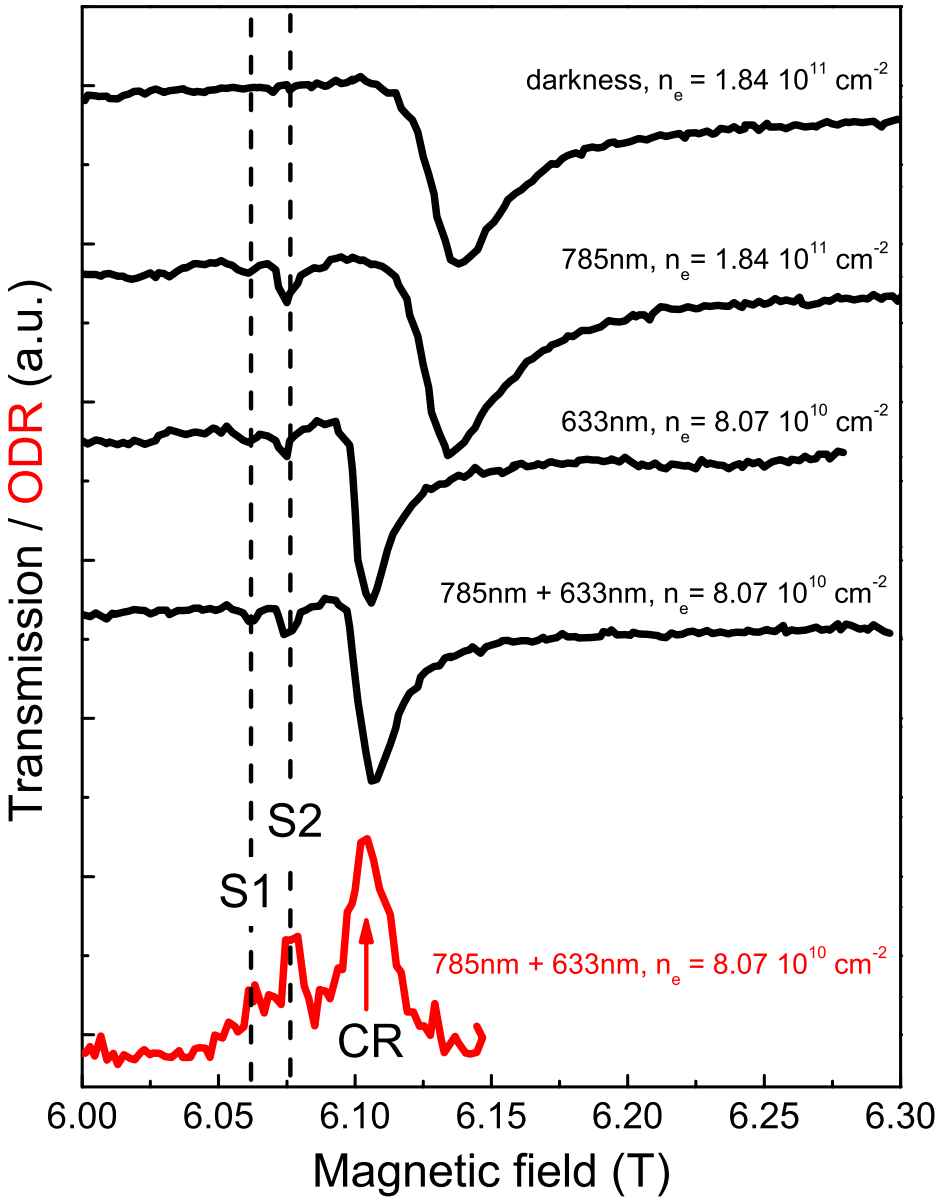


Figure 7.19: Transmission and ODR curves under different illumination conditions. The ODR is measured at the typical conditions: $P_{633nm} = 0.77\ mW/cm^2$ and $P_{785nm} = 0.30\ mW/cm^2$. The FIR transmission is measured at four different optical excitation regimes: $P_{633nm} = 0.77\ mW/cm^2$ and $P_{785nm} = 0.30\ mW/cm^2$, $P_{633nm} = 0.77\ mW/cm^2$ and $P_{785nm} = 0\ mW/cm^2$, $P_{633nm} = 0\ mW/cm^2$ and $P_{785nm} = 0.30\ mW/cm^2$ and complete darkness. $P_{\mathrm{FIR}} = 1.8\ mW/cm^2$, $T = 2.2\ K$ and $E_{\mathrm{FIR}} = 10.433\ meV$.

(d)). Even at high FIR intensities (Fig. 7.18 (c) and (d)) the X-band intensity barely changes at S1 and S2 resonance positions. Only the low energy exciton line gently looses intensity under strong FIR influence.

One might speculate about the physical origin of the S1- and S2-resonance: On the one hand S1 and S2 do not show 2DEG density dependent non-parabolicity effects and thus it could be excluded that they arise from the 2DEG in the HJs potential notch. On the other hand their resonance positions allow to estimate $m^*_{S1} = 0.0675m_0$ and $m^*_{S2} = 0.0673m_0$, very close to GaAs electrons, which is an indicator for electron CR in GaAs. This means that besides the 2DEG at the AlGaAs/GaAs interface, there must be unbound electrons in another region of the sample. In principle such electrons could result from photoexcitation, as long as the electrons have sufficient time to perform cyclotron oscillations before they are caught by holes, i.e. the exciton formation time $\tau_x$ has to be sufficiently long to assure $\omega_c \tau_x > 1$. In fact, time resolved PL studies in GaAs/AlGaAs HJs show remarkably long exciton formation times of more than 1 $ns$ [85], sufficiently long to allow CR of photogenerated electrons.

A FIR transmission experiment supports the idea of CR excitation of photogenerated electrons: Fig. 7.19 shows FIR transmission spectra under different optical excitation conditions (black lines) compared to an ODR spectrum (red line), all of them shifted vertically for better visibility. The ODR spectrum is given for simultaneous above- and below barrier excitation, typically used to obtain and electron density of $n_e = 0.81 \cdot 10^{11} cm^{-2}$. The clearly visible satellite resonances are accentuated by vertical dashed lines to facilitate the comparison with transmission data. The transmission spectra follow a gradual reduction of optical excitation. The lowest is given for the same above- and below barrier excitation as the ODR. All three resonances, CR, S1 and S2 can be identified unambiguously here. Two further transmission spectra are shown for either above- (633 $nm$) or below barrier excitation (785 $nm$), both showing S1 and S2 resonances. The transmission, measured under pure 633 $nm$ above barrier excitation does not differ significantly from the transmission spectra under above- and below barrier excitation. Switching off the 633 $nm$ excitation naturally stops the 2DEG depletion and the CR jumps to the resonance field, expected for the natural electron density $n_e = 1.84 \cdot 10^{11} cm^{-2}$. S1 and S2 however are not influenced by the 2DEG density and stay at the same resonance position. Switching off both lasers and measuring the FIR transmission in complete darkness (Fig. 7.19 top spectrum) shows no satellite resonances besides the main CR. This leads to the conclusion that S1 and S2 base on optically generated carriers. Furthermore, S1 and S2 are observed in transmission at the natural electron density $n_e = 1.84 \cdot 10^{11} cm^{-2}$ as well, while in ODR only the plain CR was visible.

This means that S1 and S2 appear for $\nu < 1$ as well as for $\nu > 1$. They are not observed in ODR for $\nu > 1$ as they are probably hidden by the strong ODCR feature.

# 8
# Conclusions

Due to its especially high electron mobility, 2DEGs in GaAs/AlGaAs HJs provide direct access to intrinsic electronic band structure properties. A powerful experimental technique to determine electronic band parameters is FIR-ODCR.

However, FIR-ODCR on GaAs/AlGaAs HJs has not been satisfyingly discussed so far. The few publications in that field [8, 9, 10, 11] were written before the GaAs/AlGaAs HJ PL was fundamentally reinterpreted by an exciton-dissociation mechanism [6, 30, 7]. An application of the exciton-dissociation model to FIR-ODCR has not been presented so far.

This work demonstrates that the FIR-ODCR mechanism can be explained based on the exciton-dissociation mechanism. The present magneto-PL experiments are fully compatible with this model and new verification for it is shown. Simultaneously, free 3D-excitons and 2DEG-hole recombinations are observed in the PL. The X-band magneto-PL agrees well with the expected behaviour of 3D-excitons in both, the zero field PL energy position and the diamagnetic shift. A rich spectrum of X-band lines can be understood as a mixing of bright and dark exciton states, which occurs in bulk GaAs only. Furthermore, the X-band energy is not affected by the 2DEG density, which again confirms the assumption of 3D-excitons in the GaAs layer. The 2DEG-band PL is in accordance with the expectations: The linear PL field dependence coincides well with the electron- and hole effective masses. The absolute energy position is in agreement with the expected order of magnitude for BGR, confinement potentials and band bending. The intensity redistribution of the main PL-bands is an expression of the exciton dissociation and subsequent supply of free holes for 2DEG-hole recombinations.

As the present FIR-ODCR experiments show, the exciton dissociation into the 2DEG is influenced by resonant FIR-heating of the 2DEG. Due to the spatial separation of 3D-excitons and 2DEG a long-ranging interaction between the hot 2DEG and the 3D excitons has to be considered. Ballistically

propagating phonons are a promising candidate for such a long-range interaction, as estimations of the phonon decay times indicate. It is demonstrated experimentally that most likely nonequilibrium phonons play the main role in the physics of FIR-ODR in GaAs/AlGaAs HJs. The comparison of PL measurements at different temperatures or under FIR irradiation, as well as time resolved FIR-ODR provide strong evidence for this.

Low power excitation allows to measure remarkably narrow ODCR. To the best of our knowledge, the ODCRs presented in this work are the narrowest FIR ODRs in semiconductors reported to date. Applying a basic Drude model of FIR absorption, it is possible to obtain realistic electron mobility values by FIR-ODCR measurements for the first time.

Favored by the narrow linewidths the 2DEG density dependence of the ODCR reveals conduction band nonparabolicity effects in the form of an electron density dependent effective mass. However, the performed data interpolation does not provide reliable values for the nonparabolicity parameter $K_2$, most likely due to rudimentary treatment of the confinement potential. The electron dependence of the ODCR linewidth is well described by the linewidth calculated by the FIR absorption model. In contrast to this, the electron density dependence of the ODCR amplitude reveals a discontinuity at filling factor $\nu = 1$, which can not be explained by the Drude model. It is attributed to the PL modulation mechanism, as the 2DEG is not expected to show a discontinuity in the FIR absorption: FIR transmission experiments are in well agreement with the Drude model and therefore the FIR absorption by the 2DEG is expected to follow a smooth 2DEG density dependence as well.

Furthermore, the narrow ODCR allows to observe satellite resonances, close to the main 2DEG-CR feature. FIR transmission experiments indicate this to be caused by long living photogenerated electrons in the GaAs layer.

Despite the progress in FIR-ODCR on GaAs/AlGaAs HJs, presented in this work, there are still challenging problems to be solved. Especially profound theoretical work is expected to provide a valuable extension of the understanding of exciton dissociation and the interaction of the excitons with the phonon wind.

# Bibliography


[1] M. G. Wright, N. Ahmed, A. Koohian, K. Mitchell, G. R. Johnson, B. C. Cavenett, C. R. Pidgeon, C. R. Stanley, and A. H. Kean, *Far-infrared optically detected cyclotron resonance observation of quantum effects in GaAs*, Semiconductor Science and Technology **5**, 438 (1990).

[2] J. Kono, S. T. Lee, M. S. Salib, G. S. Herold, A. Petrou, and B. D. McCombe, *Optically detected far-infrared resonances in doped GaAs quantum wells*, Phys. Rev. B **52**, R8654 (1995).

[3] A. A. Dremin, D. R. Yakovlev, A. A. Sirenko, S. I. Gubarev, O. P. Shabelsky, A. Waag, and M. Bayer, *Electron cyclotron mass in undoped $CdTe/CdMnTe$ quantum wells*, Phys. Rev. B **72**, 195337 (2005).

[4] A. J. Turberfield, S. R. Haynes, P. A. Wright, R. A. Ford, R. G. Clark, J. F. Ryan, J. J. Harris, and C. T. Foxon, *Optical detection of the integer and fractional quantum Hall effects in GaAs*, Phys. Rev. Lett. **65**, 637 (1990).

[5] H. Buhmann, W. Joss, K. von Klitzing, I. V. Kukushkin, G. Martinez, A. S. Plaut, K. Ploog, and V. B. Timofeev, *Magneto-optical evidence for fractional quantum Hall states down to filling factor 1/9*, Phys. Rev. Lett. **65**, 1056 (1990).

[6] B. M. Ashkinadze, E. Linder, and V. Umansky, *Dimensional magnetoplasma resonance detected by free-exciton photoluminescence in modulation-doped $GaAs/Al_xGa_{1-x}As$ heterojunctions*, Phys. Rev. B **62**, 10310 (2000).

[7] B. M. Ashkinadze, E. Linder, E. Cohen, V. V. Rudenkov, P. C. M. Christianen, J. C. Maan, and L. N. Pfeiffer, *Exciton to two-dimensional electron-hole photoluminescence transitions driven by the quantum Hall effect in photoexcited heterojunctions*, Phys. Rev. B **72**, 075332 (2005).

[8] K. Suzuki, K. Saito, K. Muraki, and Y. Hirayama, *Photoluminescence from a modulation-doped $Al_{0.33}Ga_{0.67}As/GaAs$ heterointerface under cyclotron resonance*, Phys. Rev. B **58**, 15385 (1998).

[9] S. I. Gubarev, A. A. Dremin, A. V. Kukushkin, M. A. V., and M. G. Tyazhlov, *Optical detection of cyclotron resonance at a GaAs-GaAlAs heterojunction*, Pis'ma Zh. Eksp. Teor. Fiz **54**, 361 (1991).

[10] C. C. Chang and R. J. Nicholas, *A far infrared modulated photoluminescence (FIRM-PL) study of cyclotron resonance in a 2D electron gas in $GaAs/Al_xGa_{1-x}As$ heterojunctions*, Semiconductor Science and Technology **14**, 768 (1999).

[11] K. Fujii, M. Saitoh, H. Nakata, and T. Ohyama, *Investigation of the H-band radiation in GaAs/AlGaAs heterostructures by photoluminescence and optically detected cyclotron resonance measurements*, Physica B: Condensed Matter **272**, 454 (1999).

[12] N. Miura, *Physics of semiconductors in high magnetic fields*, 1st edn., Oxford science publications (2008).

[13] M. C. P. Y. Yu, *Fundamentals of semicunductors*, 4th edn., Springer-Verlag Heidelberg (2010).

[14] F. Bloch, *Über die Quantenmechanik der Elektronen in Kristallgittern*, Zeitschrift für Physik A Hadrons and Nuclei **52**, 555 (1929).

[15] J. M. Luttinger and W. Kohn, *Motion of Electrons and Holes in Perturbed Periodic Fields*, Phys. Rev. **97**, 869 (1955).

[16] C. Cohen-Tannoudji, B. Diu, and F. Laloe, *Quantum Mechanics*, Hermann Verlag, Paris (2002).

[17] E. R. G. Landwehr, *Landau Level Spectroscopy*, 1st edn., North Holland (1991).

[18] G. Czycholl, *Theoretische Festkörperphysik*, 2nd edn., Springer-Verlag Berlin Heidelberg (2004).

[19] F. Schwabl, *Quantenmechanik*, 5th edn., Springer-Verlag Berlin Heidelberg (1998).

[20] W. Kohn, *Cyclotron Resonance and de Haas-van Alphen Oscillations of an Interacting Electron Gas*, Phys. Rev. **123**, 1242 (1961).

[21] P. Drude, *Zur Elektronentheorie der Metalle*, Annalen der Physik **306**, 566 (1900).

[22] M. Bayer, *Magnetolumineszenzuntersuchungen zur Dimensionsabhängigkeit der elektronischen Eigenschaften in Halbleiterquantenstrukturen* (1996).

[23] E. L. Ivchenko, *Optical spectroscopy of semiconductor nanostructures*, 1st edn., Springer-Verlag Berlin Heidelberg (2004).

[24] M. Bugajski, W. Kuszko, and K. Reginski, *Diamagnetic shift of exciton energy levels in $GaAs/Ga_{1-x}Al_xAs$ quantum wells*, Solid State Communications **60**, 669 (1986).

[25] Y. Yuan, M. A. A. Pudensi, G. A. Vawter, and J. L. Merz, *New photoluminescence effects of carrier confinement at an AlGaAs/GaAs heterojunction interface*, J. Appl. Phys. **58**, 397 (1985).

[26] A. S. Plaut, I. V. Kukushkin, K. v. Klitzing, and K. Ploog, *Magneto-optics in GaAs-$Al_xGa_{1-x}As$ single heterojunctions*, Phys. Rev. B **42**, 5744 (1990).

[27] E. S. Koteles and J. Y. Chi, *Photoluminescence spectra of modulation-doped GaAs/AlGaAs heterointerfaces*, Superlattices and Microstructures **2**, 421 (1986).

[28] I. Balslev, *Recombination via two-dimensional excitons in GaAs-(AlGa)As heterojunctions*, Semiconductor Science and Technology **2**, 437 (1987).

[29] H. P. van der Meulen, D. Sarkar, J. M. Calleja, R. Hey, K. J. Friedland, and K. Ploog, *Free versus localized hole magnetophotoluminescence in semiconductor heterojunctions near integer filling factors*, Phys. Rev. B **70**, 155314 (2004).

[30] B. M. Ashkinadze, V. Voznyy, E. Cohen, A. Ron, and V. Umansky, *Condensation of bulk excitons on a magnetized two-dimensional electron gas in modulation-doped heterojunctions*, Phys. Rev. B **65**, 073311 (2002).

[31] S. B. Nam, D. C. Reynolds, C. W. Litton, R. J. Almassy, T. C. Collins, and C. M. Wolfe, *Free-exciton energy spectrum in GaAs*, Phys. Rev. B **13**, 761 (1976).

[32] J. H. Davies, *The Physics of low-dimensional semiconductors*, 1st edn., Cambridge University Press (1998).

[33] D. A. Kleinman and R. C. Miller, *Band-gap renormalization in semiconductor quantum wells containing carriers*, Phys. Rev. B **32**, 2266 (1985).

[34] J. L. Osborne, A. J. Shields, M. Y. Simmons, N. R. Cooper, D. A. Ritchie, and M. Pepper, *Excitonic recombination processes in spin-polarized two-dimensional electron gases*, Phys. Rev. B **58**, R4227 (1998).

[35] N. R. Cooper and D. B. Chklovskii, *Theory of photoluminescence of the $\nu = 1$ quantum Hall state: Excitons, spin waves, and spin textures*, Phys. Rev. B **55**, 2436 (1997).

[36] C. Kallin and B. I. Halperin, *Excitations from a filled Landau level in the two-dimensional electron gas*, Phys. Rev. B **30**, 5655 (1984).

[37] E. D. Palik, G. S. Picus, S. Teitler, and R. F. Wallis, *Infrared Cyclotron Resonance in InSb*, Phys. Rev. **122**, 475 (1961).

[38] M. Godlewski, W. Chen, and B. Monemar, *Optical detection of cyclotron resonance for characterization of recombination processes in semiconductors*, Critical Reviews in Solid State and Materials Sciences **19**, 241.

[39] P. Baranov, Y. P. Veshchunov, R. A. Zhitnikov, N. G. Romanov, and Y. G. Shreter, *Optical detection of microwave resonance in germanium by means of luminescence of electron hole drops*, Pis'ma Zh. Eksp. Teor. Fiz. **26**, 369 (1977).

[40] R. Romestain and C. Weisbuch, *Optical Detection of Cyclotron Resonance in Semiconductors*, Phys. Rev. Lett. **45**, 2067 (1980).

[41] J. G. Michels, R. J. Warburton, R. J. Nicholas, and C. R. Stanley, *An optically detected cyclotron resonance study of bulk GaAs*, Semiconductor Science and Technology **9**, 198 (1994).

[42] G. S. Herold, H. A. Nickel, J. G. Tischler, B. A. Weinstein, and B. D. McCombe, *Full-spectrum optically detected resonance (ODR) spectroscopy of GaAs/AlGaAs quantum wells*, Physica E: Low-dimensional Systems and Nanostructures **2**, 39 (1998).

[43] H. Nickel, G. Herold, T. Yeo, G. Kioseoglou, Z. Jiang, B. McCombe, A. Petrou, D. Broido, and W. Schaff, *Internal Transitions of Neutral and Charged Magneto-Excitons in GaAs/AlGaAs Quantum Wells*, physica status solidi (b) **210**, 341 (1998).

[44] M. S. Salib, H. A. Nickel, G. S. Herold, A. Petrou, B. D. McCombe, R. Chen, K. K. Bajaj, and W. Schaff, *Observation of Internal Transitions of Confined Excitons in GaAs/AlGaAs Quantum Wells*, Phys. Rev. Lett. **77**, 1135 (1996).

[45] H. Nickel, G. Herold, M. Salib, G. Kioseoglou, A. Petrou, B. McCombe, and D. Broido, *Internal transitions of excitons and hole cyclotron resonance in undoped GaAs/AlGaAs quantum wells by optically detected resonance spectroscopy*, Physica B: Condensed Matter **249-251**, 598 (1998).

[46] C. J. Meining, V. R. Whiteside, B. D. McCombe, A. B. Dzyubenko, J. G. Tischler, A. S. Bracker, and D. Gammon, *Internal transitions of quasi-two-dimensional charged magnetoexcitons in the presence of purposely introduced weak lateral potential energy variations*, Phys. Rev. B **75**, 165301 (2007).

[47] J. Černe, J. Kono, M. S. Sherwin, M. Sundaram, A. C. Gossard, and G. E. W. Bauer, *Terahertz Dynamics of Excitons in GaAs/AlGaAs Quantum Wells*, Phys. Rev. Lett. **77**, 1131 (1996).

[48] H. A. Nickel, T. Yeo, C. J. Meining, D. R. Yakovlev, M. Furis, A. B. Dzyubenko, B. D. McCombe, and A. Petrou, *Interaction of an electron gas with photoexcited electron-hole pairs in modulation-doped GaAs and CdTe quantum wells*, Physica E: Low-dimensional Systems and Nanostructures **12**, 499 (2002).

[49] B. N. Murdin, A. R. Hollingworth, J. A. Barker, D. G. Clarke, P. C. Findlay, C. R. Pidgeon, J.-P. R. Wells, I. V. Bradley, S. Malik, and R. Murray, *Double-resonance spectroscopy of InAs/GaAs self-assembled quantum dots*, Phys. Rev. B **62**, R7755 (2000).

[50] R. A. Child, R. J. Nicholas, N. J. Mason, P. A. Shields, J.-P. R. Wells, I. V. Bradley, J. Phillips, and B. N. Murdin, *Far-infrared modulated photoluminescence spectroscopy of InSb/GaSb quantum dot structures*, Phys. Rev. B **68**, 165307 (2003).

[51] A. Moll, C. Wetzel, B. K. Meyer, P. Omling, and F. Scholz, *Microwave and far-infrared induced optically detected cyclotron resonance in epitaxial InP and GaAs*, Phys. Rev. B **45**, 1504 (1992).

[52] N. Ahmed, I. R. Agool, M. G. Wright, K. Mitchell, A. Koohian, S. J. A. Adams, C. R. Pidgeon, B. C. Cavenett, C. R. Stanley, and A. H. Kean, *Far-infrared optically detected cyclotron resonance in GaAs layers and low-dimensional structures*, Semiconductor Science and Technology **7**, 357 (1992).

[53] R. J. Warburton, J. G. Michels, R. J. Nicholas, J. J. Harris, and C. T. Foxon, *Optically detected cyclotron resonance of GaAs quantum wells:*

*Effective-mass measurements and offset effects*, Phys. Rev. B **46**, 13394 (1992).

[54] J. Michels, R. Warburton, R. Nicholas, J. Harris, and C. Foxon, *Optically detected cyclotron resonance of GaAs quantum wells: Effective-mass measurements and offset effects*, Physica B: Condensed Matter **184**, 159 (1993).

[55] D. M. Hofmann, M. Drechsler, C. Wetzel, B. K. Meyer, F. Hirler, R. Strenz, G. Abstreiter, G. Böhm, and G. Weimann, *Optically detected cyclotron resonance on $GaAs/Al_xGa_{1-x}As$ quantum wells and quantum wires*, Phys. Rev. B **52**, 11313 (1995).

[56] C. Wetzel, A. L. Efros, A. Moll, B. K. Meyer, P. Omling, and P. Sobkowicz, *Dependence on quantum confinement of the in-plane effective mass in $Ga_{0.47}In_{0.53}As/InP$ quantum wells*, Phys. Rev. B **45**, 14052 (1992).

[57] C. R. L. P. N. Jeukens, P. C. M. Christianen, J. C. Maan, D. R. Yakovlev, W. Ossau, V. P. Kochereshko, T. Wojtowicz, G. Karczewski, and J. Kossut, *Dynamical equilibrium between excitons and trions in CdTe quantum wells in high magnetic fields*, Phys. Rev. B **66**, 235318 (2002).

[58] M. A. Hopkins, R. J. Nicholas, M. A. Brummell, J. J. Harris, and C. T. Foxon, *Cyclotron-resonance study of nonparabolicity and screening in $GaAs/Ga_{1-x}Al_xAs$ heterojunctions*, Phys. Rev. B **36**, 4789 (1987).

[59] M. J. Chou, D. C. Tsui, and G. Weimann, *Cyclotron resonance of high-mobility two-dimensional electrons at extremely low densities*, Phys. Rev. B **37**, 848 (1988).

[60] L. J. Challis, A. J. Kent, and V. W. Rampton, *Phonon studies of two-dimensional electron gases*, Semiconductor Science and Technology **5**, 1179 (1990).

[61] S. I. Tamura, *Spontaneous decay rates of LA phonons in quasi-isotropic solids*, Phys. Rev. B **31**, 2574 (1985).

[62] V. S. Bagaev, L. V. Keldysh, N. N. Sibel'din, and V. A. Tsvetkov, *Dragging of excitons and electron-hole drops by phonon wind*, Sov. Phys. JETP **43**, 362 (1976).

[63] A. V. Akimov, A. A. Kaplyanskii, E. S. Moskalenko, and R. A. Titov, *Drag of excitons by heat-generated phonon pulses in silicon*, Zh. Eksp. Teor. Fiz. **94**, 307 (1988).

[64] E. Moskalenko, A. Akimov, A. Kaplyanskii, A. Zhmodikov, L. Challis, T. Cheng, and C. Foxon, *Effect of nonequilibrium acoustic phonons on exciton states in interrupted grown $GaAs/Al_{0.33}Ga_{0.67}As$ quantum wells*, Physica B: Condensed Matter **219-220**, 59 (1996).

[65] N. N. Zinov'ev, L. P. Ivanov, V. I. Kozub, and I. D. Yaroshetskii, *Exciton transport by nonequilibrium phonons and its effect on recombination radiation from semiconductors at high excitation levels*, Zh. Eksp. Teor. Fiz. **84**, 1761 (1983).

[66] M. C. DeLong, I. Viohl, W. D. Ohlsen, P. C. Taylor, and J. M. Olson, *Microwave thermal modulation of photoluminescence in III-V semiconductors*, Phys. Rev. B **43**, 1510 (1991).

[67] A. V. Akimov, A. V. Scherbakov, and Y. D. R., *Handbook of Semiconductor Nanostructures and Nanodevices*, vol. 3, chap. 2, American Scientific Publishers (2006).

[68] S. M. Rywkin, *Photoelektrische Erscheinungen in Halbleitern*, Berichte der Bunsengesellschaft für physikalische Chemie **70**, 929 (1966).

[69] H. Störmer, *Electron mobilities in modulation-doped GaAs-(AlGa)As heterostructures*, Surface Science **132**, 519 (1983).

[70] M. Kozhevnikov, B. M. Ashkinadze, E. Cohen, and A. Ron, *Low-temperature electron mobility studied by cyclotron resonance in ultrapure GaAs crystals*, Phys. Rev. B **52**, 17165 (1995).

[71] M. A. Hopkins, R. J. Nicholas, D. J. Barnes, M. A. Brummell, J. J. Harris, and C. T. Foxon, *Temperature dependence of the cyclotron-resonance linewidth in $GaAs/Ga_{1-x}Al_xAs$ heterojunctions*, Phys. Rev. B **39**, 13302 (1989).

[72] T. J. Drummond, W. Kopp, R. Fischer, and H. Morkoc, *Influence of AlAs mole fraction on the electron mobility of (Al,Ga)As/GaAs heterostructures*, Journal of Applied Physics **53**, 1028 (1982).

[73] K. Chiu, T. Lee, and J. Quinn, *Infrared magneto-transmittance of a two-dimensional electron gas*, Surface Science **58**, 182 (1976).

[74] O. M. Fedorych, M. Potemski, S. A. Studenikin, J. A. Gupta, Z. R. Wasilewski, and I. A. Dmitriev, *Quantum oscillations in the microwave magnetoabsorption of a two-dimensional electron gas*, Phys. Rev. B **81**, 201302 (2010).

[75] X. Wang, D. J. Hilton, J. L. Reno, D. M. Mittleman, and J. Kono, *Direct measurement of cyclotron coherence times of high-mobility two-dimensional electron gases*, Optics Express **18**, 12354 (2010).

[76] Z. G. Hu, M. B. M. Rinzan, S. G. Matsik, A. G. U. Perera, G. Von Winckel, A. Stintz, and K. S., *Optical characterizations of heavily doped p-journal article AlxGa1?xAs and GaAs epitaxial films at terahertz frequencies* **97**, 093529 (2005).

[77] E. O. Kane, *Band structure of indium antimonide*, Journal of Physics and Chemistry of Solids **1**, 249 (1957).

[78] R. F. Wallis, *Theory of cyclotron-resonance absorption by conduction electrons in indium antimonide*, Journal of Physics and Chemistry of Solids **4**, 101 (1958).

[79] J. G. Michels, M. S. Daly, P. Gee, S. Hill, R. J. Nicholas, J. Singleton, G. M. Summers, R. J. Warburton, C. T. Foxon, and J. J. Harris, *Cyclotron resonance and spin states in GaAs/Ga*$1-xAlxAs$ *heterojunctions: Experiment and theory*, Phys. Rev. B **54**, 13807 (1996).

[80] F. M. Peeters, W. Xiaoguang, and J. T. Devreese, *Landau levels above the optical-phonon continuum in two and three dimensions*, Phys. Rev. B **33**, 4338 (1986).

[81] M. Manger, E. Batke, and W. Wegscheider, *Cyclotron resonance at fractional Landau-level fillings*, Solid State Communications **120**, 463 (2001).

[82] M. Manger and E. Batke, *High-frequency conductivity of the multi-component cyclotron resonance: a classical approach*, Superlattices and Microstructures **33**, 249 (2003).

[83] Z. Schlesinger, S. J. Allen, J. C. M. Hwang, P. M. Platzman, and N. Tzoar, *Cyclotron resonance in two dimensions*, Phys. Rev. B **30**, 435 (1984).

[84] J. Richter, H. Sigg, K. von Klitzing, and K. Ploog, *Cyclotron resonance of two-dimensional electron systems under the influence of ionized impurity-scattering*, Surface Science **228**, 159 (1990).

[85] J. X. Shen, Y. Oka, C. Y. Hu, W. Ossau, G. Landwehr, K.-J. Friedland, R. Hey, K. Ploog, and G. Weimann, *Photoluminescence in modulation-doped* $GaAs/Ga_{1-x}Al_xAs$ *heterojunctions*, Phys. Rev. B **59**, 8093 (1999).

# List of publications

1. G. Bartsch, C. Zens, B. Ashkinadze, D. R. Yakovlev and M. Bayer
   *Optically detected far-infrared cyclotron resonance in a GaAs/AlGaAs heterojunction*
   (in preparation)

2. G. Bartsch, M. Gerbracht, D. R. Yakovlev, J. Blokland, P. C. M. Christianen, E. A. Zhukov, A. B. Dzyubenko, G. Karczewski, T. Wojtowicz, J. Kossut, J. C. Maan and M. Bayer
   *Positively versus negatively charged excitons: A high magnetic field study of $CdTe/Cd_{1-x}Mg_xTe$ quantum wells*
   Physical Review B **83**, 235317 (2011)

3. J. Jadczak, L. Bryja, A. Wojs, G. Bartsch, D. R. Yakovlev, M. Bayer, P. Plochocka, M. Potemski, D. Reuter and A. Wieck
   *Exciton Exchange between Nearly-Free and Acceptor-Bound States of a Positive Trion Assisted by Cyclotron Excitation*
   Acta Physica Polonica A **119**, 600 (2010)